Bose-Einstein Condensates in Coupled Co-planar Double-Ring Traps

A thesis presented in partial fulfillment of the requirements for the degree of

Masterate of Science in Physics

at

Massey University
Palmerston North, New Zealand.

Tania J. Haigh

2008

Abstract

This thesis presents a theoretical study of Bose-Einstein condensates in a double-ring trap. In particular, we determine the ground states of the condensate in the double-ring trap that arise from the interplay of quantum tunnelling and the trap's rotation.

The trap geometry is a concentric ring system, where the inner ring is of smaller radius than the outer ring and both lie in the same two-dimensional plane. Due to the difference in radii between the inner and outer rings, the angular momentum that minimises the kinetic energy of a condensate when confined in the individual rings is different at most frequencies. This preference is in direct competition with the tunnel coupling of the rings which favours the same angular momentum states being occupied in both rings.

Our calculations show that at low tunnel coupling ground state solutions exist where the expectation value of angular momentum per atom in each ring differs by approximately an integer multiple. The energy of these solutions is minimised by maintaining a uniform phase difference around most of the ring, and introducing a Josephson vortex between the inner and outer rings. A Josephson vortex is identified by a 2π step in the relative phase between the two rings, and accounts for one quantum of circulation. We discuss similarities and differences between Josephson vortices in cold-atom systems and in superconducting Josephson junctions.

Josephson vortices are actuated by a sudden change in the trapping potential. After this change Josephson vortices rotate around the double-ring system at a different frequency to the rotation of the double-ring potential. Numerical studies of the dependence of the velocity on the ground state tunnel coupling and interaction strength are presented. An analytical theory of the Josephson vortex dynamics is also presented which is consistent with our numerical results.

Acknowledgements

I would like to thank my supervisor Ulrich Zuelicke for providing such an interesting research project, and for his guidance and contribution to the research. Also, for the time spent reading my thesis drafts and offering suggestions for improvements. Also my co-supervisor, Joachim Brand, for his input into the direction of the project, and for the MATLAB code. I am grateful to have been provided with a Massey University Masterate Scholarship, without which I would not have been able to complete this work. Thanks to Katrina, for her time spent proof reading. And finally, thanks to all my family for their continued support and for their confidence in me.

Contents

List of Figures

Chapter 1

Basic Theory

We briefly review the concept of Bose-Einstein condensation, and introduce the Gross-Pitaevskii approach which is the method used to describe condensates throughout this thesis. Our double-ring geometry allows us to investigate the combined effects of a rotation of the condensate, and of quantum tunneling of atoms between the inner and outer rings. To introduce these ideas, we discuss separately the rotational ground states and behaviour of a condensate in a ring trap, and then the eigenstates and dynamics of a condensate confined in a double well potential.

1.1 Introduction to Bose-Einstein condensation

At very low temperatures, a phase transition called Bose-Einstein condensation can occur for bosonic atoms. During this phase transition, many atoms fall or 'condense' into the lowest energy state of the system. This results in a phase of matter quite unlike the states of our everyday experience (gas, liquid, solid). In a Bose-Einstein condensate the quantum nature of matter becomes visible on a macroscopic scale.

The prediction of Bose-Einstein condensation in 1925 was due to a combination of work by Albert Einstein and the Indian physicist Satyendra Bose. In 1924 Bose gave a derivation of Planck's radiation law for photons within an entirely quantum mechanical framework [1]. After Bose's paper was rejected for publication he then sent it to Einstein who was working in Berlin at the time. Einstein recognized the importance of the derivation, and with his endorsement the paper was published. Applying the same technique to an ideal (non-interacting) gas of atoms allowed Einstein to write the distribution function for such atoms [2]. This so-called Bose-Einstein distribution can be used to derive an expression for the number of atoms in state s with energy ϵ_s as a function of temperature. It is from studying these occupations that the Bose-Einstein condensate (BEC) phase transition is understood.

Einstein's distribution formula is as follows:

$$n_s = \frac{1}{e^{\beta(\epsilon_s - \mu)} - 1} \tag{1.1}$$

where μ is the chemical potential of the state. To ensure positive occupation numbers of all states, μ must be less than the ground state energy. As the chemical potential becomes similar to the energy of the lowest energy state, which it does as temperature decreases, the occupation of this state grows exponentially. It is the atoms which occupy this lowest energy state that are referred to as the 'condensate'.

Despite its early prediction, it was not until 1995 that Bose-Einstein condensation was first achieved. This time lapse was due to the technical difficulties of cooling atoms to the nanoKelvin temperatures required for the transition to occur. Steven Chu, Claude Cohen-Tannoudji and William D. Phillips developed "methods to cool and trap atoms with laser light" and were jointly awarded the 1999 Nobel Prize for Physics for these results [3]. Their methods finally enabled atoms to be cooled sufficiently for Bose-Einstein condensation to be observed. Eric Cornell, Carl Wieman, and Wolfgang Ketterle were leaders of the first two experimental groups to achieve Bose-Einstein condensation [4, 5]. These three scientists were joint recipients of the Nobel Prize in Physics in 2001 "for the achievement of Bose-Einstein condensation in dilute gases of alkali atoms, and for early fundamental studies of the properties of the condensates" [6].

In a Bose-Einstein condensate of ideal atoms, only one single particle state is occupied. The large number of atoms in this state means that the nature and dynamics predicted by quantum physics for the single state are amplified and become visible on a macroscopic scale (μm in current experiments). Because of the identical behaviour of all the atoms, the condensate is said to be coherent. Shortly after the first successful BEC apparatus were set up, at MIT [7] experiments were conducted to demonstrate this coherence by allowing two separated condensates to overlap. The result was a set of interference fringes that were due to the existence of a uniform relative phase between the two condensates.

The contribution of Bose-Einstein condensation to increasing and verifying our understanding of fundamental physics is not the only reason for the growing interest in the field since its practical achievement in 1995. Some current areas of research include:

- Developing methods to describe the effects of finite temperature on condensate behaviour [8]
- Creating condensates of molecules, or mixtures of different atoms [9]
- Studying the changes in behaviour due to different interaction strengths (e.g. the collapse of a condensate with attractive interactions) [10]
- Designing atom lasers, and other ways to control matter more precisely than ever before [11]
- Matter wave interferometry [12]
- Using atom chips to create confinements for atomic BECs [13]

Bose-Einstein condensates have the potential to be used in many practical areas due to their high sensitivity to gravitational fields, as well as to rotation. Commercially available applications are years away, however, as there is much work still to be done in increasing our understanding of Bose-Einstein condensates and their behaviour, not to mention the formidable challenge presented by attempting to produce functional devices at the low temperatures required for a condensate to even exist.

1.2 Gross-Pitaevskii mean-field theory

A Bose-Einstein condensate can be described relatively simply if one neglects all the atoms which are not in the very lowest energy state. This is equivalent to assuming that the system is at zero temperature. In reality due to the finite temperature at which experiments are conducted there will always be some higher energy modes occupied, and these can influence the behaviour of the condensate significantly. However, in certain limits, the Gross-Pitaevskii approach can be used to describe the condensate [14]. For this approach to be valid the condensate must contain a large number of particles, the condensate must be weakly interacting and dilute, and the temperature must be low enough so that the thermal component is negligible. The Gross-Pitaevskii approach can only be used to investigate distances larger than the scattering length.

The assumption that a single-particle state is macroscopically occupied allows the many-body wavefunction to be approximated by an order parameter. The order parameter is the wavefunction of this single-particle state, and has a time-dependence given by $\Phi(\vec{r},t) = e^{i\mu t}\Psi(\vec{r})$, where μ is the chemical potential. The Gross-Pitaevskii energy functional for the order parameter is [15–17]:

$$E = \int \left(\Psi(\vec{r})^* \left[\frac{\hbar^2 \nabla^2}{2M} + V_{\text{ext}} + \frac{gN}{2} |\Psi(\vec{r})|^2 \right] \Psi(\vec{r}) \right) d\vec{r} \tag{1.2}$$

where V_{ext} is some external potential, and M is the mass of one atom. The non-linear term describes the two-body interactions between particles. These are repulsive if g is positive, and attractive if g is negative. The parameter g is related to the s-wave scattering length. N is the number of atoms in the condensate.

Minimising the energy with respect to $\Psi(\vec{r})^*$, and keeping the number of atoms in the condensate constant yields the time-independent Gross-Pitaevskii equation [14]:

$$\mu\Psi(\vec{r}) = \left(-\frac{\hbar^2 \nabla^2}{2M} + V_{\text{ext}}(\vec{r},t) + gN|\Psi(\vec{r})|^2 \right) \Psi(\vec{r}) \quad . \tag{1.3}$$

In this equation, $\Psi(\vec{r})$ is the wave function for one atom in the condensate and should be normalised to 1. The order parameter of the entire condensate is given by $\sqrt{n(\vec{r})}\Psi(\vec{r})$ where $n(\vec{r})$ is the condensate density.

The Gross-Pitaevskii theory described above is not always valid. In double well systems, the theory may fail at small values of tunnel coupling because it only permits the existence of one condensate consisting of all the atoms in the double well, hence assuming that all the atoms share the same phase. The Gross-Pitaevskii theory does not consider the possibility that two separate condensates could exist, each localised in one of the two wells, and that this arrangement could be of lower energy overall than the single-condensate model. If there were these two separate condensates then they would have a random relative phase. This separation or 'fragmentation' of the condensate is expected in potentials where the tunnel coupling is very small, or when the interactions are reasonably large [18].

1.3 Bose-Einstein condensates in non-trivial traps

1.3.1 Ring traps

When considering a condensate in a rotating trap, it is easier to work in the rotating frame where the trapping potential is stationary. Using a Galilean transformation of the Lagrangian, the Hamiltonian can be written in the coordinates of the frame which is rotating with angular velocity, Ω [17]. The energy in the rotating frame is then:

$$E = \int \left(\Psi(\vec{r})^* \left[\frac{\hbar^2 \nabla^2}{2M} + V_{\text{ext}} + \frac{gN}{2} |\Psi(\vec{r})|^2 \right] \Psi(\vec{r}) \right) d\vec{r} - \Omega L_z \tag{1.4}$$

where V_{ext} is stationary, and the coordinates $\vec{r}$ are now the coordinates in the rotating frame. L_z is the angular momentum operator. From this energy expression it is easy to see that at a sufficiently large rotational frequency, the energy of a state with finite and positive angular momentum may be lower than the non-rotating state and so may be the ground state of the system.

In the new frame of reference, the Gross-Pitaevskii equation becomes:

$$i\hbar \frac{\partial}{\partial t} \Phi(\vec{r}, t) = \left(\frac{-\hbar^2}{2M} \nabla^2 + V_{\text{ext}}(r, t) + gN |\Phi(\vec{r}, t)|^2 - \Omega L_z \right) \Phi(\vec{r}, t) \quad . \tag{1.5}$$

In the case of a cylindrically symmetric external potential, the following wave function ansatz for stationary states can be made:

$$\Psi(r, \theta) = \psi(r) e^{im\theta} \tag{1.6}$$

where m is restricted to integers due to the requirement that the wave function must be single-valued at all points in space. The density of these solutions is only dependent on the radial coordinate, thus retaining the cylindrical symmetry of the system, but the complex phase can vary around the angular coordinate. The z-component of the angular momentum operator is $L_z = -i\hbar(\partial/\partial\theta)$. Substituting this operator, and the ansatz above into equation (1.5) we find:

$$\mu\psi(r) = \left(\frac{-\hbar^2}{2M} \frac{1}{r} \frac{\partial}{\partial r} \left(r \frac{\partial}{\partial r} \right) + \frac{\hbar^2}{2M} \frac{m^2}{r^2} + V_{\text{ext}}(r, t) + gN |\psi(r)|^2 - m\hbar\Omega \right) \psi(r) \quad . \tag{1.7}$$

From this we see that the angular momentum of each atom in the condensate is $m\hbar$. Solutions of the type given in equation (1.6) for any finite m must be zero-valued at $r = 0$, which in toroidal confinements is often already the case due to the potential. For a condensate confined in a ring, solutions with $m > 1$ are states where all atoms in the condensate circulate around the ring, all carrying exactly m quanta of angular momentum. These states are often referred to as 'persistent current' states.

In a similar way that a supercurrent of electrons through a superconductor flows continually without reducing in amplitude due to the lack of resistance, a circulating current of atoms in a toroidal trap is expected to continue circulating due to the lack of dissipation of energy through friction. They are also stable with respect to a change in the angular momentum, because this requires a vortex to cross the ring. [19]. The movement of a vortex across the ring requires a large density perturbation, but in a repulsively interacting system this costs a lot of energy and is therefore unlikely to happen. Persistent currents of atoms in a ring trap have recently been observed [20].

1.3.2 Double wells

Here we introduce the two-state model [21] to illustrate the effects of a coupling between two states. This model has been widely used to investigate the dynamics of condensates in double wells, see for example Refs. [22–24]. These dynamics are Josephson oscillations, which were first predicted [25] and observed in superconducting Josephson junctions (for a review of the Josephson effect in superconducting structures see [26]). Section 3.1 contains a detailed derivation of a two-state model for our co-planar double-ring system.

For the two-state model to be a good approximation, the energies of the two separate states must be close, and also far away from the energy of all other possible states in the system. This is so that transitions from either of the two states under consideration to other higher energy states (or vice versa) are negligible and the effects of a coupling between the two states can be calculated easily. The two isolated states have energies $E_{1/2}$, where $\mathcal{H}$ is the Hamiltonian of the system.

$$\mathcal{H}|\psi_{1/2}\rangle = E_{1/2}|\psi_{1/2}\rangle \tag{1.8}$$

Introducing a coupling between these two states, the Hamiltonian of the combined system can now be expressed as the sum of the Hamiltonian of the uncoupled states and some purely off-diagonal elements describing the transitions. To ensure the Hamiltonian is Hermitian, these off-diagonal elements must be the complex conjugate of each other.

$$\mathcal{H} = \begin{bmatrix} E_1 & 0 \\ 0 & E_2 \end{bmatrix} + \begin{bmatrix} 0 & te^{i\varphi} \\ te^{-i\varphi} & 0 \end{bmatrix} \tag{1.9}$$

Due to the coupling, the individual states are no longer eigenstates of the combined system. Diagonalising the above Hamiltonian yields the following eigenvalues for the combined system [21]:

$$E_\pm = \frac{1}{2}\left(E_1 + E_2\right) \pm \frac{1}{2}\sqrt{\left(E_1 - E_2\right)^2 + 4|t|^2} \quad . \tag{1.10}$$

From this we see that the coupling produces an energy splitting, so that the eigenstates of the combined system have either higher or lower energy than each of the individual states. Note that the eigenenergies depend only on $|t|$, and the phase of the coupling term does not enter into this calculation.

The new eigenvectors of the combined system are [21]:

$$|\psi_+\rangle = \cos\frac{\theta}{2}e^{-i\frac{\varphi}{2}}|\psi_1\rangle + \sin\frac{\theta}{2}e^{i\frac{\varphi}{2}}|\psi_2\rangle \tag{1.11}$$

$$|\psi_-\rangle = -\sin\frac{\theta}{2}e^{-i\frac{\varphi}{2}}|\psi_1\rangle + \cos\frac{\theta}{2}e^{i\frac{\varphi}{2}}|\psi_2\rangle \tag{1.12}$$

where the angle θ is defined as

$$\tan\theta = \frac{2|t|}{E_1 - E_2} \tag{1.13}$$

and is restricted to $0 \leq \theta < \pi$.

When using a two-state model to describe a Bose-Einstein condensate in a double well the atoms can be in one of two possible states - either localized in the 'left' or

the 'right' well - and there is some possibility for atoms to transfer from one well to the other through quantum tunneling [21]. In this case the eigenenergies $E_{\pm}$ are the ground and first excited states of the double well.

Although only the absolute value of the coupling term appears in the calculation of the eigenenergies, the sign of this term can be determined by requiring the ground state eigenvector to be symmetric, and the first excited state eigenvector to be antisymmetric. These symmetries are required by the node theorem [27]. In the case of a one-dimensional system described by the Schrodinger equation, the node theorem states that "If one arranges the eigenstates in order of increasing energies, the eigenfunctions likewise fall in the order of increasing nodes" [27]. In a two-state system the symmetric wave function with no nodes must be of lower energy than the antisymmetric wave function which has one node.

Examining the ground state eigenvector, we see that over the interval $[0, \pi]$ the sine and cosine terms are both positive, so that the eigenvector can be written as:

$$|\psi_-\rangle \propto -|\psi_1\rangle + e^{i\varphi}|\psi_2\rangle \quad . \tag{1.14}$$

For this vector to be symmetric, the phase of the coupling term is restricted to $\pi/2 \leq \varphi < 3\pi/2$. Over this range, the real part of the tunnel coupling term is negative.

The dynamics of a Bose-Einstein condensate can also be studied within the two-state model. Coupled equations for the population difference, and the relative phase between the wells can be derived by substituting the approximate wave function into the time-dependent Gross-Pitaevskii equation (see [22, 23]). These equations predict that if an initial population difference exists, the relative phase will evolve in time. This gives rise to oscillations of a fraction of the population between the two wells. In 2005 Albiez et al. [28] published results of an experiment demonstrating these Josephson oscillations of a Bose-Einstein condensate in a double well. They also observed a regime where very small oscillations around an initial large population imbalance occurred. This is called 'macroscopic quantum self-trapping', and is due to the interacting nature of the atoms. This effect does not exist in the superconducting Josephson effect, but rather is unique to the condensate experiment.

Chapter 2

Model for Double-Ring BECs

Laser beams have been used to confine and manipulate atomic Bose-Einstein condensates, and the existence of hollow beams (for example, Laguerre-Gaussian lasers) points to the possibility of creating toroidal confinements for BEC. We describe a possible optical double-ring potential for a BEC, which is formed from two Laguerre-Gaussian laser beams. Also a rescaling of the Gross-Pitaevskii equation into suitable dimensionless units is presented, which we use for the calculations in the following chapters.

2.1 Toroidal traps using Laguerre-Gaussian laser beams

We study a Bose-Einstein condensate confined in an optical double-ring trap. One advantage of optical traps over magnetic traps is that they can confine atoms regardless of their spin state. The energy levels of atoms in a magnetic field are shifted (the Zeeman effect), so that atoms in a magnetic field gradient experience a force toward the direction where their energy levels are lower. Whether this results in atoms gathering in a region of high or low magnetic field intensity depends of course on their internal spin state. For atoms which are not spin-polarized, this means magnetic traps can only confine a fraction of atoms in a given sample. In an electric field, the energy levels of an atom are also shifted (the AC Stark effect). In a light field containing an intensity gradient, the atomic energy levels are then also a function of the spatial coordinates. Such a field can also be used to confine and manipulate atomic BECs, since the atoms will tend to be found in areas where their energy is lower. This can be an area of high or low intensity depending on the frequency of the laser field but is independent of the spin state of the atoms.

Optical traps also provide a more diverse range of trapping geometries than magnetic traps alone. In 2000, Wright et al. [29] proposed a method of confining atomic Bose-Einstein condensates in a ring shape by using Laguerre-Gaussian laser beams. These beams are cylindrically symmetric and their name describes the intensity profile in the plane perpendicular to the axis of propagation. The product of a Laguerre polynomial and a Gaussian function provides a series of peaks which decay in intensity from the centre of the beam outward. A beam with one ring of high intensity is a hollow cylinder, which, perpendicular to the axis of propagation, can provide a toroidal confinement for an atomic BEC. Laguerre-Gaussian beams

with one or multiple peaks in the intensity profile can also be produced, offering the possibility of confining a condensate in concentric rings. Wright et al. [29] present a mathematical description of the confining potential experienced by an atomic BEC due to a single Laguerre-Gaussian beam. We describe this briefly, then in the following section we consider the possible construction of a double-ring optical trap using a combination of two Laguerre-Gaussian beams.

Laguerre-Gaussian laser beams are characterized by the two integers ℓ and p. A given beam has $p+1$ radial nodes (peaks) in the intensity profile. The index ℓ gives the number of 2π phase cycles around the circumference, and determines the strength of the confining rings. The depth of the rings increases and the width decreases as ℓ takes larger values.

The optical dipole potential created by a laser field is given by [30], [31]:

$$V(\mathbf{r}_\perp) = \frac{\hbar\Delta}{2}\log\left[1+\frac{I(\mathbf{r}_\perp)/I_{\mathrm{Sat}}}{1+(2\Delta/\Gamma^2)^2}\right] \tag{2.1}$$

where Δ is the laser detuning (the difference between the laser frequency and the frequency of atomic transition), Γ is the linewidth of the optical transition (the range of light frequencies which can cause the atomic transition to occur), and I_{Sat} is the resonant saturation intensity (the maximum intensity that can be applied for a photon to still find the atom in the ground state after excitation from the previous photon). The coordinate $\mathbf{r}_\perp$ lies in the plane perpendicular to the laser field's axis of propagation. Expanding the logarithm to first order, and assuming $(2\Delta/\Gamma^2)^2 \gg 1$, this potential can be rewritten as:

$$V(\mathbf{r}_\perp) = \frac{\hbar\Gamma^2}{8\Delta}\left(\frac{I(\mathbf{r}_\perp)}{I_{\mathrm{Sat}}}\right) \quad . \tag{2.2}$$

The intensity of a Laguerre-Gaussian beam as a function of the radial coordinate is [29]:

$$I_{p,\ell}(r) = \frac{2p!}{(p+|\ell|)!}\frac{P_0}{\pi w_{p,\ell}^2}\left(\frac{2r^2}{w_{p,\ell}^2}\right)^{|\ell|} e^{\frac{-2r^2}{w_{p,\ell}^2}}\left[L_p^{|\ell|}\left(\frac{2r^2}{w_\ell^2}\right)\right]^2 \tag{2.3}$$

where $w_{p,\ell}$ is the laser beam spot size (i.e. the radius at the focus of the beam) for a given mode with indices p and ℓ. For a beam with one ring of high intensity, $p=0$, and the Laguerre polynomial $L_p^{|\ell|}$ is equal to 1, thus simplifying the intensity expression:

$$I_\ell(r) = \frac{2P_0}{|\ell|!\pi w_\ell^2}\left(\frac{2r^2}{w_\ell^2}\right)^{|\ell|} e^{\frac{-2r^2}{w_\ell^2}} \quad . \tag{2.4}$$

To describe a trap with a radius of r_{T} from the axis of propagation to the peak in intensity, we substitute the following relation between spot size and radius into the intensity expression.

$$w_\ell = r_{\mathrm{T}}\sqrt{\frac{2}{\ell}} \tag{2.5}$$

The intensity can then be expressed in terms of the normalised radius, $\rho = r/r_{\mathrm{T}}$:

$$\tilde{I}_\ell(\rho) = \frac{P_0 e^{-1}}{r_{\mathrm{T}}^2}\frac{\ell^{\ell+1}}{\ell!}e^{1-\rho^2\ell}\rho^{2\ell} \quad . \tag{2.6}$$

Comparing this with equation (2.2) we can define a parameter U_1 which characterises the strength of the optical dipole potential:

$$U_1 = \frac{\hbar\Gamma^2}{8\Delta}\frac{e^{-1}P_0}{\pi r_{\mathrm{T}}^2 I_{\mathrm{Sat}}} \quad . \tag{2.7}$$

The optical dipole potential created by the Laguerre-Gaussian beam is then given by:

$$\tilde{V}_\ell(\rho) = U_1\frac{\ell^{\ell+1}}{\ell!}e^{1-\rho^2\ell}\rho^{2\ell} \quad . \tag{2.8}$$

2.2 Double-ring optical trap for BECs

A single Laguerre-Gaussian laser beam with $p = 1$ could in theory be used to create a trap confining an atomic BEC in two concentric rings. However, due to the Gaussian decay, this double-ring potential would be highly asymmetric. We wish to include the effects of quantum mechanical tunneling of atoms between the inner and outer rings in such a system. In order to maximise this tunneling the rings should be as symmetric as possible, so the single laser beam double ring trap is far from ideal. Instead, we propose creating a double ring trap using a combination of two Laguerre-Gaussian beams.

By altering the laser beams' spot size, it is possible to produce confining potentials from different ℓ modes which have their maxima at the same radial position. We can then use the above parametrization to describe beams of any mode with their intensity maxima at $\rho = 1$. A combination of two oppositely detuned $p = 0$ beams produces a double-ring potential. It has been found that a superposition of a red-detuned beam of index $\ell = 3$, and a blue-detuned beam of index $\ell = 6$ produces a reasonably symmetric potential [32]. We notate this potential as:

$$U(\rho) = \tilde{V}_1(\rho) + \alpha\tilde{V}_2(\rho) \tag{2.9}$$

where $\tilde{V}_1$ and $\tilde{V}_2$ are the potentials produced by the two Laguerre-Gaussian beams, described by equation (2.8). The constant α is chosen so that the potential is zero at $\rho = 1$. This constant is calculated from the following equation:

$$\alpha = \frac{-\tilde{V}_1(\rho = 1)}{\tilde{V}_2(\rho = 1)} \tag{2.10}$$

and we find that $\alpha = 5e^3/144 \approx 0.7$. Thus our double ring potential is given by:

$$U(\rho) = U_1\left(\frac{-27e^{1-3\rho^2}\rho^6}{2} + \frac{27e^{4-6\rho^2}\rho^{12}}{2}\right) \quad . \tag{2.11}$$

The optical dipole potentials of the two individual beams are plotted in Fig. 2.1 and Fig. 2.2, taking $U_1 = 1$. Fig. 2.3 shows the resulting double ring potential given by equation (2.11), also taking $U_1 = 1$. We assume that there is some additional tight confinement along the z-axis, so that we can consider the condensate to be effectively two-dimensional. This confinement could be provided by so-called 'plugging beams' [33] above and below the condensate.

We take the same values for the parameters in equation (2.7) as those given in Wright et al. [29]: a laser power of $P_0 = 1$ mW, resonant saturation intensity $I_{\mathrm{Sat}} = 63\ \mathrm{Wm}^{-2}$, a potential radius of $r_{\mathrm{T}} = 10\ \mu$m, and the natural linewidth of the optical transition $\Gamma = 2\pi \times 9.89$ MHz (for sodium). The laser wavelength is 985 nm, and the transition wavelength of sodium is 589 nm. This corresponds to a detuning of $\Delta = 2\pi \times 7.57 \times 10^8$ MHz. With these parameters, U_1 has a value of 1.4×10^{-8} K, and the trap described has a radius of approximately 25 μm.

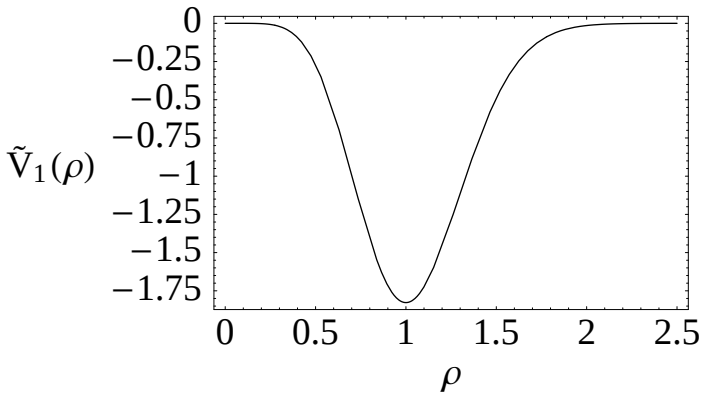

Figure 2.1: Normalised (attractive) optical dipole potential produced by red-detuned $\ell = 3$ Laguerre-Gaussian beam, defined in equation (2.8) with $U_1 = 1$.

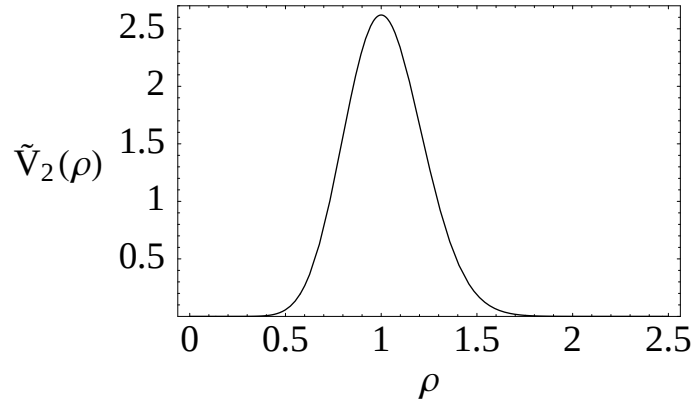

Figure 2.2: Normalised (repulsive) optical dipole potential produced by blue-detuned $\ell = 6$ Laguerre-Gaussian beam, defined in equation (2.8) with $U_1 = 1$

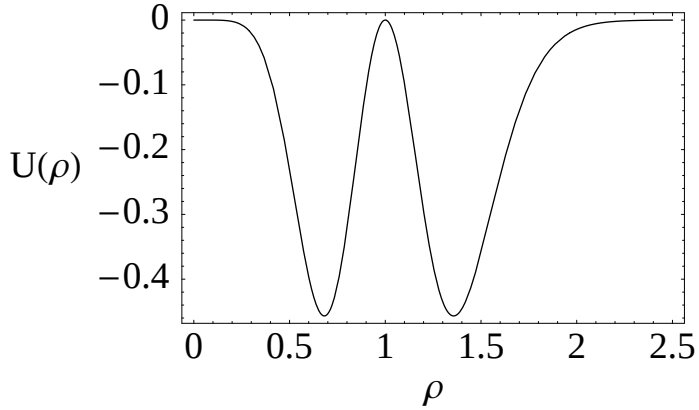

Figure 2.3: Normalised double-ring potential formed by superposition of two Laguerre-Gaussian beams: $U(\rho) \approx U_1(\tilde{V}_1 + 0.7 \times \tilde{V}_2)$, with $U_1 = 1$

2.3 Dimensionless Gross-Pitaevskii equation

The time-independent Gross-Pitaevskii equation in the rotating frame, and in cylindrical coordinates, is:

$$\mu\psi(r) = \left(\frac{-\hbar^2}{2Mr_T^2}\left[\frac{1}{r}\frac{\partial}{\partial r}r\frac{\partial}{\partial r} + \frac{1}{r^2}\frac{\partial^2}{\partial r^2}\right] + V_{\text{ext}}(r) + gN|\psi(r)|^2 + i\hbar\Omega\frac{\partial}{\partial\theta}\right)\psi(r) \tag{2.12}$$

where Ω is the rotational frequency of the trapping potential V_{ext}. The cylindrical symmetry of the system suggests that the density of the ground state should remain a function of the radial coordinate only. However, it is possible for the phase of the wavefunction to be a function of the angular coordinate since the phase does not contribute to the density. The wavefunction can then be written as:

$$\psi(r,\theta) = \phi(r)e^{iS(\theta)} \quad . \tag{2.13}$$

We define a dimensionless radial parameter $\rho = r/r_{\text{T}}$, where r_{T} is the radial distance from the centre of the trap to the top of the potential barrier dividing the two rings. We also define a scaled wavefunction $\varphi(\rho)$, where $\varphi(\rho) = \sqrt{2\pi}r_{\text{T}}\phi(r)$. This definition of the wavefunction can be obtained by considering the normalization of the unscaled wave function:

$$\int\int |\psi(r,\theta)|^2\ r dr\ d\theta = 1 \tag{2.14}$$

and requiring the following normalization of the wave function in dimensionless units:

$$\int |\ \varphi(\rho)\ |^2\ \rho d\rho = 1 \tag{2.15}$$

Making these substitutions and multiplying through by $\sqrt{2\pi}r_{\text{T}}$, we find:

$$\begin{aligned}\mu\varphi(\rho)e^{iS(\theta)} \quad = \quad & \left(\frac{-\hbar^2}{2Mr_{\text{T}}^2}\left[\frac{1}{\rho}\frac{\partial}{\partial\rho}\rho\frac{\partial}{\partial\rho} + \frac{1}{\rho^2}\frac{\partial^2}{\partial\theta^2}\right] + U(\rho)\right. \\ & \left. + \frac{gN}{2\pi r_{\text{T}}^2}|\varphi(\rho)|^2 + i\hbar\Omega\frac{\partial}{\partial\theta}\right)\varphi(\rho)e^{iS(\theta)} \quad . \end{aligned} \tag{2.16}$$

We then divide through by an energy, $\varepsilon_{\text{T}} = \hbar^2/2Mr_{\text{T}}^2$. This scaling energy is chosen because it is essentially the order of magnitude of the kinetic energy per atom when defined in the dimensionless radial coordinate. Dividing through by this scaling energy means that the prefactor of the gradient operator becomes 1. Assuming sodium atoms, and a trap radius of $r_{\text{T}} = 10\ \mu$m, this energy is 1.05×10^{-10}K.

$$\tilde{\mu}\varphi(\rho)e^{iS(\theta)} = \left(-\frac{1}{\rho}\frac{\partial}{\partial\rho}\rho\frac{\partial}{\partial\rho} - \frac{1}{\rho^2}\frac{\partial^2}{\partial\theta^2} + \tilde{U}(\rho) + \eta N|\varphi(\rho)|^2 + i\tilde{\Omega}\frac{\partial}{\partial\theta}\right)\varphi(\rho)e^{iS(\theta)} \tag{2.17}$$

$\tilde{\Omega}$ is the scaled frequency, given by $\hbar\Omega/\varepsilon_{\text{T}}$. The effective interaction parameter is now $\eta = gM/\hbar^2\pi$, and $\tilde{\mu}$ is the scaled chemical potential, $\mu/\varepsilon_{\text{T}}$. All chemical potentials and energies calculated in the following will be in units of ε_{T}. $\tilde{U}(\rho)$ is the scaled double-ring potential, given by $\tilde{U}(\rho) = U(\rho)/\varepsilon_{\text{T}}$. This evaluates to:

$$\tilde{U}(\rho) = 253\left(-27e^{1-3\rho^2}\rho^6 + 27e^{4-6\rho^2}\rho^{12}\right) \quad . \tag{2.18}$$

Chapter 3

Ground States of Double-Ring BEC - General Theory

We derive a two-state model for a double-ring condensate, where the double-ring wave function can be written as a linear superposition of the separate ring wave functions. Using a specific double-ring potential, ground and first excited state solutions are found by analytic and numerical methods. These results allow us to test our two-state model, which is found to be an adequate description of the system. The two-state model has the advantage of allowing us to estimate the tunnel coupling for a particular potential, $\tilde{U}(\rho)$, and hence to estimate the characteristic time scale for changes to the condensate due to tunneling.

3.1 Derivation of two-state model for double ring BECs

We make the following ansatz for the wave function in the double ring:

$$\varphi(\rho) = c_{\mathrm{i}}\varphi_{\mathrm{i}}(\rho)e^{i\phi_{\mathrm{i}}} + c_{\mathrm{o}}\varphi_{\mathrm{o}}(\rho)e^{i\phi_{\mathrm{o}}} \tag{3.1}$$

where the real constants $c_{\mathrm{i/o}}$ are chosen to ensure the correct normalization of the wave function, and the subscripts i and o refer to the inner and outer rings respectively. The wave functions $\varphi_{\mathrm{i}}(\rho)$ and $\varphi_{\mathrm{o}}(\rho)$ are the ground state wave functions of the condensate confined in the isolated inner and outer ring, and $\phi_{\mathrm{i/o}}$ are the absolute phases of the wave functions in each ring. These wave functions satisfy the normalization condition:

$$\int |\varphi_{\mathrm{i/o}}|^2 \rho d\rho = 1 \quad . \tag{3.2}$$

For the non-rotating case, where the phase or the order parameter does not vary as a function of the coordinate θ, the Gross-Pitaevskii equation in dimensionless units is:

$$\tilde{\mu}\varphi = -\nabla^2\varphi + \tilde{U}(\rho)\varphi + \eta N|\varphi|^2\varphi \quad . \tag{3.3}$$

Two coupled equations can be derived after substituting the ansatz from equation (3.1) into the Gross-Pitaevskii equation. The first is obtained by multiplying through by φ_{i}^* and integrating over all ρ; the second by multiplying through by φ_{o}^* then integrating. Assuming the overlap between the two wave functions is small, we can

neglect terms arising from the non-linear interaction containing both wave functions. The normalization of $\varphi_{\mathrm{i/o}}$ also simplifies the equations.

$$\begin{aligned}\tilde{\mu}c_{\mathrm{i}} &= c_{\mathrm{i}}\int \varphi_{\mathrm{i}}^{*}\left(-\nabla^{2}+\tilde{U}(\rho)+\eta N c_{\mathrm{i}}^{2}\varphi_{\mathrm{i}}^{2}\right)\varphi_{\mathrm{i}}\rho d\rho \\ &\qquad +c_{\mathrm{o}}\int \varphi_{\mathrm{i}}^{*}\left(-\nabla^{2}+\tilde{U}(\rho)\right)\varphi_{\mathrm{o}}\rho d\rho \end{aligned} \tag{3.4}$$

$$\begin{aligned}\tilde{\mu}c_{\mathrm{o}} &= c_{\mathrm{o}}\int \varphi_{\mathrm{o}}^{*}\left(-\nabla^{2}+\tilde{U}(\rho)+\eta N c_{\mathrm{o}}^{2}\varphi_{\mathrm{o}}^{2}\right)\varphi_{\mathrm{o}}\rho d\rho \\ &\qquad +c_{\mathrm{i}}\int \varphi_{\mathrm{o}}^{*}\left(-\nabla^{2}+\tilde{U}(\rho)\right)\varphi_{\mathrm{i}}\rho d\rho \end{aligned} \tag{3.5}$$

We define the following terms:

$$\tilde{\mu}_{\mathrm{i}} = \int \varphi_{\mathrm{i}}^{*}\left(-\nabla^{2}+\tilde{U}(\rho)+\eta N c_{\mathrm{i}}^{2}|\varphi_{\mathrm{i}}|^{2}\right)\varphi_{\mathrm{i}}\rho d\rho \quad , \tag{3.6}$$

$$\tilde{\mu}_{\mathrm{o}} = \int \varphi_{\mathrm{o}}^{*}\left(-\nabla^{2}+\tilde{U}(\rho)+\eta N c_{\mathrm{o}}^{2}|\varphi_{\mathrm{o}}|^{2}\right)\varphi_{\mathrm{o}}\rho d\rho \quad , \tag{3.7}$$

$$\kappa = -\int \varphi_{\mathrm{o/i}}^{*}\left(-\nabla^{2}+\tilde{U}(\rho)\right)\varphi_{\mathrm{i/o}}\rho d\rho \quad . \tag{3.8}$$

$\tilde{\mu}_{\mathrm{i}}$ and $\tilde{\mu}_{\mathrm{o}}$ are the reduced chemical potentials of the individual ring ground states. The two equations can then be written as a matrix equation in terms of $\tilde{\mu}_{\mathrm{i/o}}$ and κ.

$$\begin{bmatrix} \tilde{\mu}_{\mathrm{i}} & -\kappa e^{-i\phi_{\mathrm{rel}}} \\ -\kappa e^{i\phi_{\mathrm{rel}}} & \tilde{\mu}_{\mathrm{o}} \end{bmatrix}\begin{bmatrix} c_{\mathrm{i}} \\ c_{\mathrm{o}} \end{bmatrix} = \tilde{\mu}\begin{bmatrix} c_{\mathrm{i}} \\ c_{\mathrm{o}} \end{bmatrix} \tag{3.9}$$

We have defined a relative phase, $\phi_{\mathrm{rel}} = \phi_{\mathrm{o}} - \phi_{\mathrm{i}}$. The off-diagonal element, κ, is the tunnel coupling. It describes transitions between the inner and outer ring states which can occur through quantum tunneling. With the definition in equation (3.8), κ must be positive to ensure that the ground state is symmetric (see Section 1.3.2). Our double-ring system has now been reduced to a two-state model. The chemical potential of the double-ring ground and first excited states are then given by (see equation (1.10)):

$$\tilde{\mu}_{\pm} = \frac{\tilde{\mu}_{\mathrm{i}}+\tilde{\mu}_{\mathrm{o}}}{2} \pm \sqrt{|\kappa|^{2}+\left(\frac{\tilde{\mu}_{\mathrm{i}}-\tilde{\mu}_{\mathrm{o}}}{2}\right)^{2}} \quad . \tag{3.10}$$

Taking the ground state equation and rearranging, we find that the absolute value of tunnel coupling is given by:

$$|\kappa|^{2} = \left(\tilde{\mu}_{-}-\frac{\tilde{\mu}_{\mathrm{i}}-\tilde{\mu}_{\mathrm{o}}}{2}\right)^{2} - \left(\frac{\tilde{\mu}_{\mathrm{i}}-\tilde{\mu}_{\mathrm{o}}}{2}\right)^{2} \quad . \tag{3.11}$$

Thus the tunnel coupling can be calculated if $\tilde{\mu}_{-}$, $\tilde{\mu}_{\mathrm{i}}$ and $\tilde{\mu}_{\mathrm{o}}$ are known. From this, we can also calculate $\tilde{\mu}_{+}$, the chemical potential of the first excited state. We define the level splitting, $\Delta\tilde{\mu}$, as the energy gap between the ground state and first excited state.

$$\tilde{\mu}_{\pm} = \frac{\tilde{\mu}_{\mathrm{i}}+\tilde{\mu}_{\mathrm{o}}}{2} \pm \frac{\Delta\tilde{\mu}}{2} \tag{3.12}$$

3.2 Ground state solutions

Appendix A contains the two methods used to determine the ground state of the condensate. The first is the approximate Thomas Fermi method, which gives an analytic solution. The second is a numerical energy minimisation using a discretisation along the co-ordinate ρ. As expected, the numerical minimisation process yields discretised wave functions which are smooth and tend to zero as ρ becomes large. As well as solving for the ground state of the condensate confined in the double ring potential, we also solve for the ground state of the condensate confined in each of the inner and outer rings separately. In the numerical method, the discretised potential used for the inner ring was valued at $U(\rho)$ at grid points along ρ between 0 and 1, then zero valued for $\rho > 1$. Similarly the potential used for the outer ring solution was zero valued for $\rho < 1$ and then valued at $U(\rho)$ for larger radial distances. Fig. 3.1, 3.2, and 3.3 show the Thomas Fermi, and the numerically determined ground state density distributions for the condensate confined in the three different configurations. The interaction strength used was $\eta N = 50/\pi$ (this corresponds to a condensate of ≈16000 atoms if one takes $\eta \approx 10^{-3}$ as suggested in [29]).

The Thomas Fermi solution overestimates the peak densities in all cases, and does not provide a realistic density distribution which decreases smoothly as the confining potential weakens. This is because the shape of the density profile in the Thomas Fermi model is determined by the inverted shape of the confining potential (see Appendix A). In the double-ring solution, the Thomas Fermi density profile has peaks of equal density in each ring due to the confining potential having equal depth in each ring. Table 3.1 shows the chemical potentials of the ground state calculated using the Thomas Fermi and numerical methods. The Thomas Fermi chemical potentials are more negative than those found by full numerical integration of the Gross-Pitaevskii equation, and this is to be expected as the Thomas Fermi approximation neglects the positive kinetic energy contribution to the overall energy.

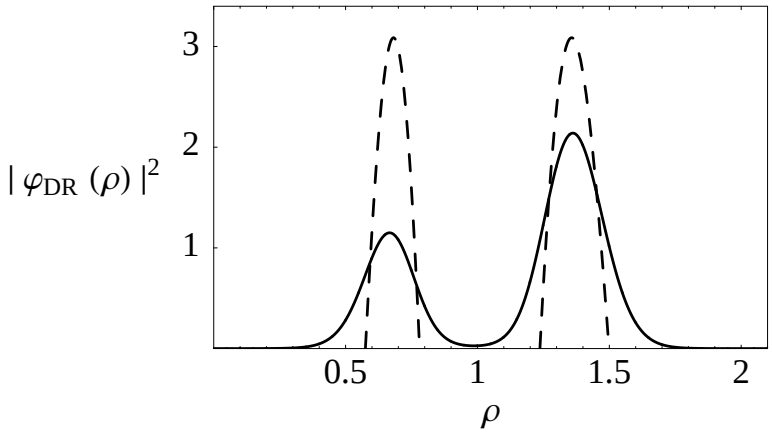

Figure 3.1: Condensate density along radial coordinate when confined in double ring potential, $\tilde{U}(\rho)$, for an interaction strength $\eta = 10^{-3}$ and a condensate of $N \approx 16000$ atoms (dashed line - Thomas Fermi solution, solid line - numerical solution).

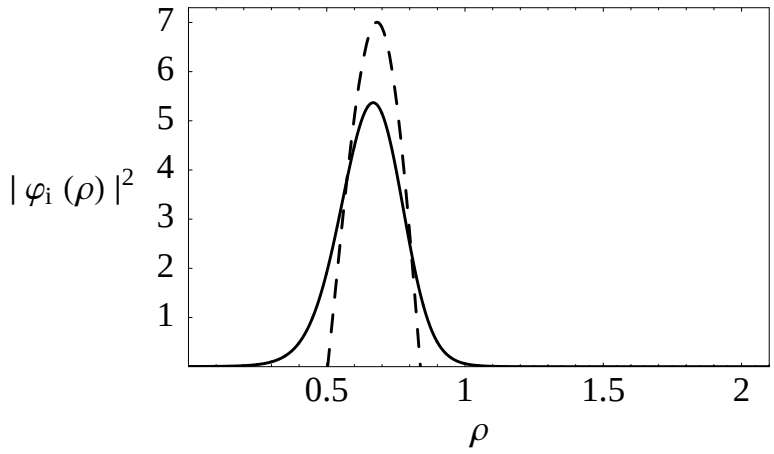

Figure 3.2: Condensate density when confined in inner ring only, for an interaction strength $\eta = 10^{-3}$ and a condensate of $N \approx 16000$ atoms (dashed line - Thomas Fermi solution, solid line - numerical solution). Inner ring potential is $\tilde{U}(\rho)$ for $\rho \leq 1$ and zero for $\rho > 1$.

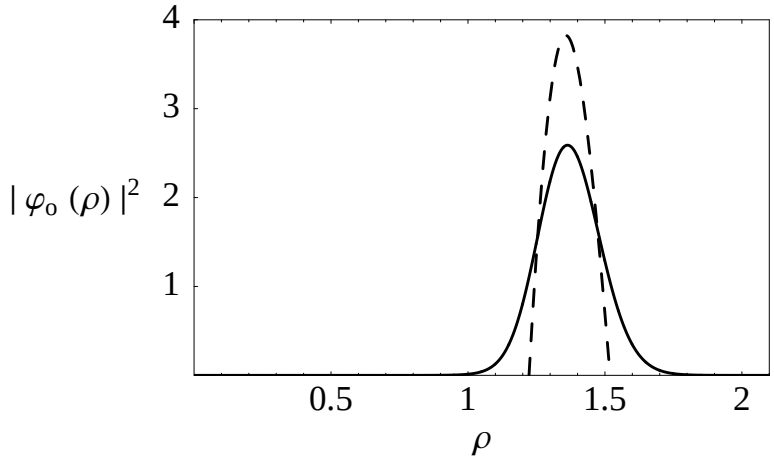

Figure 3.3: Condensate density when confined in outer ring only, for an interaction strength $\eta = 10^{-3}$ and a condensate of $N \approx 16000$ atoms (dashed line - Thomas Fermi solution, solid line - numerical solution). Outer ring potential is zero for $\rho \leq 1$, and $\tilde{U}(\rho)$ for $\rho > 1$.

	Thomas Fermi Solution	Full Solution
Inner ring	-119.641	-104.268
Outer ring	-170.256	-149.712
Double ring	-181.984	-155.177

Table 3.1: Chemical potential of the ground state of a condensate confined in double ring, and confined separately in the inner and the outer rings, in units of ε_{T}.

3.3 Validity of two-state model for double-ring BEC

3.3.1 Checking validity of two-state model

In the two-state approximation, the ground and first excited states can be written as a sum and difference respectively of the inner and outer ring states. The amplitudes of the two basis states can be found by solving for c_i from:

$$\varphi_{\pm} = \mp c_{\mathrm{i}}\varphi_{\mathrm{i}} + \sqrt{1 - c_{\mathrm{i}}^2}\varphi_{\mathrm{o}} \tag{3.13}$$

where $\varphi_{\pm}$ is the ground or first excited state wave function. We find the difference between the numerical double ring wave function and the wave function formed from a linear superposition of the individual ring wave functions. Taking the sum of the squares of this difference at each grid point, and minimising this sum with respect to c_{i}, we find a best-fit ground state wave function:

$$\varphi_{-} \approx 0.43\varphi_{\mathrm{i}} + 0.90\varphi_{\mathrm{o}} \quad . \tag{3.14}$$

Fig. 3.4 shows the corresponding density profile, and the density profile of the condensate found numerically for the double ring potential. There is reasonably good agreement between the two profiles.

The numerical method can be extended to solve for the first excited state, which we can then use as a further test of the two-state approximation. The first excited state can be approximate by an antisymmetric superposition of φ_{i} and φ_{o}. Again, minimising the sum of the squares of the differences between the double ring wave function and the superposition wave function at all grid points allows us to solve for the relative contributions of the individual ring wave functions. We hence find:

$$\varphi_{+} \approx -0.41\varphi_{\mathrm{i}} + 0.91\varphi_{\mathrm{o}} \quad . \tag{3.15}$$

Fig. 3.5 shows the corresponding density profile as well as the numerically determined double ring first excited state.

Both the similarity of the coefficients in the approximate φ_{+} and φ_{-} wave functions and the visual similarity of the density profiles give us confidence in the two-state approximation. A further test is to calculate the first excited state chemical potential from the ground and individual ring chemical potentials. Using equation (3.11), we calculate the tunnel coupling to be $\kappa = 0.598$. The level splitting is then $\Delta\tilde{\mu} = 1.868$, which corresponds to a first excited state chemical potential of -153.308 (and an energy of -165.406). The numerically determined first excited state chemical potential was found to be -154.181, which is reasonably close. This first excited state has a node positioned at $\rho = 0.98$, and the wave function is normalised to 0.9999787 (7 d.p.). The tunnel coupling of 0.598 is in units of the scaling energy ε_{T}. Converting this to real units again, we can calculate the frequency that this energy corresponds to. This gives an estimate of the time scale in which changes could occur to the condensate due to tunneling. This time scale is ≈ 0.12 seconds, which is suitable given the lifetime of condensates in current experiments.

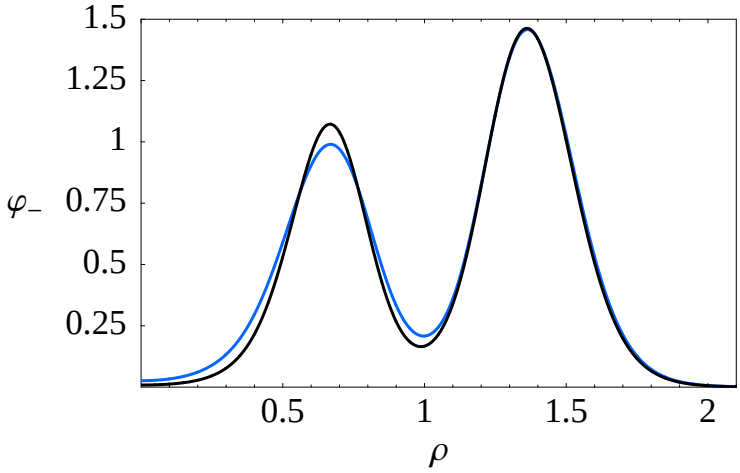

Figure 3.4: Ground state wave function for condensate confined in double ring potential, $\tilde{U}(\rho)$. Black is the numerically determined solution, blue is the wave function in the two-state approximation, given by $\varphi_- \approx 0.43\varphi_\mathrm{i} + 0.90\varphi_\mathrm{o}$.

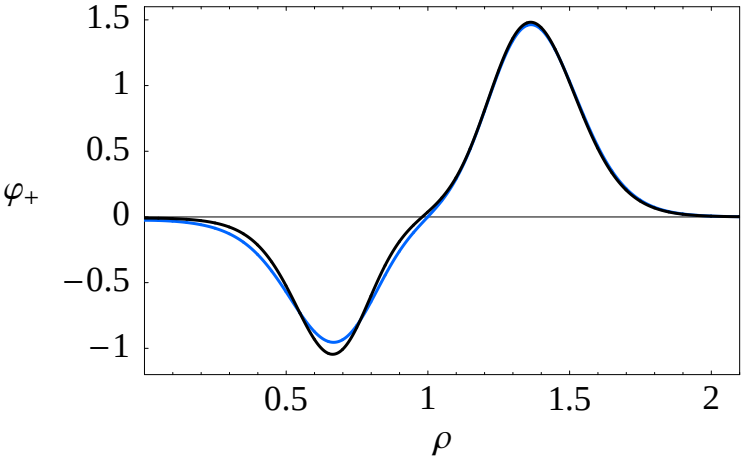

Figure 3.5: First excited state for condensate confined in double ring potential, $\tilde{U}(\rho)$ determined from numerical method (black line), and from two-state approximation (blue line), given by $\varphi_+ \approx -0.41\varphi_\mathrm{i} + 0.91\varphi_\mathrm{o}$.

3.3.2 Two-state model and Thomas Fermi approximation

The chemical potentials found from the analytic Thomas Fermi approximation can also be used to obtain another estimate of the tunnel coupling. However, for this particular potential the Thomas Fermi method fails, giving a complex value for the tunnel coupling. Under this model, we find that the reduced chemical potential of the inner ring solution lies below the lowest energy of the confining potential, and well below the ground state chemical potential. The two-state model describes a system whereby the coupling results in a splitting of the energy levels, which clearly is not the case here. Thus the Thomas Fermi approximation seems to be of value only in providing a reasonably good initial condition for the full numerical integration.

Chapter 4

Ground States in Rotating Double-Ring Trap

Ground state solutions for a condensate in the double-ring trap are determined for a range of frequencies and tunnel couplings. From studying the angular momentum of the ground states, we find that at low tunnel coupling interesting solutions exist where atoms in each ring have a different expectation value of angular momentum. These states contain Josephson vortices, which can be identified by their phase and density structure from the numerical results. A variational model is presented which provides an approximate calculation of the angular momentum of the ground states. This model also illustrates the competition which exists between the rotation and tunnel coupling in the energy minimisation of the ground states. The influence of non-linear interactions is also studied analytically, and it is shown that interactions are necessary for Josephson vortices to exist in the ground state solutions.

4.1 Introduction

In this study we solve for the ground states of a Bose-Einstein condensate in the double-ring trap as a function of the rotational frequency and the tunnel coupling. If a finite tunnel coupling exists, at least some atoms in each ring would be expected to carry the same angular momentum, since tunneling conserves angular momentum. A stronger tunnel coupling would increase the likelihood of the same angular momentum modes being occupied in each ring. This is in contrast to the behaviour of the individual rings under rotation, where, as shown below, there are different preferred angular momentum modes for each ring at nearly all frequencies.

To consider states where only one angular momentum mode is occupied we use the ansatz:

$$\psi(\rho,\theta) = \varphi(\rho)e^{im\theta} \quad . \tag{4.1}$$

The energy functional in the rotating frame, for correctly normalized $\varphi(\rho)$, is then:

$$E = \int \left[\varphi^*(\rho)\left(-\frac{1}{\rho}\frac{\partial}{\partial\rho}\rho\frac{\partial}{\partial\rho} + \frac{m^2}{\rho^2} + \tilde{U}(\rho) + \frac{\eta N}{2}|\varphi(\rho)|^2\right)\varphi^*(\rho)\right]\rho d\rho - m\tilde{\Omega} \tag{4.2}$$

and the dimensionless time-independent Gross-Pitaevskii equation is:

$$\tilde{\mu}\varphi(\rho) = \left[-\frac{1}{\rho}\frac{\partial}{\partial\rho}\rho\frac{\partial}{\partial\rho} + \frac{m^2}{\rho^2} + \tilde{U}(\rho) + \eta N|\varphi(\rho)|^2 - m\tilde{\Omega}\right]\varphi(\rho) \quad . \tag{4.3}$$

From equation (4.2) we see that the energy of a state at a finite rotational frequency $\tilde{\Omega}$ can be calculated if the energy of that state at zero frequency is known. Thus we can use the same numerical energy minimisation procedure as in Section 3.2.2 to solve for wavefunctions corresponding to each m value at zero frequency. We can then plot the energies of these states as a function of frequency. As an example, the energies of double-ring states having angular momentum from 0 to 4 are plotted in Fig. 4.1. After these energy calculations, the ground state as a function of frequency can be determined, since by definition this is the lowest energy state.

As well as using this ansatz to calculate the ground state angular momentum as a function of frequency for the double ring, we can also apply it to the separate ring states used in the two-state model. Fig. 4.2 shows the angular momentum, m, of the ground state as a function of frequency for the three confinements. The number of quanta of angular momentum that minimises the energy at a given frequency is different for the inner and outer rings. This suggests that the ansatz given in equation (4.1) may not always be appropriate for the double-ring system. At zero coupling, the individual rings have ground states with different angular momentum, which means that there may be a transitional region of weak but finite coupling where the double ring ground states still reflect the preferred angular momentum modes of each ring. The ansatz in equation (4.1) assumes that the rings share the same angular momentum, and this discrepancy motivates our more general numerical method and the study of the rotational ground states as a function of the tunnel coupling.

At large frequencies, there is little difference between the critical frequencies of a condensate in the double ring system and those of a condensate confined to the outer ring only. This can be understood when one considers the double ring wavefunctions, which are shown in Fig. 4.3. Here a density transfer to the outer ring is clearly visible as the rotational frequency increases, thus making the double ring wave function similar to the wave function of the condensate when confined in the outer ring only.

Section 4.4 includes an alteration to the trapping potential which compensates for this density shift so that ground states with relatively equal densities in each ring can be found at all frequencies. This is so that the trivial density shift to the outer ring does not mask any interesting effects which may be due to the tunnel coupling.

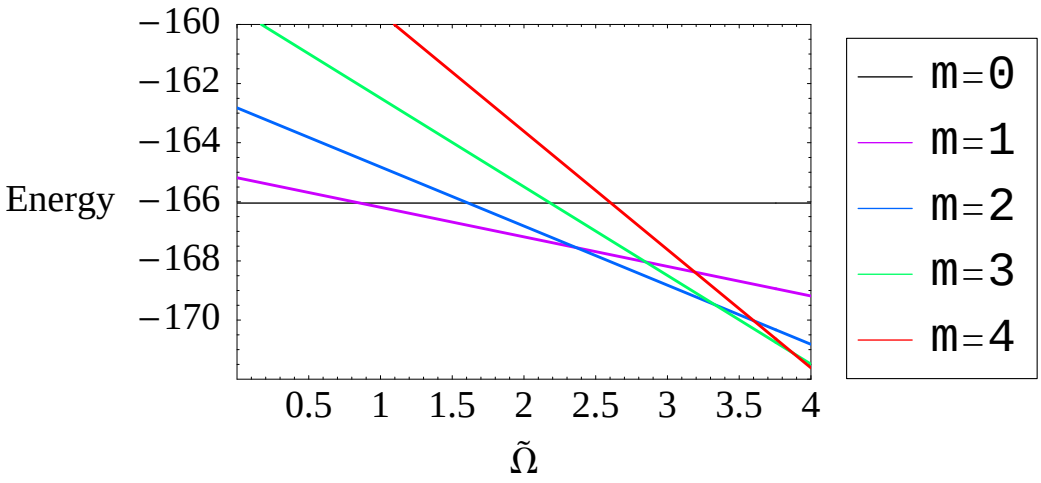

Figure 4.1: Energy of double-ring states in units of ε_{T}, where m is number of quanta of angular momentum carried by all atoms in condensate. Interaction strength $\eta = 10^{-3}$, and $N \approx 16000$. Rotation at finite angular frequencies allows states of finite angular momentum to become the ground (lowest energy) state.

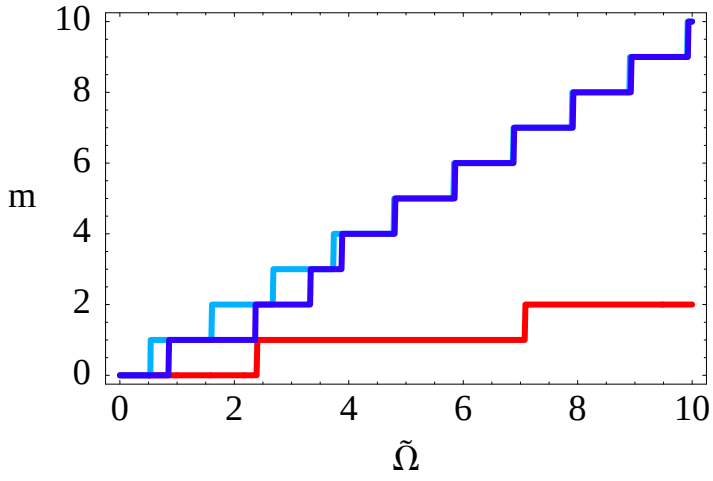

Figure 4.2: Ground state angular momentum (m) of condensate in inner ring (red line), outer ring (light blue line), and double ring (dark blue). Double ring potential given by $\tilde{U}(\rho)$. Interaction strength $\eta = 10^{-3}$, and $N \approx 16000$.

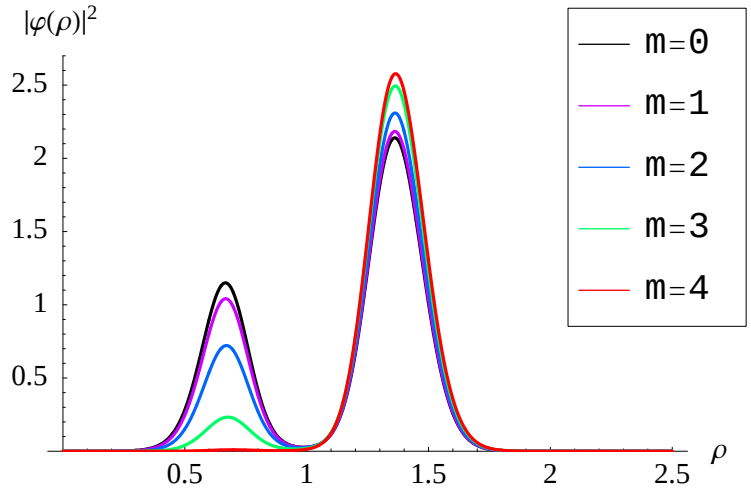

Figure 4.3: Condensate density profiles for states where expectation value of angular momentum for all atoms is given by m. Condensate is confined in the double ring potential, $\tilde{U}(\rho)$. Interaction strength $\eta = 10^{-3}$, and $N \approx 16000$.

4.2 Numerical method

The calculations in Section 4.1 show that there is a noticeable difference in the preferred angular momentum of a condensate when confined in the inner ring or the outer ring, at nearly all finite frequencies. With this in mind, a thorough method of solving for the ground states of the rotating double-ring condensate should allow for the possiblity of ground state solutions where the expectation value of angular momentum of atoms in the inner ring may be different to that of atoms in the outer ring. Our current numerical minimization method can only be used to find states where all atoms in the condensate have the same expectation value of angular momentum. We therefore make a new wavefunction ansatz which does not restrict the occupation of any angular momentum modes. We first separate the radial and angular parts of the wavefunction:

$$\varphi(\rho,\theta) = \phi_{\mathrm{i}}(\rho)\chi_{\mathrm{i}}(\theta) + \phi_{\mathrm{o}}(\rho)\chi_{\mathrm{o}}(\theta) \quad . \tag{4.4}$$

Substituting this into the time-dependent Gross-Pitaevskii equation we can derive two coupled equations by multiplying through by $\phi^*_{\mathrm{i}}(\rho)$ and $\phi^*_{\mathrm{o}}(\rho)$ and integrating both equations over all ρ.

$$i\frac{\partial\chi_{\mathrm{i/o}}}{\partial\tau} = \left[\frac{-1}{\rho^2_{\mathrm{i/o}}}\frac{\partial^2}{\partial\theta^2} \mp \delta + 2\pi\gamma_{\mathrm{i/o}}|\chi_{\mathrm{i/o}}|^2 + i\tilde{\Omega}\frac{\partial}{\partial\theta}\right]\chi_{\mathrm{i/o}} - \kappa\chi_{\mathrm{o/i}} \tag{4.5}$$

The ρ dependent wavefunction integrals have been used to define effective radii for each ring, ρ_{i} and ρ_{o}:

$$\frac{1}{\rho^2_{\mathrm{i/o}}} = \int \frac{1}{\rho}|\phi_{\mathrm{i/o}}|^2 d\rho \quad . \tag{4.6}$$

We can also define effective interaction strengths:

$$\gamma_{\mathrm{i/o}} = \frac{\eta N}{2\pi}\int |\phi_{\mathrm{i/o}}|^4 \rho d\rho \tag{4.7}$$

and a detuning, δ, which contains the contribution from the trapping potential and also the ρ-dependent kinetic energy term, i.e. terms of the form:

$$\int \phi^*_{\mathrm{i/o}} \left(\frac{-1}{\rho} \frac{\partial}{\partial \rho} \rho \frac{\partial}{\partial \rho} + \tilde{U}(\rho) \right) \phi_{\mathrm{i/o}} \rho d\rho \quad . \tag{4.8}$$

We take the zero of energy to be halfway between these two energies, and write $\pm\delta$ for these energy terms of the inner and outer ring states. The term coupling the inner and outer rings is found to be:

$$\kappa = - \int \phi^*_{\mathrm{i/o}} \left(\frac{-1}{\rho} \frac{\partial}{\partial \rho} \rho \frac{\partial}{\partial \rho} + \tilde{U}(\rho) \right) \phi_{\mathrm{o/i}}(\rho) d\rho \quad . \tag{4.9}$$

In our calculations, we assume that the radial wave functions do not change depending on the angular momentum modes that are occupied. In doing this we can use the same values for effective radii, effective interaction strengths, and tunnel coupling at all frequencies. $\chi_{\mathrm{i/o}}$ will, in general, contain contributions from all angular momentum modes:

$$\chi_{\mathrm{i/o}} = \frac{1}{\sqrt{2\pi}} \sum_m \alpha_m^{(\mathrm{i/o})} e^{im\theta} \quad . \tag{4.10}$$

Substituting this ansatz into equation (4.5), we find a system of equations which depend on only one spatial coordinate, the polar angle θ.

$$i \frac{\partial \alpha_m^{(\mathrm{i/o})}}{\partial \tau} = \left[\frac{m^2}{\rho^2_{\mathrm{i/o}}} - \tilde{\Omega} m \mp \delta \right] \alpha_m^{(\mathrm{i/o})} - \kappa \alpha_m^{(\mathrm{o/i})} + \gamma_{\mathrm{i/o}} \sum_{n,n'} \alpha_n^{(\mathrm{i/o})} \alpha_{n'}^{*(\mathrm{i/o})} \alpha_{m-n+n'}^{(\mathrm{i/o})} \tag{4.11}$$

Using this method we can solve for ground states as a function of both frequency and tunnel coupling. Appendix B details the imaginary time propagation used to find the ground state solutions. This method returns a vector containing the amplitudes of each angular momentum mode in the inner and outer ring. The effective interactions are assumed to be the same in each ring, i.e. $\gamma_{\mathrm{i}} = \gamma_{\mathrm{o}}$. We take $\rho_{\mathrm{i}} = 0.8$ and $\rho_{\mathrm{i}} = 1.166$.

4.3 Ground state results - angular momentum

4.3.1 Calculating expectation value of angular momentum

The expectation value of the angular momentum operator for a state, $\varphi(\rho, \theta)$, in our scaled cylindrical coordinates is given by:

$$\langle L_z \rangle = \frac{-i}{\int |\varphi(\rho,\theta)|^2 \rho d\rho d\theta} \int \varphi^*(\rho,\theta) \, \frac{\partial}{\partial\theta} \, \varphi(\rho,\theta) d\theta \quad . \tag{4.12}$$

For the double-ring state, using the two-state ansatz from equation (4.4), and expressing $\chi_{\mathrm{i/o}}(\theta)$ as the sum over all angular momentum modes as in equation (4.10), the expectation value simplifies to:

$$\langle L_z \rangle = \sum_m m \left(|\alpha_m^{\mathrm{i}}|^2 + |\alpha_m^{\mathrm{o}}|^2 \right) \quad . \tag{4.13}$$

assuming correctly normalised radial wave functions. We can also calculate the expectation value of angular momentum for atoms which are localized in the inner or outer rings. The calculation is similar, except that there is a normalisation factor so that the resulting expectation value is still per atom:

$$\langle L_z \rangle_{\mathrm{i/o}} = \frac{\sum_m m |\alpha_m^{\mathrm{i/o}}|^2}{\sum_m |\alpha_m^{\mathrm{i/o}}|^2} \quad . \tag{4.14}$$

4.3.2 Numerical results

Fig. 4.4 plots the expectation value of the angular momentum of the ground states in the double ring, for a non-linear interaction strength of $\gamma = 100$. Solutions were found at intervals of 0.1 along the tunnel coupling axis, and at intervals of 0.2 along the frequency axis. The expectation value of angular momentum for each solution is plotted as a rectangle of dimension 0.1×0.2 and its value is given by the colour bar to the right of the figure.

In the upper left part of Fig. 4.4, where tunnel coupling, κ, is strong, the ground state solutions are such that all atoms in the condensate have the same expectation value of angular momentum. At low tunnel coupling there are areas in the phase plot where the expectation value of angular momentum is not an integer. Since the angular momentum carried by any individual atom must be an integer, these solutions must contain atoms carrying different values of angular momentum. Looking at the occupation of individual m modes for any of these non-integer solutions, we find that the mode with the highest occupation is different for the inner and outer rings, and that there are also multiple modes occupied in each ring. By way of example, Fig. 4.5 shows the occupations of angular momentum for a ground state that has an expectation value of angular momentum of ≈ 1.5. These occupations in Fig. 4.5 represent fractions of the atoms in the condensate which would be expected to circulate with each m quanta of angular momentum, and the expectation value of 1.5 is the expected mean angular momentum per atom in the condensate.

Fig. 4.6 and 4.7 plot the expectation value of angular momentum for atoms in the inner and outer rings respectively for the same ground states. By comparison with the color bar it can be seen that in each ring the expectation value is always close to an integer.

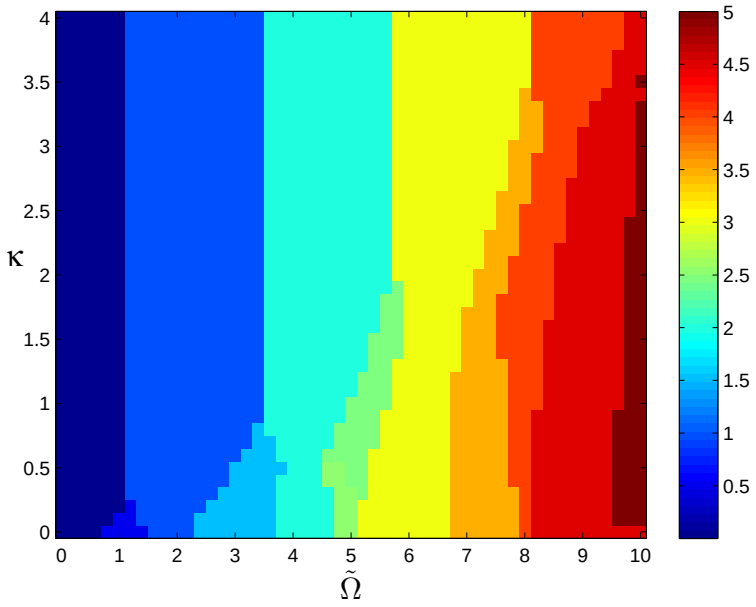

Figure 4.4: Ground state expectation value of angular momentum (see equation (4.13)) of condensate in double-ring, as a function of tunnel coupling, κ, and scaled rotational frequency, $\tilde{\Omega}$. Effective radii are $\rho_{\mathrm{i}} = 0.8$ and $\rho_{\mathrm{o}} = 1.166$, interaction strength is $\gamma_{\mathrm{i/o}} = 100$. Detuning varies with frequency as $\delta = (1/8)\tilde{\Omega}^2(\rho_{\mathrm{o}}^2 - \rho_{\mathrm{i}}^2)$.

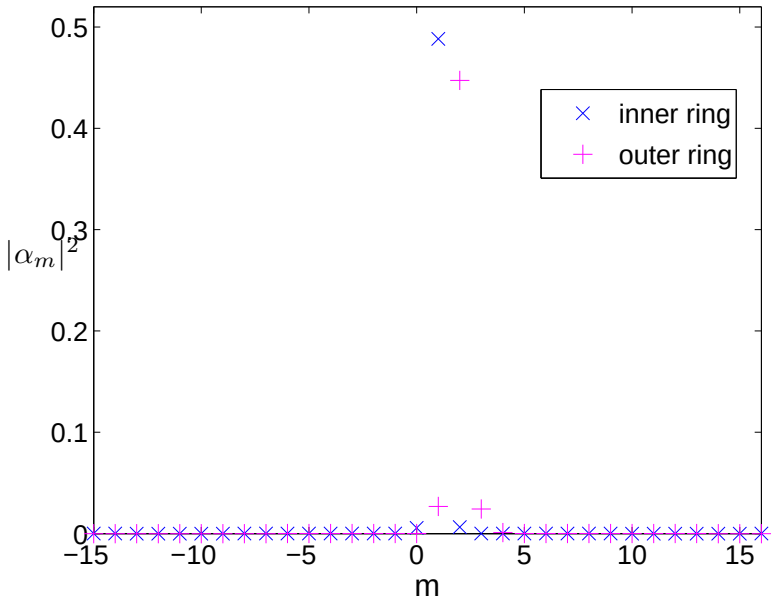

Figure 4.5: Occupation of angular momentum modes for the ground state at scaled rotational frequency of $\tilde{\Omega} = 3.4$ and tunnel coupling of $\kappa = 0.4$, interaction strength $\gamma_{\mathrm{i/o}} = 100$. Expectation value of angular momentum in inner ring is $\langle L_z \rangle_{\mathrm{i}} \approx 1$, in outer ring it is $\langle L_z \rangle_{\mathrm{o}} \approx 2$ (see equation (4.14)). Expectation value of angular momentum per atom in double ring is $\langle L_z \rangle \approx 1.5$.

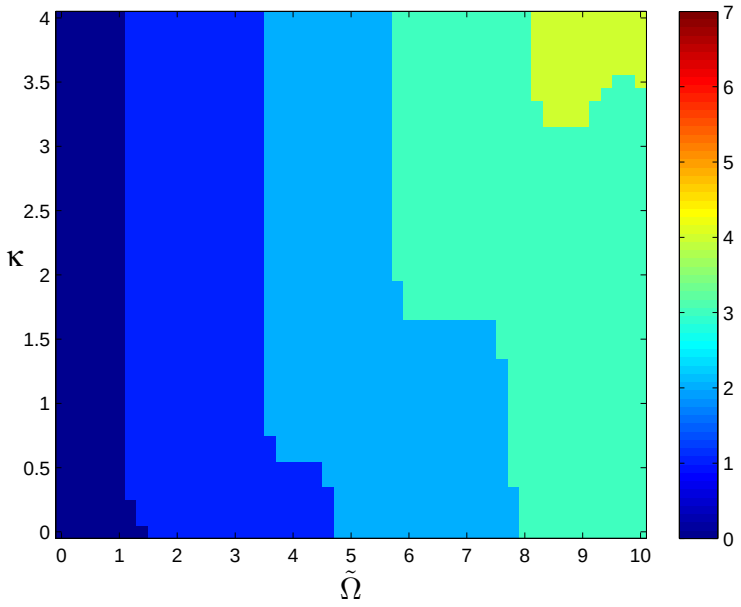

Figure 4.6: Ground state expectation value of angular momentum for atoms in inner ring (see equation (4.14)), as a function of tunnel coupling, κ, and scaled rotational frequency $\tilde{\Omega}$. Effective radii are $\rho_{\mathrm{i}} = 0.8$ and $\rho_{\mathrm{o}} = 1.166$, interaction strength is $\gamma_{\mathrm{i/o}} = 100$. Detuning varies with frequency as $\delta = (1/8)\tilde{\Omega}^2(\rho_{\mathrm{o}}^2 - \rho_{\mathrm{i}}^2)$.

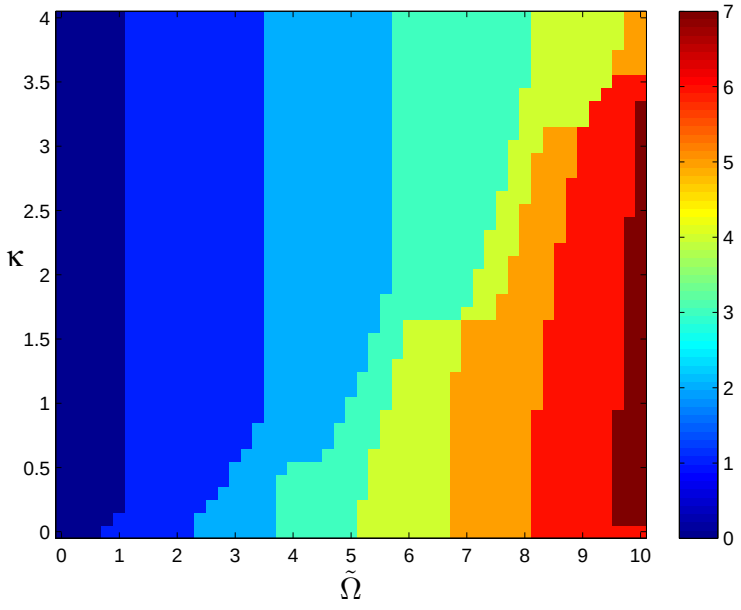

Figure 4.7: Ground state expectation value of angular momentum for atoms in outer ring, as a function of tunnel coupling, κ, and scaled rotational frequency $\tilde{\Omega}$. Effective radii are $\rho_{\mathrm{i}} = 0.8$ and $\rho_{\mathrm{o}} = 1.166$, interaction strength is $\gamma_{\mathrm{i/o}} = 100$. Detuning varies with frequency as $\delta = (1/8)\tilde{\Omega}^2(\rho_{\mathrm{o}}^2 - \rho_{\mathrm{i}}^2)$.

Fig. 4.8 plots the difference in angular momentum between the outer and inner rings. This highlights where the most interesting ground states occur. Ground states which are coloured dark blue have the same expectation value of angular momentum for all atoms, regardless of which ring the atom is localised in. These are solutions which can be described by the simple wavefunction ansatz $\varphi(\rho)e^{im\theta}$. For states where there is a difference in expectation value between the two rings, Fig. 4.8 shows that these differences are close to integer values. These states contain structural features which we identify as Josephson vortices.

The description of Josephson vortices is left until Section 4.7. This is because the discussion of ground state solutions in the following sections can be understood in terms of the angular momentum distribution, and the exact structure of Josephson vortices is not needed. For now, it is sufficient to know that each Josephson vortex accounts for a difference in expectation value of angular momentum of approximately 1 between the inner and outer rings.

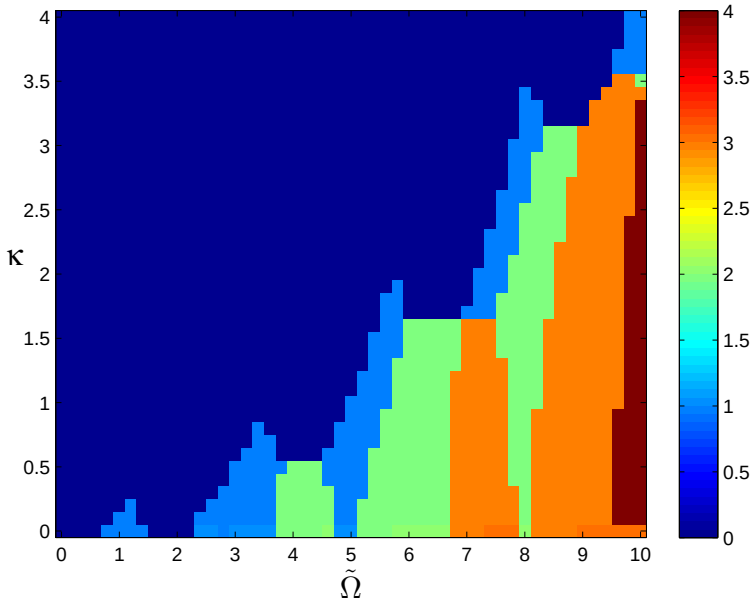

Figure 4.8: Difference in expectation value of angular momentum between atoms in outer ring and atoms in inner ring in the ground state, as a function of tunnel coupling, κ, and scaled rotational frequency $\tilde{\Omega}$. Effective radii of $\rho_{\mathrm{i}} = 0.8$ and $\rho_{\mathrm{o}} = 1.166$, interaction strength of $\gamma_{\mathrm{i/o}} = 100$. Detuning varies with frequency as $\delta = (1/8)\tilde{\Omega}^2(\rho_{\mathrm{o}}^2 - \rho_{\mathrm{i}}^2)$.

4.4 Variational model

We have analyzed an analytic model of the double ring system, which uses an approximate ansatz that allows for only one angular momentum mode to be occupied in each ring [36]. It provides a fast calculation of the angular momentum of the ground states, and also offers an estimate of the critical frequency above which states with more than one angular momentum mode are expected to be ground states.

Using the general ansatz which allows contributions from all angular momentum modes, the energy functional is found to be:

$$\begin{aligned} E &= \sum_m |\alpha^{\mathrm{i}}_m|^2 \left(-\delta + \frac{m_{\mathrm{i}}^2}{\rho_{\mathrm{i}}^2} - m_{\mathrm{i}}\tilde{\Omega}\right) + \frac{\gamma_{\mathrm{i}}}{2}\left(\sum_{m,n,n'} \alpha^{\mathrm{i}^*}_m \alpha^{\mathrm{i}^*}_{n'} \alpha^{\mathrm{i}}_{n'+m-n} \alpha^{\mathrm{i}}_n\right) \\ &+ \sum_m |\alpha^{\mathrm{o}}_m|^2 \left(\delta + \frac{m_{\mathrm{o}}^2}{\rho_{\mathrm{o}}^2} - m_{\mathrm{o}}\tilde{\Omega}\right) + \frac{\gamma_{\mathrm{o}}}{2}\left(\sum_{m,n,n'} \alpha^{\mathrm{o}^*}_m \alpha^{\mathrm{o}^*}_{n'} \alpha^{\mathrm{o}}_{n'+m-n} \alpha^{\mathrm{o}}_n\right) \\ &- \kappa \sum_m \left(\alpha^{\mathrm{i}^*}_m \alpha^{\mathrm{o}}_m + \alpha^{\mathrm{o}^*}_m \alpha^{\mathrm{i}}_m\right) \quad . \end{aligned} \tag{4.15}$$

With the variational ansatz $\alpha_{\mathrm{i}} = ae^{i\phi_{\mathrm{i}}}\delta_{mm_{\mathrm{i}}}$ and $\alpha_{\mathrm{o}} = be^{i\phi_{\mathrm{o}}}\delta_{mm_{\mathrm{o}}}$, where a and b are the amplitudes of the inner and outer ring wavefunctions contributing to the double ring wavefunction, the energy functional reduces to:

$$\begin{aligned} \tilde{E} &= a^2\left(-\delta + \frac{m_{\mathrm{i}}^2}{\rho_{\mathrm{i}}^2} - m_{\mathrm{i}}\tilde{\Omega}\right) + b^2\left(\delta + \frac{m_{\mathrm{o}}^2}{\rho_{\mathrm{o}}^2} - m_{\mathrm{o}}\tilde{\Omega}\right) \\ &+ \frac{\gamma_{\mathrm{i}}}{2}a^4 + \frac{\gamma_{\mathrm{o}}}{2}b^4 - \kappa 2ab\cos(\phi_o - \phi_i)\delta_{m_{\mathrm{i}},m_{\mathrm{o}}} \end{aligned} \tag{4.16}$$

where ϕ_{i} and ϕ_{o} are the absolute phases in each of the rings, and κ is a positive number which only contributes to the energy if the m modes in each ring are the same.

In this model equal densities and equal interaction strengths in both rings are assumed ($a = b$, $\gamma_{\mathrm{i}} = \gamma_{\mathrm{o}} = \gamma$). The non-linear terms then contribute a constant energy shift independent of frequency and coupling. This could be neglected but we retain it for comparison with the energies obtained using the numerical method.

Within the variational ansatz there are two possible solutions. Firstly, the m modes in both rings can be the same. In this case the energy is minimised when the phase in each ring is the same:

$$\tilde{E}_{m_{\mathrm{i}}=m_{\mathrm{o}}} = \frac{m^2}{2}\left(\frac{1}{\rho_{\mathrm{i}}^2} + \frac{1}{\rho_{\mathrm{o}}^2}\right) - m\tilde{\Omega} + \frac{\gamma}{4} - \kappa \quad . \tag{4.17}$$

In the second case where the m modes in each ring are different, the energy is:

$$\tilde{E}_{m_{\mathrm{i}}\neq m_{\mathrm{o}}} = \frac{1}{2}\left(\frac{m_{\mathrm{i}}^2}{\rho_{\mathrm{i}}^2} + \frac{m_{\mathrm{o}}^2}{\rho_{\mathrm{o}}^2}\right) - \frac{1}{2}(m_{\mathrm{i}} + m_{\mathrm{o}})\tilde{\Omega} + \frac{\gamma}{4} \quad . \tag{4.18}$$

The ground state at a given frequency and tunnel coupling can then be determined by comparing the energies calculated with a range of m, m_{i} and m_{o}. These energy expressions highlight the competing effects of the rotation and tunnel coupling in determining the ground state structure in the double ring system. We see that there

are two ways to minimise the energy: either through the kinetic energy term (as in equation (4.18)) or through the tunnel coupling term (as in equation (4.17)), and these two possibilities correspond to very different angular momentum distributions.

Neglecting the restriction of m to integer values and minimising equation (4.17) with respect to m yields:

$$m = \frac{\tilde{\Omega}}{\frac{1}{\rho_{\mathrm{i}}^2} + \frac{1}{\rho_{\mathrm{o}}^2}} \quad . \tag{4.19}$$

Similarly, we can find the m_{i} and m_{o} that minimise equation (4.18).

$$m_{\mathrm{i}} = \frac{1}{2}\rho_{\mathrm{i}}^2\tilde{\Omega} \tag{4.20}$$

$$m_{\mathrm{o}} = \frac{1}{2}\rho_{\mathrm{o}}^2\tilde{\Omega} \tag{4.21}$$

These expressions can be reinserted into equations (4.17) and (4.18). By equating the resulting energy equations an expression for a critical frequency can then be derived.

$$\tilde{\Omega}_{\mathrm{cr}} \approx \sqrt{\frac{8\kappa\left(\rho_{\mathrm{o}}^2 + \rho_{\mathrm{i}}^2\right)}{\left(\rho_{\mathrm{o}}^2 - \rho_{\mathrm{i}}^2\right)^2}} \tag{4.22}$$

This frequency is an approximate domain boundary between ground state solutions with different expectation values of angular momentum in each ring and those with the same expectation value of angular momentum in both rings.

The variational model provides an easy way to adjust the confining double-ring potential so that the densities in each ring remain relatively even at all frequencies. For this to occur, the detuning must offset the energy difference between the m dependent terms, i.e. we want to set the detuning such that:

$$-\delta + \frac{m_{\mathrm{i}}^2}{\rho_{\mathrm{i}}^2} - m_{\mathrm{i}}\tilde{\Omega} = \delta + \frac{m_{\mathrm{o}}^2}{\rho_{\mathrm{o}}^2} - m_{\mathrm{o}}\tilde{\Omega} \quad . \tag{4.23}$$

To avoid having to use a detuning which depends on the unknown m values of the ground state, we use equations (4.20) and (4.21), again neglecting the integer-valued requirement for m. Substituting into equation (4.23) we find that the detuning should be:

$$\delta = \frac{1}{8}\tilde{\Omega}^2(\rho_{\mathrm{o}}^2 - \rho_{\mathrm{i}}^2) \quad . \tag{4.24}$$

This detuning is used in the numerical method outlined in Section 4.1.

4.5 Comparison with variational model

The energies calculated by the variational model are close to those from the numerical method. Fig. 4.9 plots the energy of these ground states calculated using the numerical method, and Fig. 4.10 plots the difference between the energies calculated numerically, and the energies calculated analytically from the variational approach. This difference is very small except for the region along the boundary between the states with different angular momentum in each ring and states with the same angular momentum in each ring. This is to be expected, as this is the area where the variational model becomes inexact.

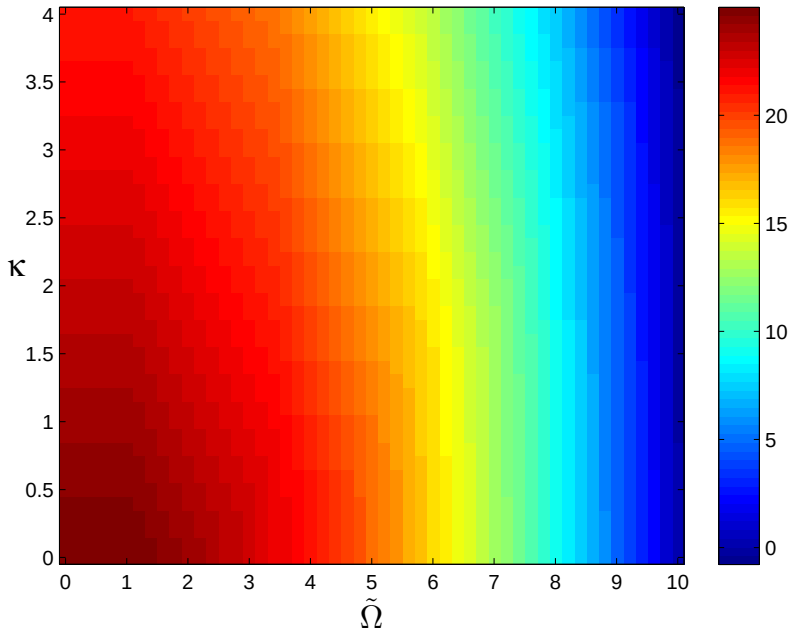

Figure 4.9: Ground state energies calculated using numerical method, as a function of tunnel coupling, κ, and scaled rotational frequency $\tilde{\Omega}$, in units of ε_{T}. Effective radii are $\rho_{\mathrm{i}} = 0.8$, $\rho_{\mathrm{o}} = 1.166$, interaction strength $\gamma_{\mathrm{i/o}} = 100$.

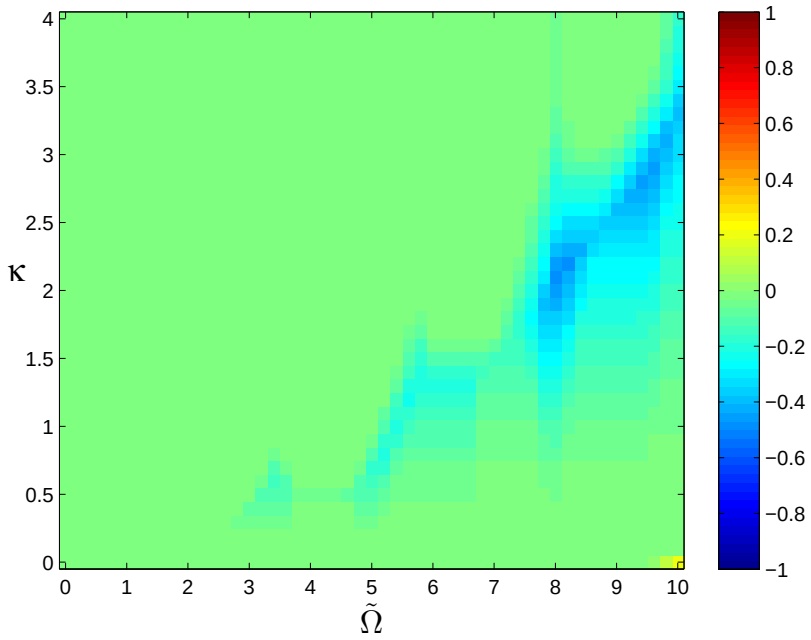

Figure 4.10: Difference in ground state energies between numerical and variational results (numerical - variational), as a function of tunnel coupling, κ, and scaled rotational frequency $\tilde{\Omega}$. Energy is in units of ε_{T}. Effective radii are $\rho_{\mathrm{i}} = 0.8$, $\rho_{\mathrm{o}} = 1.166$, interaction strength $\gamma_{\mathrm{i/o}} = 100$.

We then compare the angular momentum of the ground states calculated by the two methods. Fig. 4.12 and 4.13 plot the difference in expectation value between atoms in the outer ring and atoms in the inner ring. Shown in these plots by the pink line is the estimate of the critical frequency given by equation (4.22). In the variational model this critical frequency does not match exactly, but this is probably due to assuming continuous m throughout the derivation of $\tilde{\Omega}_{\mathrm{cr}}$.

The main difference between the variational and numerical phase plots is that in the numerical method, ground state solutions with different angular momentum in each ring are found at larger couplings than the variational model predicts. These differences are easily explained by remembering the approximations made in the variational model. Fig. 4.5 displayed the general nature of these ground states in which many angular momentum modes are occupied. Referring back to equation (4.15), we see that in the full energy functional this results in a decrease in energy through the tunnel coupling term due to the occupation of angular momentum modes in both rings. Also neglected in the variational model are interactions between the different m modes within a single ring, which tend to increase the energy of the state. The existence of these solutions at higher tunnel coupling suggests that the increase in energy due to interactions is not hugely significant. Due to neglecting the tunnel coupling terms, the variational model overestimates the energy of all states where $m_{\mathrm{i}} \neq m_{\mathrm{o}}$ and therefore sometimes incorrectly determines that states with equal m in both rings will be the ground states.

The variational model becomes more inadequate as the tunnel coupling increases. Fig. 4.11 shows the occupations of the angular momentum modes for the ground state solution at a tunnel coupling of 3.7 and a scaled frequency of 9.6. It is clear that trying to describe this solution with an ansatz where only one angular momentum mode is occupied in each ring is a bad approximation.

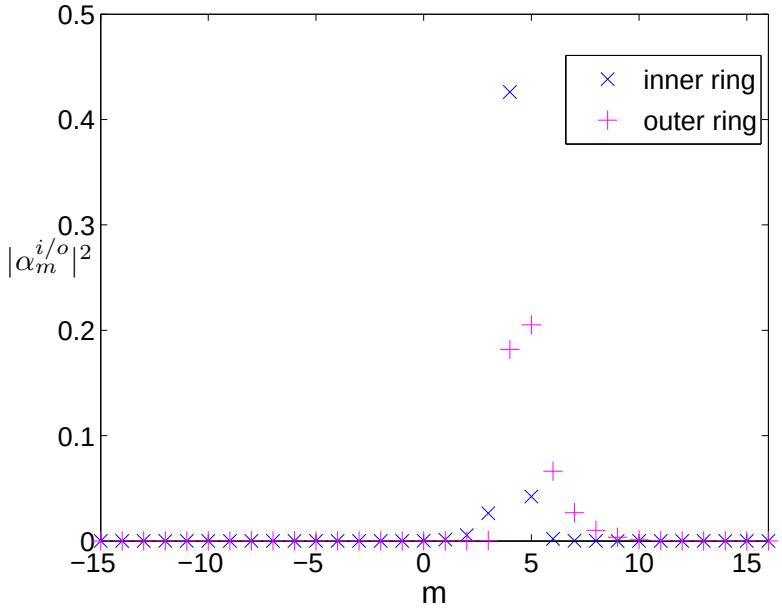

Figure 4.11: Angular momentum components of ground state at $\tilde{\Omega} = 9.6$, $\kappa = 3.7$. Effective radii are $\rho_{\mathrm{i}} = 0.8$, $\rho_{\mathrm{o}} = 1.166$, interaction strength $\gamma_{\mathrm{i/o}} = 100$.

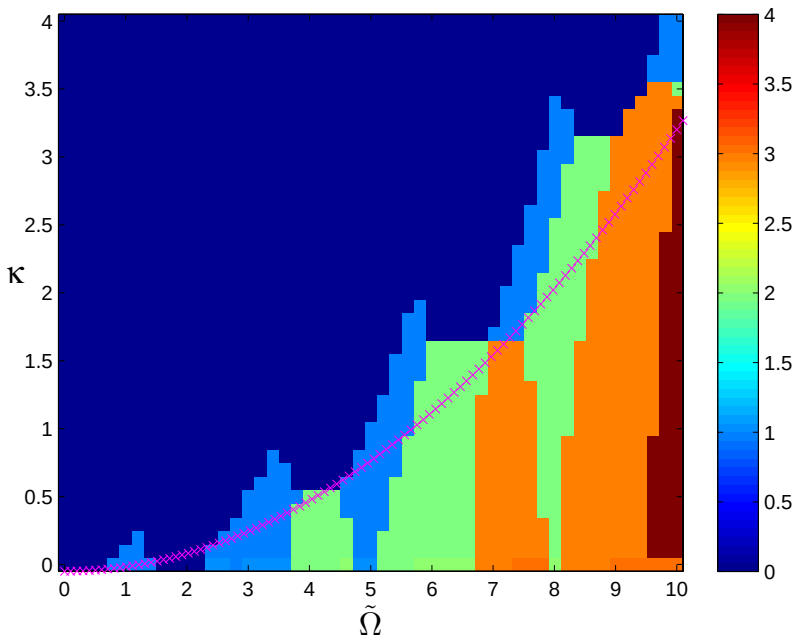

Figure 4.12: Difference in expectation value between atoms in outer and inner rings, from numerical ground state solutions, as a function of tunnel coupling, κ, and scaled rotational frequency $\tilde{\Omega}$. Effective radii are $\rho_{\mathrm{i}} = 0.8$, $\rho_{\mathrm{o}} = 1.166$, interaction strength $\gamma_{\mathrm{i/o}} = 100$.

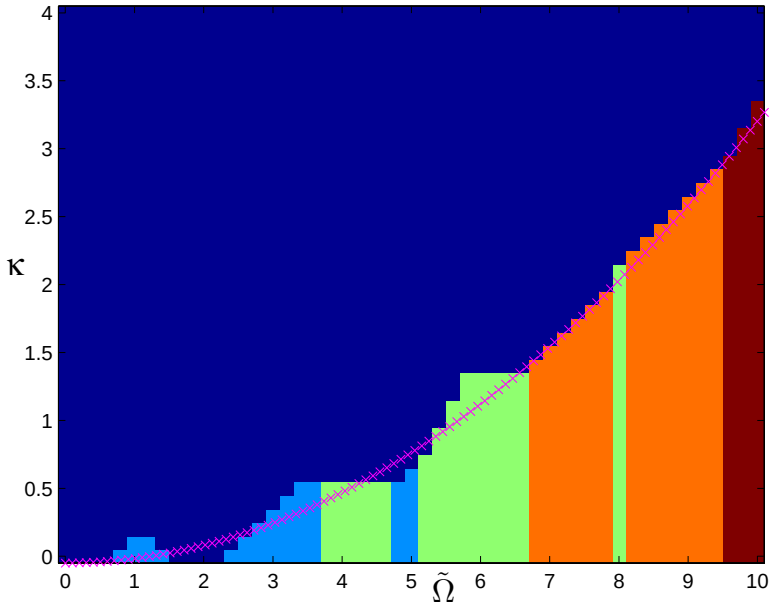

Figure 4.13: Difference in expecation value between atoms in outer and inner rings calculated from variational model, as a function of tunnel coupling, κ, and scaled rotational frequency $\tilde{\Omega}$. Effective radii are $\rho_{\mathrm{i}} = 0.8$, $\rho_{\mathrm{o}} = 1.166$, interaction strength $\gamma_{\mathrm{i/o}} = 100$.

The variational model predicts boundaries at a single frequency for all values of the tunnel coupling between solutions that have differences in the expectation value of angular momentum between the rings. This is also explained by the discarding of tunnel coupling terms in the variational calculations, which means that the critical frequencies then have no dependence on the tunnel coupling. The numerical method, however, does take into account these effects, thus producing diagonally shaped domain walls between some of the solutions where the m values are different in each of the rings.

In both the variational and numerical results, there exist some boundaries between areas with an angular momentum difference between the rings, and areas with no difference in angular momentum between the rings. Some of these boundaries are horizontal and others are diagonal. For example, in Fig. 4.12 the domains representing solutions with a single integer difference in angular momentum between the rings are triangular or diagonally shaped, whereas domains with a two integer difference are bounded by a line of constant tunnel coupling. The varying shape of these domain walls can be understood within the variational model by considering the frequency dependence of the energies of these states. The energy of states where the expectation value of angular momentum in both rings is 2 (the '22' state), and states with an expectation value of 1 in the inner ring and 3 in the outer ring (the '13' state) have the same frequency dependence in the variational model. In addition, the '13' state does not change energy as a function of the tunnel coupling. This means that the transition between the two states will occur at a constant tunnel coupling value. The same is true of the boundary between the '24' and '33' areas.

The triangularly shaped domain walls lie between states that have different frequency dependencies. For example, there is a boundary between the '24' and '22' states. The mixed state decreases in energy faster than the '22' state as a function of frequency, so a larger tunnel coupling is required before the '22' state becomes the ground state. The small triangular area at a frequency of approximately 1 can be understood similarly since it is the boundary between the '01' and '00' states, and also the boundary between the '01' and '11' states.

4.6 Influence of non-linear interactions

We find that the presence of non-linear interactions is vital for the existence of Josephson vortices in the ground states of a condensate in our double-ring system. For the non-interacting case, there exists an exact solution which predicts ground states in which only one angular momentum mode is occupied [37]. The system of equations given in (4.11), without the non-linear term, can be written as a block-diagonal Hamiltonian. Each m mode has a 2×2 entry which acts on the 2 component spinor $(\alpha_m^{(\mathrm{i})}, \alpha_m^{(\mathrm{o})})$. The 2×2 Hamiltonian for each mode is given by:

$$\mathcal{H}_m = \left(\frac{m^2}{2\bar{\rho}^2} - \tilde{\Omega}m\right)(\mathbb{1})_{2\times2} + \left(\frac{m^2 d}{2\bar{\rho}^2} - \delta\right)\hat{\tau}_z - \kappa\hat{\tau}_x \tag{4.25}$$

where

$$\hat{\tau}_z = \begin{pmatrix} 1 & 0 \\ 0 & -1 \end{pmatrix} \tag{4.26}$$

and

$$\hat{\tau}_x = \begin{pmatrix} 0 & 1 \\ 1 & 0 \end{pmatrix} \quad . \tag{4.27}$$

We have defined $d = (\rho_o^2 - \rho_i^2)/(\rho_o^2 + \rho_i^2)$, and $\bar{\rho} = \rho_o\rho_o/\sqrt{\rho_o^2 + \rho_i^2}$. The 2×2 matrix for each m mode can be diagonalized separately. The eigenvalues are found to be:

$$E_{m,\pm} = \frac{m^2}{2\bar{\rho}^2} - \tilde{\Omega}m \pm \kappa\sqrt{1 + \Upsilon_m^2} \quad , \tag{4.28}$$

where

$$\Upsilon_m = \frac{m^2 d - 2\bar{\rho}^2\delta}{2\bar{\rho}^2\kappa} \quad . \tag{4.29}$$

$E_{m,\pm}$ are the energies of the two lowest energy states where all atoms carry m quanta of angular momentum. The ground state of the condensate at a particular coupling and frequency can be found by a comparison of the lowest energies obtained from each m value.

The wave function amplitudes in the inner and outer ring can also be calculated. These are a function of Υ_m of the ground state and are thus determined by the m value of the ground state, and also the effective ring radii, tunnel coupling, and detuning. The wave function amplitudes in each ring are given by:

$$\alpha_{m,\pm}^{(\mathrm{i})} = \mp\frac{\sqrt{\sqrt{1 + \Upsilon^2} \pm \Upsilon}}{\sqrt{2}(1 + \Upsilon^2)^{1/4}} \tag{4.30}$$

$$\alpha_{m,\pm}^{(\mathrm{o})} = \frac{\sqrt{\sqrt{1 + \Upsilon^2} \mp \Upsilon}}{\sqrt{2}(1 + \Upsilon^2)^{1/4}} \quad . \tag{4.31}$$

4.6.1 Ground state results of non-interacting condensate

Since all the parameters in equations (4.28) and (4.29) are known, we can calculate the ground states analytically, and determine their energy, angular momentum, and density distribution between the two rings. Since this analytical solution is exact we expect an exact agreement between these analytic results and those obtained using the numerical method detailed in Section 4.1. The numerical method is significantly more time consuming, but provides a check of the MATLAB code which generates the analytic results. Figure 4.14 shows the energies of the ground states obtained using the analytic expressions described above. The energies calculated using the numerical method agree very well (to within 3 d.p.).

Using the analytic expressions, the ground state is always a state where all the atoms in the condensate carry the same quanta of angular momentum. Fig. 4.15 shows the angular momentum of the ground states as a function of tunnel coupling and frequency. The numerical results produce the same angular momentum phase plot. By looking at the occupation of different angular momentum modes from the numerical results we can confirm that when the condensate is non-interacting the ground states are such that the atoms in each ring have the same expectation value of angular momentum, or that when there is a difference in expectation value between the rings the condensate is almost entirely localised in only one ring. Thus the ground states of the non-interacting condensate do not contain Josephson vortices.

The effect of using a detuning that varies with frequency can be investigated in this non-interacting case. For a ground state solution with a reasonably symmetric distribution of density between the two rings, the parameter Υ_m must be small (this is the only difference between the two expressions for the individual ring amplitudes in the symmetric case). By requiring Υ_m to be less than 1, we can estimate that at frequencies less than $\sqrt{(2\kappa/\bar{\rho}^2 d^3)}$ ground state solutions will have an even spread of density between the rings. In calculating this we first replace m with $\bar{\rho}^2\tilde{\Omega}$, which is the value of m that minimizes the lowest eigenenergy from (4.28) (ignoring the integer value requirment on m).

Fig. 4.16 plots the condensate density in the inner ring of the ground states discussed above, and also plots this estimated critical frequency.

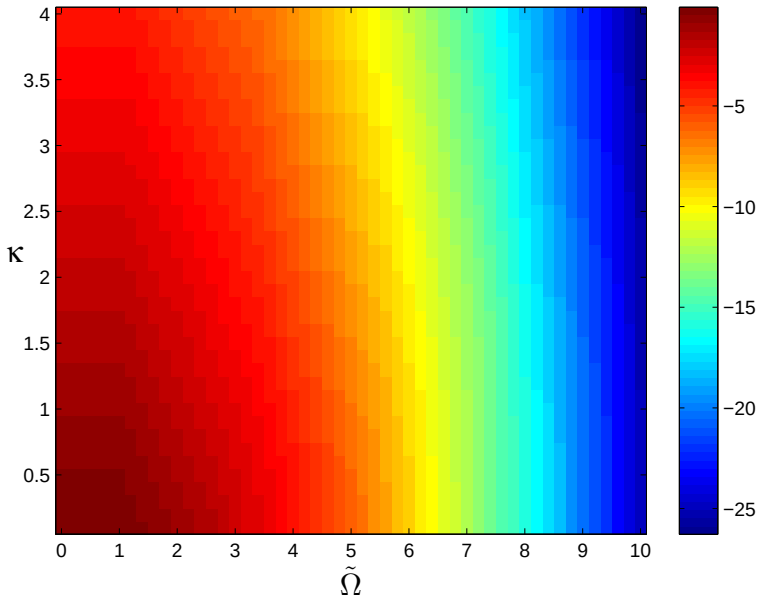

Figure 4.14: Energy of ground states of non-interacting condensate from analytic solutions (see equations (4.28) and (4.29)), in units of ε_{T}, as a function of tunnel coupling, κ, and scaled rotational frequency, $\tilde{\Omega}$. Effective radii are $\rho_{\mathrm{i}} = 0.8$, $\rho_{\mathrm{o}} = 1.166$. Detuning varies with frequency as $\delta = (1/8)\tilde{\Omega}^2(\rho_{\mathrm{o}}^2 - \rho_{\mathrm{i}}^2)$.

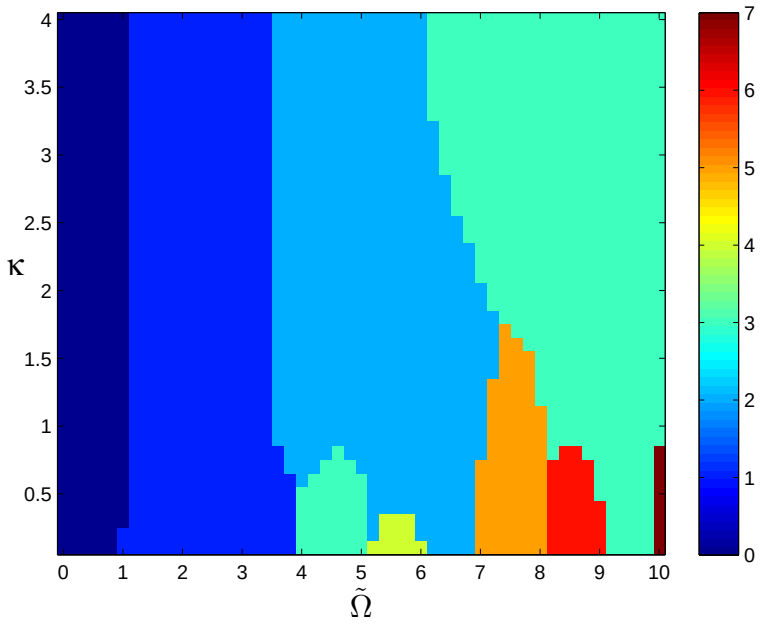

Figure 4.15: Angular momentum of double-ring ground states of non-interacting condensate from analytic calculations, as a function of tunnel coupling, κ, and scaled rotational frequency $\tilde{\Omega}$. Effective radii are $\rho_{\mathrm{i}} = 0.8$, $\rho_{\mathrm{o}} = 1.166$. Detuning varies with frequency as $\delta = (1/8)\tilde{\Omega}^2(\rho_{\mathrm{o}}^2 - \rho_{\mathrm{i}}^2)$.

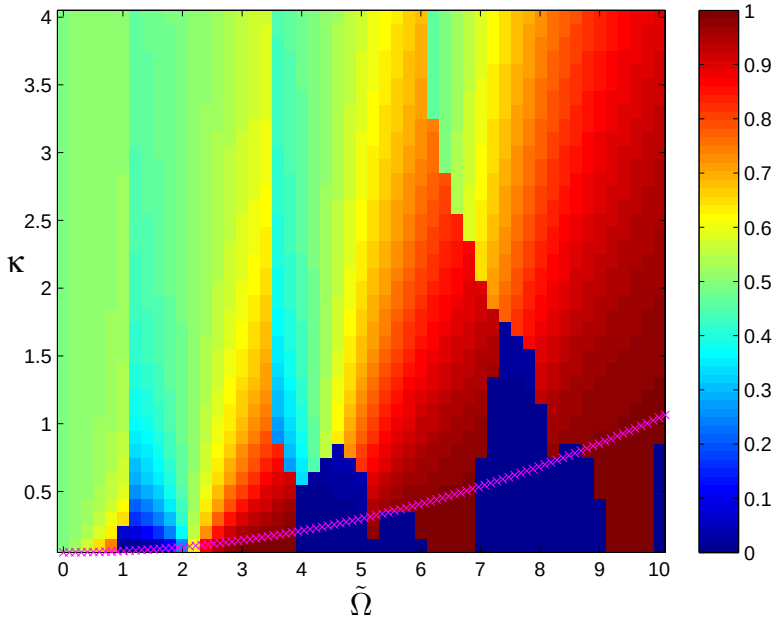

Figure 4.16: Condensate density in inner ring, as a function of tunnel coupling, κ, and scaled rotational frequency $\tilde{\Omega}$ for ground states with zero non-linear interactions. Effective radii are $\rho_{\mathrm{i}} = 0.8$, $\rho_{\mathrm{o}} = 1.166$. Detuning varies with frequency as $\delta = (1/8)\tilde{\Omega}^2(\rho_{\mathrm{o}}^2 - \rho_{\mathrm{i}}^2)$.

There is an interesting variation in density (and angular momentum of the ground state) at low tunnel coupling for the solutions with a finite detuning. The areas where the density is almost entirely localized in the outer ring (dark blue areas on Fig. 4.16) have an expectation value of angular momentum which is the same as the angular momentum of the condensate confined in the outer ring only. Similarly, the areas where the density is almost entirely in the inner ring (red areas) have an angular momentum the same as the case where the condensate is confined only in the inner ring. These solutions at low tunnel coupling are therefore still being minimized through the kinetic energy term, as were the solutions at low tunnel coupling with non-linear interactions. The density distribution plays no role in determining the ground state in the non-interacting case. Rather, the variation of the angular momentum of the ground states as a function of frequency is due to the introduction of a frequency dependent detuning which causes the energies of each m state to no longer be linear functions of frequency.

To highlight the effect of this detuning, we also calculate the ground state solutions for the case of $\delta = 0$. In this case, the critical frequency is $\sqrt{(2\kappa/\bar{\rho}^2 d)}$ which is lower than when the detuning has a frequency dependence. Fig. 4.17 plots the density in the inner ring for the ground states calculated with zero detuning. It is immediately clear that the frequency dependent detuning is important in evening out the densities between the rings. Fig. 4.18 plots the expectation value of angular momentum of the ground state solutions for the case of $\delta = 0$. The domain walls are nearly vertical, suggesting very little dependence on the tunnel coupling. This is explained by considering the density distribution, where for frequencies above ≈ 3 nearly all the condensate density lies in the outer ring, so that the ground states are similar to the case of the entire condensate being confined in the outer ring only.

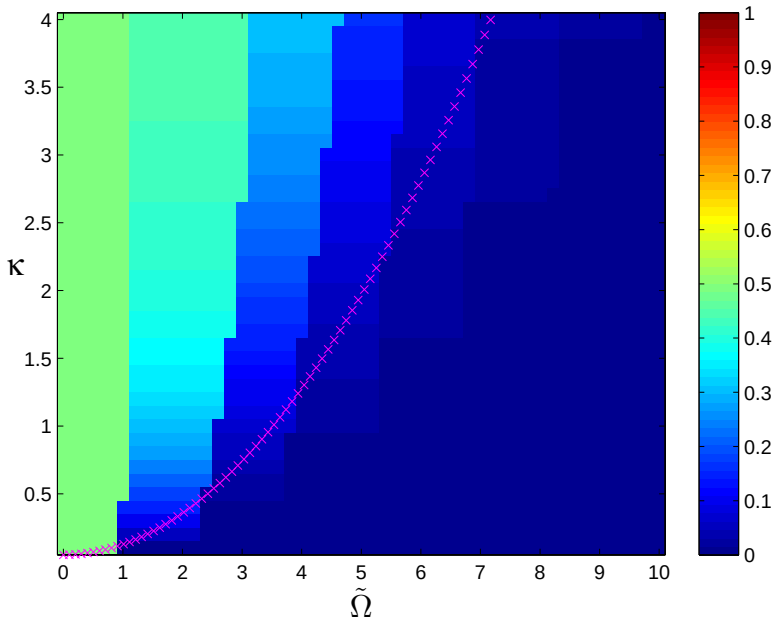

Figure 4.17: Condensate density in inner ring, $\delta = 0$, as a function of tunnel coupling, κ, and scaled rotational frequency $\tilde{\Omega}$ for ground states with zero non-linear interactions. Effective radii are $\rho_{\mathrm{i}} = 0.8$, $\rho_{\mathrm{o}} = 1.166$. Detuning is $\delta = 0$ for all frequencies. A noticeable transfer of density to the outer ring occurs as the frequency increases.

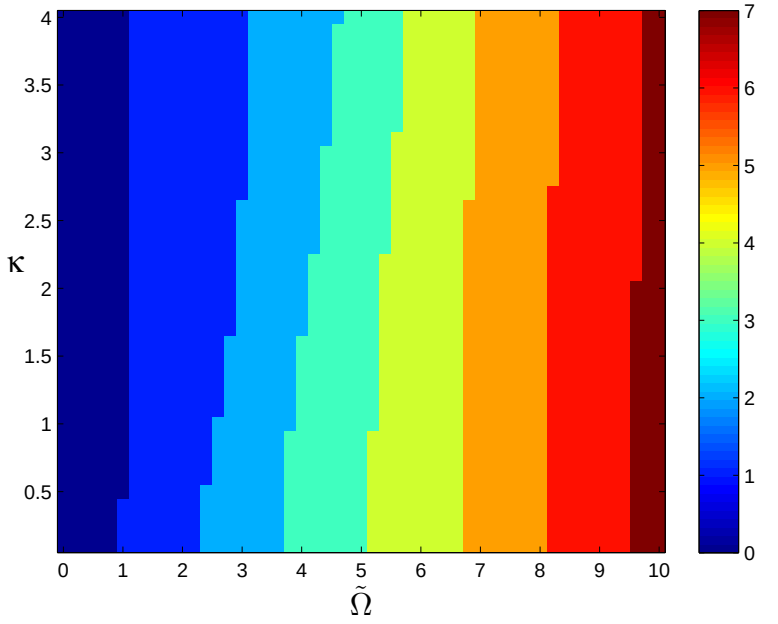

Figure 4.18: Expectation value of angular momentum of ground state solutions of non-interacting condensate, $\delta = 0$, as a function of tunnel coupling, κ, and scaled rotational frequency $\tilde{\Omega}$. Effective radii are $\rho_{\mathrm{i}} = 0.8$, $\rho_{\mathrm{o}} = 1.166$. Detuning is $\delta = 0$ for all frequencies.

4.7 Josephson vortices

4.7.1 Numerical study of ground state density and phase

Returning to the ground state solutions of a condensate with a finite interaction strength, we look at the density and phase structure of these solutions. Of particular interest are the solutions that have a difference in expectation value of angular momentum between the inner and outer rings. These are states that contain Josephson vortices. Fig. 4.19 plots the density and relative phase (the phase in the outer ring less the phase in the inner ring) as a function of the polar coordinate for a ground state solution where the expectation value in angular momentum between atoms in each ring differs by approximately 1. This ground state contains a 2π step in the relative phase and a density defect at the same position as the phase step around the angular coordinate θ. This phase step is deemed to indicate a Josephson vortex, which is a circulating current of atoms generating one quantum of angular momentum per atom. These vortices were named after their similarity to the Josephson vortices already known to exist in superconducting Josephson junctions (see also section 4.7.2).

All ground state solutions in which the difference in expectation value of angular momentum between the rings is approximately 1 share the same density and relative phase structure. However, there is a slight variation in the density and phase structure of Josephson vortices within each domain of Fig. 4.12. Ground states at a larger tunnel coupling contain deeper density defects in both rings, and a sharper phase step.

Solutions with no difference in expectation value between the two rings have a uniform relative phase and uniform densities in both rings around the coordinate θ.

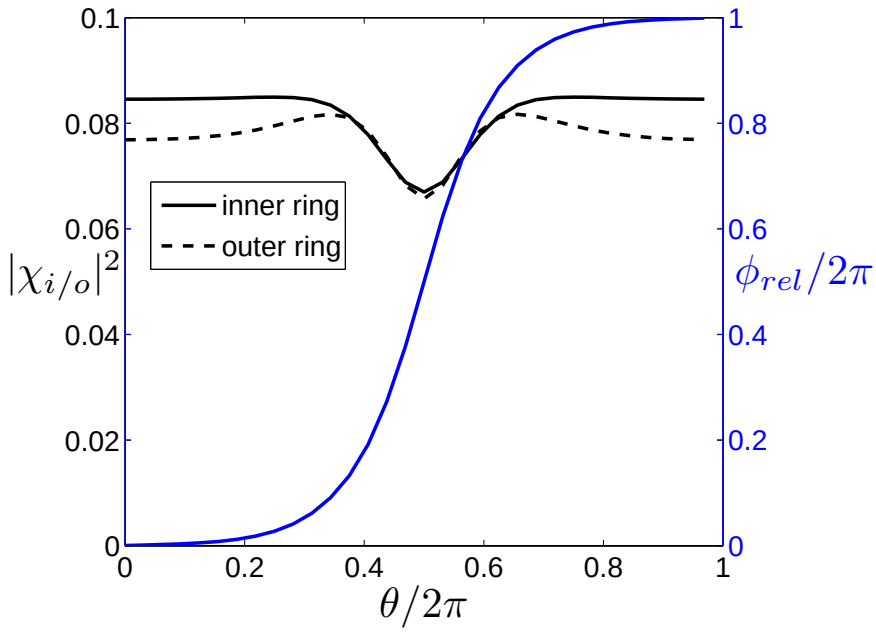

Figure 4.19: Condensate density in each ring (black lines), and normalised relative phase (blue line) for ground state at $\tilde{\Omega} = 5.8$, $\kappa = 1.9$, $\rho_{\rm i} = 0.8$, $\rho_{\rm o} = 1.166$, $\gamma = 30$. Expectation value of angular momentum in inner ring is ≈ 2, and in outer ring ≈ 3.

The influence of the tunnel coupling becomes clear after considering the structure of the ground state at zero coupling. The density in both rings is uniform around the ring, and the relative phase contains no step feature but rather varies linearly around the coordinate θ. When the tunnel coupling is finite, distorting the relative phase can further minimise the energy of a state after allowing each ring to occupy its preferred angular momentum mode and creates the Josephson vortex structure.

Ground state solutions which contain multiple Josephson vortices can also occur. In Fig. 4.12, areas of the phase plot that are coloured green, orange and red represent solutions containing two, three and four Josephson vortices respectively. Fig. 4.20 shows the density and phase profile of a ground state solution with $\langle L_z \rangle_\mathrm{i} \approx 3$ and $\langle L_z \rangle_\mathrm{o} \approx 6$. There are three Josephson vortices, which are evenly spaced around the ring and each are identical in density and relative phase structure.

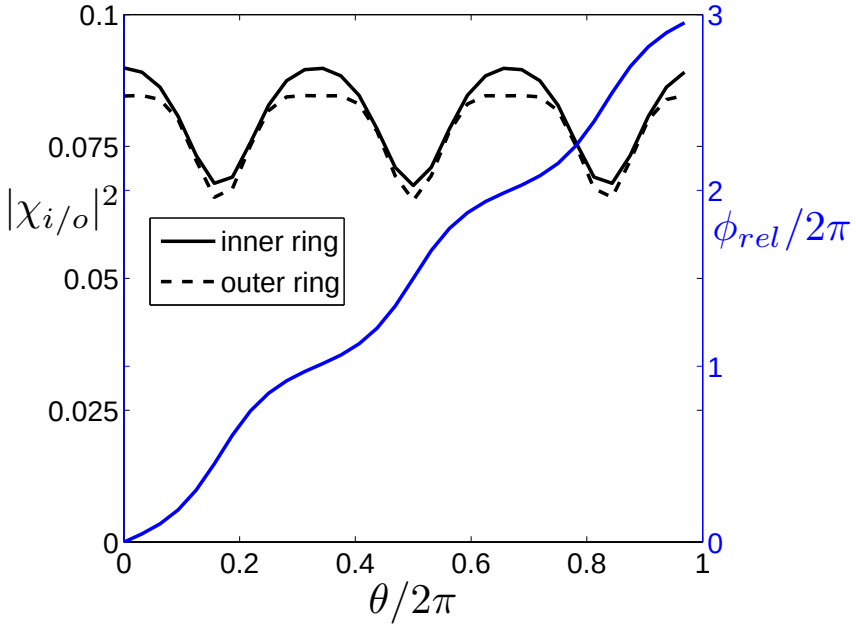

Figure 4.20: Condensate density in each ring (black lines), and normalised relative phase (blue line) for ground state at $\tilde{\Omega} = 9.6$, $\kappa = 3.1$, $\rho_\mathrm{i} = 0.8$, $\rho_\mathrm{o} = 1.166$, $\gamma = 30$. Expectation value of angular momentum in inner ring is ≈ 3, and in outer ring ≈ 6. Three Josephson vortices are present, each with a 2π phase step.

4.7.2 Josephson vortices in superconducting Josephson junctions in an applied magnetic field

Here we provide some background information on Josephson vortices in superconducting Josephson junctions. Superconducting Josephson junctions exist between two pieces of superconductor separated by a thin layer of insulating material. The insulating barrier is thin enough that Cooper pairs of electrons can tunnel from one side to the other. The tunnel coupling here establishes a relative phase between the two macroscopic wave functions that describe the condensate of Cooper pairs in each piece of superconductor. The Josephson effect described in Section 1.3.2 was first described [25, 26] and observed in these superconducting junctions. The analogous equations are:

$$J = \frac{-2K}{\hbar}\sqrt{\rho_L \rho_R}\sin\varphi \tag{4.32}$$

$$\frac{\partial\varphi}{\partial t} = \frac{2eV}{\hbar} \tag{4.33}$$

where V is the voltage applied across the junction, and J is the current flowing between the superconductors. $\rho_{L/R}$ are the Cooper pair densities in the left and right superconductors, K is the coupling constant, and φ the relative phase. For a constant applied voltage, the time-varying relative phase generates an alternating current across the junction. The Josephson oscillations in a superconducting Josephson junction are oscillations of the current, and in the double well BEC system are oscillations of the population difference between the two wells. The initial population difference in the double well system is analogous to the voltage applied to the superconducting Josephson junction.

By considering the form of the Hamiltonians in each case, a similarity can be seen between the rotation of a double-ring BEC around the z-axis and the application of a magnetic field to a superconducting Josephson junction. The kinetic and rotational terms of the Hamiltonian of a BEC in the rotating frame are:

$$H_{BEC} = \frac{\vec{p}^2}{2m} - \Omega\,(\vec{r}\times\vec{p})\cdot\vec{z} \tag{4.34}$$

where $\vec{p}$ is the momentum and Ω the rotational frequency. Rearranging the second term we can write this as:

$$H_{BEC} = \frac{\vec{p}^2}{2m} - \vec{p}\cdot(\Omega\vec{z}\times\vec{r}) \quad . \tag{4.35}$$

The kinetic energy term from the Hamiltonian of a charged particle in a magnetic field is given by:

$$H_{mag} = \frac{\left(\vec{p} - q\vec{A}\right)^2}{2m} \tag{4.36}$$

where $\vec{p}$ is again the momentum of the particle, $\vec{A}$ is the magnetic vector potential and q is the charge of the particle. This can be expanded to:

$$H_{mag} = \frac{\vec{p}^2}{2m} - \vec{p}\cdot\frac{q}{m}\vec{A} + \frac{q^2\vec{A}^2}{2m} \quad . \tag{4.37}$$

Substituting in the expression for the magnetic vector potential as a function of the magnetic field strength we find:

$$H_{mag} = \frac{\vec{p}^2}{2m} - \vec{p} \cdot \left(\frac{q}{2m} \vec{B} \times \vec{r} \right) + \frac{q^2 (\vec{B} \times \vec{r})^2}{8m} \tag{4.38}$$

Considering the first two terms of each Hamiltonian, we notice that the rotation around the z-axis, $\Omega \vec{z}$, and the uniform applied magnetic field $\vec{B}$ each enter the Hamiltonian in exactly the same way.

In a long superconducting Josephson junction (i.e. where the barrier between the two superconductors extends over a relatively large distance) the spatial coordinate along the barrier can become important. In a uniform applied magnetic field, the superconducting density and relative phase can vary along this coordinate. If the magnetic field is strong enough it can penetrate the junction in quantized units of magnetic flux, sometimes referred to as 'fluxons' [38]. Each unit of magnetic flux is generated by a circulating supercurrent of electrons. For each unit of magnetic flux that enters the junction, the relative phase along the junction contains a 2π soliton. It is this phase soliton that allows the circulating current to flow. These structures are also called Josephson vortices and are analogous to the Josephson vortices in our double-ring Bose-Einstein condensate. In both systems a Josephson vortex is identified by a 2π phase soliton. This allows a circulating current of atoms to flow in the condensate system, which generates one quantum of angular momentum per atom in the vortex. The density profile along the barrier in the superconducting Josephson junction differs in that the vortex core is filled with normal metal, whereas in the condensate system there is actually a region of suppressed total density at the position of the Josephson vortex.

Chapter 5

Dynamics of Josephson Vortices

Josephson vortices can be actuated by a sudden change in the trapping potential. This movement is then a rotation around the polar coordinate θ at a constant velocity. Initial numerical results on the dependence of the velocity on the ground state tunnel coupling and interaction strength are presented. We then present an analytic theory of Josephson vortices in our double-ring condensate in terms of the relative phase between the inner and outer rings. This includes stationary solutions for the relative phase of a single Josephson vortex, and an equation governing the dynamics of a Josephson vortex in response to an applied detuning. This theory predicts the dependence of the velocity on the tunnel coupling, which is consistent with the numerical results.

5.1 Josephson vortices can move

Josephson vortices, which exist in the double-ring ground states at small tunnel couplings, can be made to rotate around the double-ring if the detuning is suddenly altered. This change in detuning would correspond to a sudden change in the confining potential which alters the individual ring bound state energies. The movement is such that the relative phase and density structure of the Josephson vortex remain the same, except that both of these move along the polar coordinate θ at a constant velocity.

Fig. 5.1 shows the density in both rings at a fixed value of the polar coordinate, θ, as a function of the time from the applied change in detuning, where all other parameters are kept the same as in the ground state. The ground state chosen contained one Josephson vortex, and the oscillation in density in both rings over time clearly indicates the movement of the Josephson vortex past the chosen point along θ.

Fig. 5.2 plots the times of each successive rotation of the Josephson vortex, for different values of the applied detuning. We see no acceleration of the Josephson vortex in response to the change in detuning, rather, a fixed detuning seems to correspond to a constant velocity. A decrease in detuning gives rise to rotation at the same speed but in the opposite direction.

Since no acceleration takes place, the relationship between applied detuning and Josephson vortex velocity can be studied. Fig. 5.3 shows the velocity of the Josephson vortex rotation as a function of the applied change in detuning. We have taken

movement of the Josephson vortex to the right (along increasing θ) as positive velocity, and movement to the left as negative. For large changes in detuning (greater than 2), the density and phase structures become very irregular, and determining the position of the Josephson vortex becomes increasingly difficult. For small changes in detuning, there appears to be a linear relationship between velocity and detuning. Energy and angular momentum are well conserved as the Josephson vortex rotates.

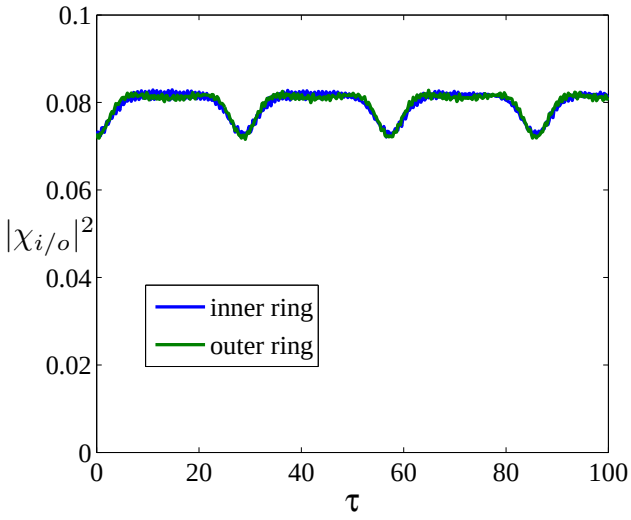

Figure 5.1: Density at fixed point along θ, after a change in detuning (δ) of +0.2, as a function of scaled time, τ. Initial wave function was the ground state at $\tilde{\Omega} = 3.4$, $\kappa = 0.8$, $\rho_{\mathrm{i}} = 0.8$, $\rho_{\mathrm{o}} = 1.166$, $\gamma = 30$, $\delta_{\mathrm{ground}} = -1.0398$, which contains one Josephson vortex. This changing density shows a rotation of the Josephson vortex around the polar coordinate θ.

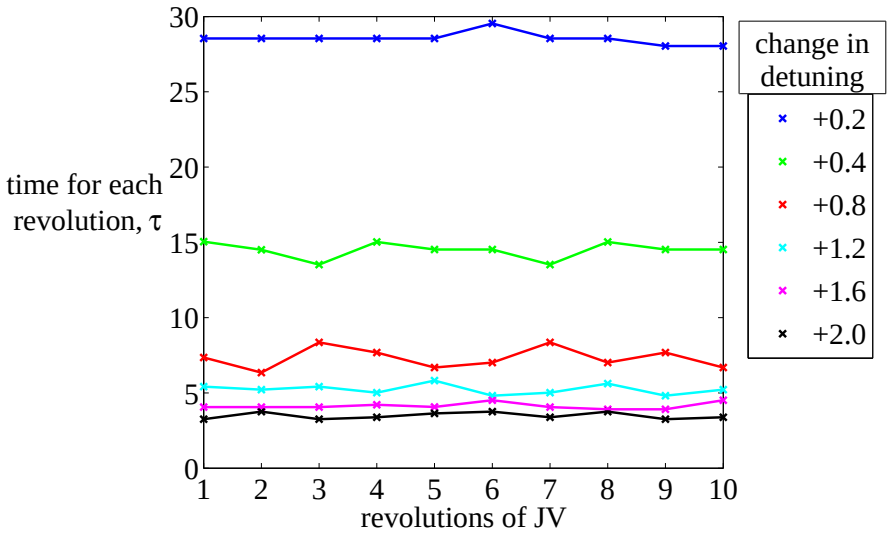

Figure 5.2: Times for rotation of the Josephson vortex in ground state at $\tilde{\Omega} = 3.4$, $\kappa = 0.8$, $\rho_{\mathrm{i}} = 0.8$, $\rho_{\mathrm{o}} = 1.166$, $\gamma = 30$, $\delta_{\mathrm{ground}} = -1.0398$, for different values of the sudden change in detuning (δ) . There is no acceleration of the Josephson vortex.

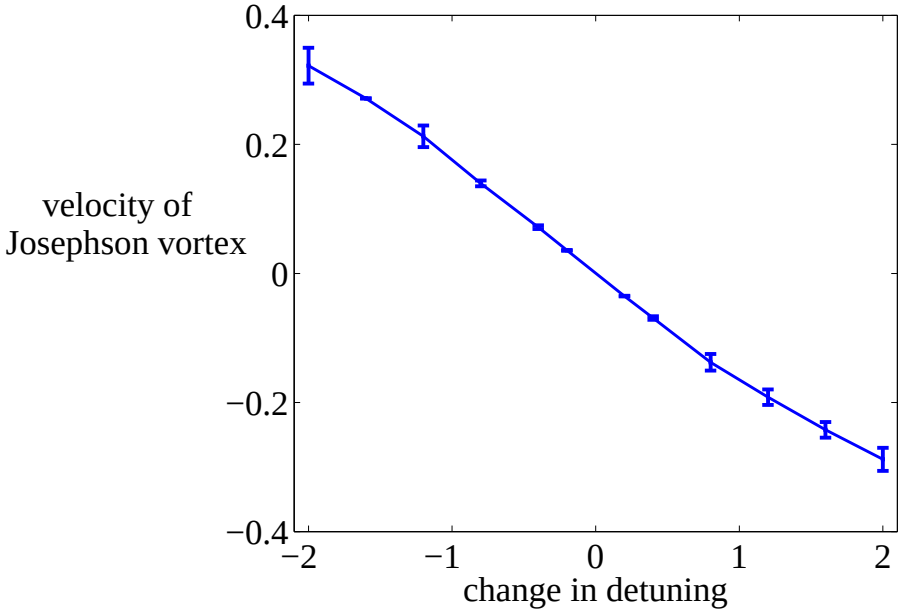

Figure 5.3: Velocity in response to a sudden change in detuning (δ), for Josephson vortex in ground state at $\tilde{\Omega} = 3.4$, $\kappa = 0.8$, $\rho_{\mathrm{i}} = 0.8$, $\rho_{\mathrm{o}} = 1.166$, $\gamma = 30$, $\delta_{\mathrm{ground}} = -1.0398$. Velocity calculated as inverse of average time for full revolution. Error bars are $\pm$ one standard deviation, where times for the first 10 revolutions were used.

5.2 Numerical study of Josephson vortex velocity

We wish to investigate the effect of certain parameters on the Josephson vortex velocity, in particular the ground state tunnel coupling and interaction strength. To first look at the influence of the tunnel coupling, we take ground state solutions containing one Josephson vortex and calculate the velocity after a change in detuning of $+0.4$. We use solutions at two different frequencies, but over a range of different tunnel couplings. The change in detuning lies within the linear region of the velocity vs. change in detuning relationship, where there is little irregularity in the density and phase structures so that the velocity can be determined fairly easily. Fig. 5.4 and Fig. 5.5 plot the log of the velocity against the log of the ground state tunnel coupling, for the Josephson vortex at two different frequencies. Shown also in these plots is the linear fit between the log of the velocity and the log of the ground state tunnel coupling, for coupling values greater than 0.57 (the reason for this will be explained in Section 5.3). In this region, the velocity is proportional to $\kappa^{-0.56}$. In Fig. 5.6 this velocity relationship is plotted as a function of κ, and is a good match to the numerical data at large coupling, but deviates noticeably from the numerical velocities at small coupling.

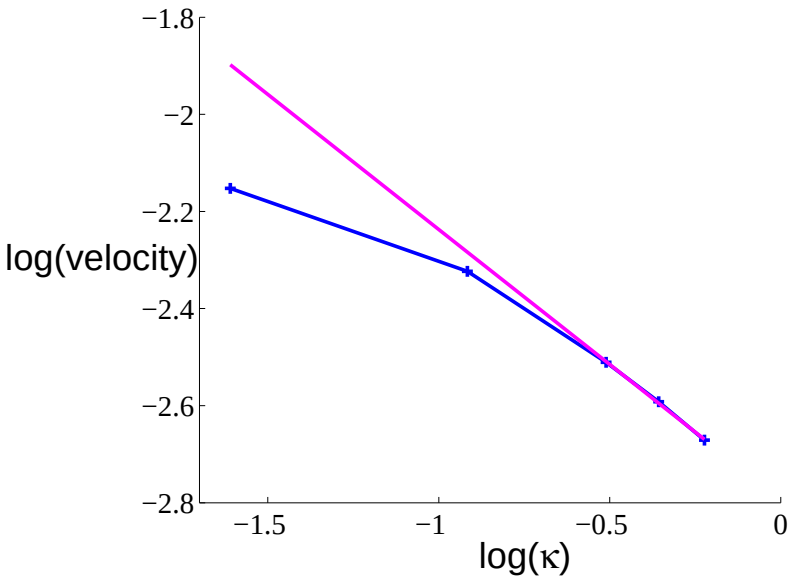

Figure 5.4: Velocity of Josephson vortex (in ground state at $\tilde{\Omega} = 3.4$, $\rho_{\mathrm{i}} = 0.8$, $\rho_{\mathrm{o}} = 1.166$, $\gamma = 30$, a '12' state) as a function of ground state tunnel coupling. Numerical data (blue line). For $\kappa \geq 0.6$: Correlation coefficient between log(velocity) and log(κ) is -0.9995, p-value is 0.0210. Linear fit from MATLAB's 'stepwisefit' function (pink line) is $\log(\text{velocity}) = -0.5564 \times \log(\kappa) - 2.7935$, with root mean squared error of 0.0037.

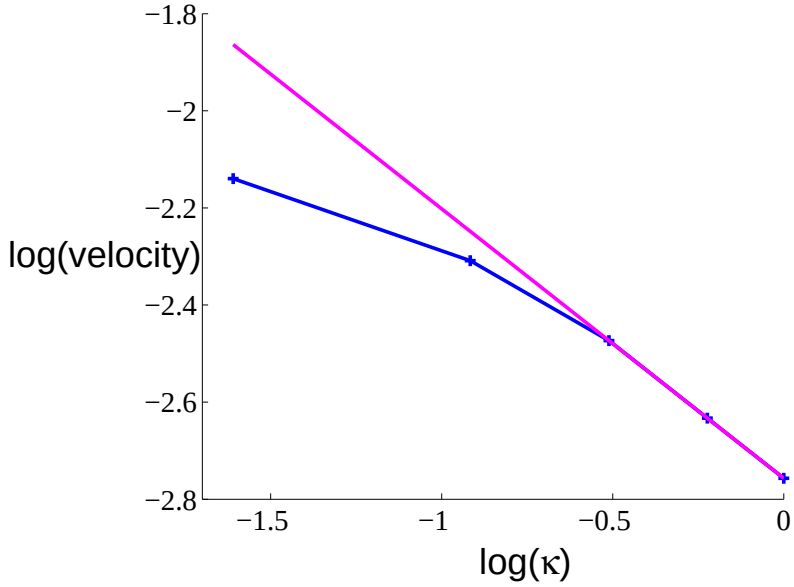

Figure 5.5: Velocity of Josephson vortex (in ground state at $\tilde{\Omega} = 5$, $\rho_{\mathrm{i}} = 0.8$, $\rho_{\mathrm{o}} = 1.166$, $\gamma = 30$, a '23' state) as a function of ground state tunnel coupling. Numerical data (blue line). For $\kappa \geq 0.6$: Correlation coefficient between log(velocity) and log(κ) is -1.0000, p-value is 6.8×10^{-4}. Linear fit from MATLAB's 'stepwisefit' function (pink line) is $\log(\text{velocity}) = -0.5551 \times \log(\kappa) - 2.7569$, with root mean squared error of 2.1×10^{-4}.

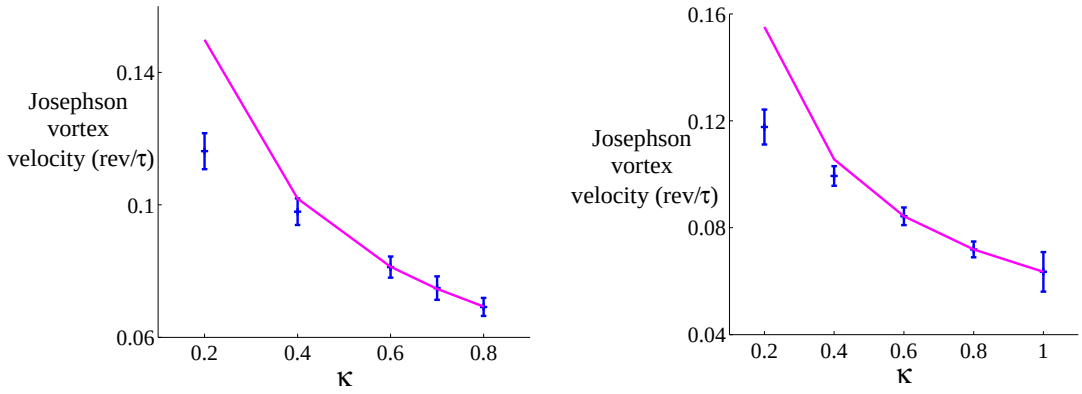

Figure 5.6: Velocity (absolute value) of Josephson vortex in ground states at $\tilde{\Omega} = 3.4$, $\rho_{\mathrm{i}} = 0.8$, $\rho_{\mathrm{o}} = 1.166$, $\gamma = 30$ (left plot), and $\tilde{\Omega} = 5$, $\rho_{\mathrm{i}} = 0.8$, $\rho_{\mathrm{o}} = 1.166$, $\gamma = 30$ (right plot) after a sudden change in detuning of $+0.4$. κ is ground state tunnel coupling. Numerical results (blue line) with error bars of $\pm$ one standard deviation calculated from velocities of first ten revolutions, and best fit relationship (pink line) where velocity depends on tunnel coupling by approximately $1/\kappa^{0.56}$.

To look at the dependence of the Josephson vortex velocity on the interaction strength of the ground state, we solve for the ground state at a range of interaction strengths (from 10 to 100) at a fixed frequency and tunnel coupling. At all of these interaction strengths the ground state contains one Josephson vortex. A change in detuning of $+0.4$ from the ground state detuning is then applied to all of the solutions. Fig. 5.7 and Fig. 5.8 show the relationship between the log of the velocity and the log of the ground state interaction strength. These two sets of results suggest that the Josephson vortex velocity depends on the ground state interaction strength by $v \propto \gamma^{0.03}$ or $v \propto \gamma^{0.05}$, which is a very weak dependence. Fig. 5.9 plots this 'best fit' relationship between velocity and interaction strength, which is in agreement with the numerical data once the uncertainties are taken into account.

These numerical results motivate the derivation of an analytical theory to describe the dynamics of a Josephson vortex, which will provide more insight into how the velocity is influenced by various parameters.

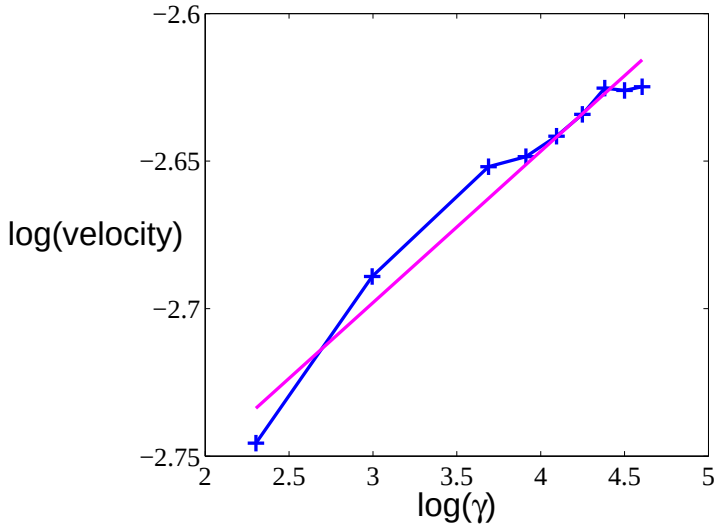

Figure 5.7: Velocity of Josephson vortex (in ground state at $\tilde{\Omega} = 3.4$, $\rho_{\mathrm{i}} = 0.8$, $\rho_{\mathrm{o}} = 1.166$, $\kappa = 0.8$, a '12' state) as a function of ground state interaction strength. Numerical data (blue line). Correlation coefficient between log(velocity) and log(γ) is 0.9742, p-value is 2.64×10^{-6}. Linear fit from MATLAB's 'stepwisefit' function (pink line) is $\log(\text{velocity}) = 0.0513 \times \log(\gamma) - 2.8519$, with root mean squared error of 0.0081.

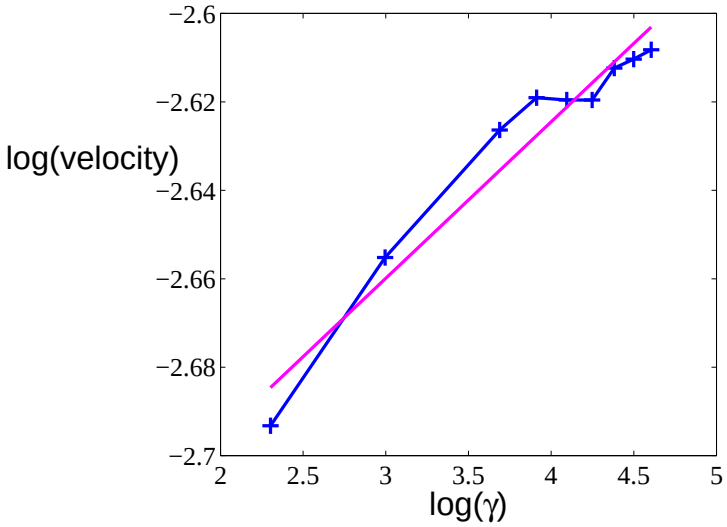

Figure 5.8: Velocity of Josephson vortex (in ground state at $\tilde{\Omega} = 5$, $\rho_{\mathrm{i}} = 0.8$, $\rho_{\mathrm{o}} = 1.166$, $\kappa = 0.8$, a '23' state) as a function of ground state interaction strength. Numerical data (blue line). Correlation coefficient between log(velocity) and log(γ) is 0.9818, p-value is 8.88×10^{-6}. Linear fit from MATLAB's 'stepwisefit' function (pink line) is $\log(\text{velocity}) = 0.0354 \times \log(\gamma) - 2.7661$, with root mean squared error of 0.0067.

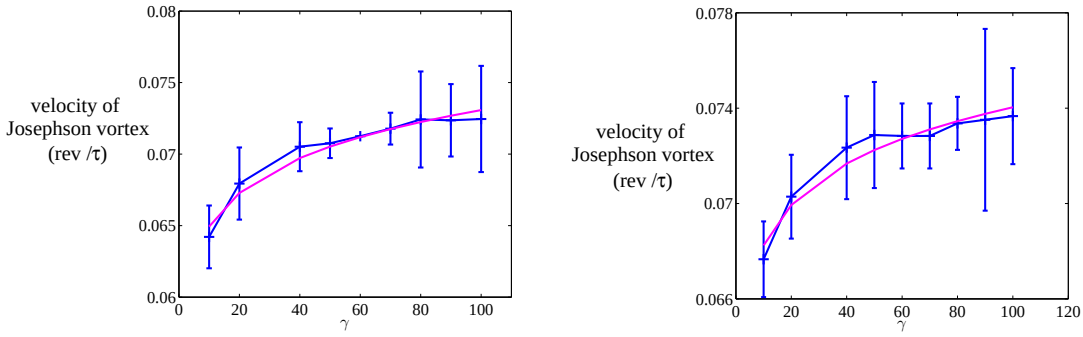

Figure 5.9: Velocity (absolute value) of Josephson vortex in '12' ground state at $\tilde{\Omega} = 3.4$, $\rho_{\rm i} = 0.8$, $\rho_{\rm o} = 1.166$, $\kappa = 0.8$ (left plot), and in '23' ground state at $\tilde{\Omega} = 5$, $\rho_{\rm i} = 0.8$, $\rho_{\rm o} = 1.166$, $\kappa = 0.8$ (right plot), after a sudden change in detuning of +0.4. γ is ground state interaction strength. Numerical results (blue line) with error bars of $\pm$ one standard deviation calculated from velocities of first ten revolutions, and best fit relationship (pink line).

5.3 Analytic theory of phase dynamics

The Hamiltonian of the double-ring system can be written in terms of density and phase variables. This allows an effective Lagrangian for the relative phase variable to be found (Ref. [37] contains full details of this derivation).

In the two-state approximation, the Hamiltonian of the double-ring system in terms of the angular part of the wave function, is $H = \int d\theta \left(\sum_\alpha \mathcal{H}_\alpha + \mathcal{H}_{\rm tun}\right)$, where:

$$\mathcal{H}_\alpha = \chi_\alpha^* \left(-\frac{\partial_\theta^2}{\rho_\alpha^2} + i\tilde{\Omega}\partial_\theta + E_\alpha + \gamma_\alpha |\chi_\alpha|^2 \right) \chi_\alpha \tag{5.1}$$

$$\mathcal{H}_{\rm tun} = -\kappa(\chi_i^* \chi_o + \chi_o^* \chi_i) \tag{5.2}$$

and α indicates the sum over the inner and outer rings. This Hamiltonian can be written in terms of density and phase variables by separating the wave function into a modulus and phase, $\chi_{i/o} = |\chi_{i/o}| e^{i\phi_{i/o}}$. We define:

$$\phi_{\rm s} = \frac{1}{2}(\phi_{\rm o} + \phi_{\rm i}) \tag{5.3}$$

$$\phi_{\rm a} = (\phi_{\rm o} - \phi_{\rm i}) \tag{5.4}$$

$$n_{\rm s} = \frac{1}{2}(|\chi_o|^2 + |\chi_i|^2) \tag{5.5}$$

$$n_{\rm a} = \frac{1}{2}(|\chi_o|^2 - |\chi_i|^2) \tag{5.6}$$

where $\phi_{\rm a}$ is the relative phase between the two rings. The effective Lagrangian for the relative phase is then [37]:

$$\mathcal{L}_{\phi_{\rm a}} = \frac{(\partial_\tau \phi_{\rm a})^2}{8\gamma} + \frac{\delta}{2\gamma}\partial_\tau \phi_{\rm a} - \frac{n_{\rm s}}{\bar{\rho}^2}\left[\frac{1}{4}\left(\partial_\theta \phi_{\rm a} - 2\bar{\rho}^2\tilde{\Omega}d\right)^2 - 2\kappa\bar{\rho}^2\cos\phi_{\rm a}\right] \tag{5.7}$$

where $d = (\rho_o^2 - \rho_i^2)/(\rho_o^2 + \rho_i^2)$, and $\bar{\rho} = \rho_o\rho_i/\sqrt{\rho_o^2 + \rho_i^2}$. From this Lagrangian, the competing effects of the tunnel coupling and the rotation can be seen. The energy from the term containing the tunnel coupling is minimised when the relative phase is zero, while the energy contribution from the third term is minimised by allowing a phase gradient when the rotation is finite. In states containing Josephson vortices both of these terms contribute to the energy, and the coupling term distorts the phase into a step structure. The equation of motion for the relative phase is:

$$\partial_\tau^2\phi_\mathrm{a} - \frac{2\gamma n_\mathrm{s}}{\bar{\rho}^2}\,\partial_\theta^2\phi_\mathrm{a} + 8\gamma\kappa n_\mathrm{s}\,\sin\phi_\mathrm{a} + 2\dot{\delta} = 0 \tag{5.8}$$

where $\dot{\delta}$ is the time derivative of the detuning. With constant or zero detuning, stationary solutions must satisfy:

$$\frac{\partial^2\phi_\mathrm{a}}{\partial\theta^2} - 4\kappa\bar{\rho}^2\sin\phi_\mathrm{a} = 0 \tag{5.9}$$

A sine-Gordon equation of the same form as (5.8) has previously appeared in Ref. [39], where a superconducting Josephson junction of similar geometry to our concentric double-ring system, and in a uniform magnetic field, has been studied. A solution for the relative phase as a function of the polar coordinate is given which describes a single Josephson vortex in the junction. By a direct comparison of the equations of motion we conclude that stationary solutions for the relative phase of a Josephson vortex in our double-ring condensate are given by:

$$\phi_\mathrm{a}(\theta) = 2\sin^{-1}\left[\mathrm{sn}\left(\frac{2\bar{\rho}\sqrt{\kappa}(\theta-\theta_0)}{k}\mid k\right)\right] + \pi \tag{5.10}$$

where θ_0 is the coordinate of the centre of the Josephson vortex. The parameter k can be determined from the condition that the relative phase must have the same value at the coordinates $\theta = 0$ and $\theta = 2\pi$. Using the fact that the Jacobi elliptic function, $\mathrm{sn}\,[u \mid k]$, has zeros when $u = n2K(k)$ [40], we find the condition:

$$2\pi\bar{\rho}\sqrt{\kappa} = kK(k) \tag{5.11}$$

where $K(k)$ is the complete elliptic integral of the first kind. Fig. 5.10 plots these solutions for two different couplings strengths, as well as phase profiles from our numerical solutions for the same value of tunnel coupling. The length scale over which the phase step is spread is $\approx 1/(2\bar{\rho}\sqrt{\kappa})$, thus solutions at larger coupling strengths have a phase step confined over a smaller region of the polar coordinate. The analytic solutions plotted in Fig. 5.10 have $\theta_0 = \pi$, so that they are centred in the same place as the numerical solutions.

To investigate the dynamics of a Josephson vortex we use the following phase profile:

$$\phi_\mathrm{a}(\theta,\tau) = 2\sin^{-1}\left[\mathrm{sn}\left(\frac{2\bar{\rho}\sqrt{\kappa}(\theta-\theta_\mathrm{JV}(\tau))}{k}|k\right)\right] + \pi \tag{5.12}$$

where $\theta_\mathrm{JV}(\tau)$ is the time-dependent position of the Josephson vortex. A Newton-like equation of motion for the position variable θ_JV can be derived by inserting the above ansatz into equation (5.8), multiplying through by $\partial_\theta\phi_\mathrm{a}$, and integrating over θ:

$$\mathcal{I}_\mathrm{JV}\,\ddot{\theta}_\mathrm{JV} = \mathcal{F}_\mathrm{JV} \quad . \tag{5.13}$$

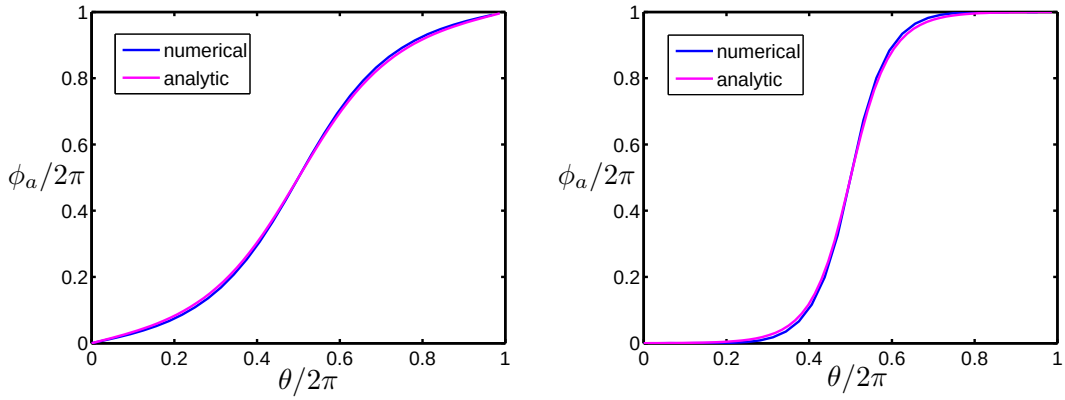

Figure 5.10: Analytic and numerical solutions of relative phase $\phi_{\rm a}$ as a function of the polar coordinate θ, for tunnel couplings of 0.6 (left hand plot), and 4 (right hand plot). Analytic solution defined in equation (5.10), with $\theta_0 = \pi$, Numerical solutions found with $\rho_{\rm i} = 0.8$, $\rho_{\rm o} = 1.166$, $\gamma = 30$, $\tilde{\Omega} = 5.2$ (left hand plot) and $\tilde{\Omega} = 10$ (right hand plot).

The moment of inertia of the Josephson vortex is given by:

$$\mathcal{I}_{\rm JV} = \frac{1}{4\pi}\int_0^{2\pi} d\theta \, \left[\partial_\theta \phi_{\rm a}^{\rm (JV)}\right]^2 \equiv \frac{2}{\pi}\,\frac{\bar{\rho}\sqrt{\kappa}}{k}\,{\rm E}\left(4\pi\,\frac{\bar{\rho}\sqrt{\kappa}}{k}\middle|\, k\right), \tag{5.14}$$

where $E(u|k)$ is the incomplete elliptic integral of the second kind [40]. To obtain the r.h.s. of Eq. (5.14), we used the relation ${\rm sn}' = {\rm cn}\,{\rm dn}$ for the derivative of a Jacobi elliptic function (see 16.16.1 in Ref. [40]), as well as the identity 17.2.10 from Ref. [40]. The torque acting on the Josephson vortex is

$$\mathcal{F}_{\rm JV} = \frac{1}{2\pi}\int_0^{2\pi} d\theta \;\; \dot{\delta}\;\partial_\theta \phi_{\rm a}^{\rm (JV)} \quad . \tag{5.15}$$

For a detuning that is not spatially dependent, this torque simplifies to $\dot{\delta}$. In this case, integration of equation (5.13) then tells us that the velocity of a Josephson vortex is directly related to the detuning, δ. This is consistent with our early numerical experiments in Section 5.1. For a detuning which does vary spatially, numerical simulations [41] show that the dynamics are considerably more complex. A possible continuation from the work of this thesis would be to investigate analytically the effect of some specific spatially varying external potentials.

Equation (5.13) does not contain γ, the interaction strength, and so the velocity of a Josephson vortex will also be independent of the interaction strength. This explains the very weak dependence seen in the numerical results, which is so small it can be neglected. The influence of the ground state coupling strength is visible in Fig. 5.11. At large couplings, the inertia is proportional to the square of the coupling. However, below $\bar{\rho}\sqrt{\kappa} \approx 0.5$ this relationship no longer holds. The velocity then, at tunnel couplings greater than approximately 0.57, is proportional to the inverse square root of the tunnel coupling. At lower values of the tunnel coupling the velocity has a weaker dependence on the coupling. This is consistent with our numerical results, which showed that for sufficiently large tunnel couplings, the velocity is proportional to $\kappa^{-0.56}$, with only three data points being used in the linear

fit. At tunnel couplings below 0.57, the deviation from the inverse square root law is obvious in Fig. 5.4 and 5.5.

Rewriting the angular velocity $\dot{\theta}$ as a tangential velocity, we see that the expression for the inertia differs from the mass expression in Ref. [39] by a factor of $1/r_{\mathrm{T}}$, where r_{T} is the mean radius of the double ring. The limits of small and large tunnel couplings correspond to the limits of small and large junction length (where the junction length is the trap circumference), since κ is the scaled tunnel coupling. Thus the behaviour of the inertia at small tunnel couplings seen in Fig. 5.11 is consistent with the divergent behaviour of the mass in Ref. [39] for small junction lengths. In the limit of long junctions, the mass in Ref. [39] becomes independent of the trap size, and this is also true of $\mathcal{I}_{JV}/r_{\mathrm{T}}$.

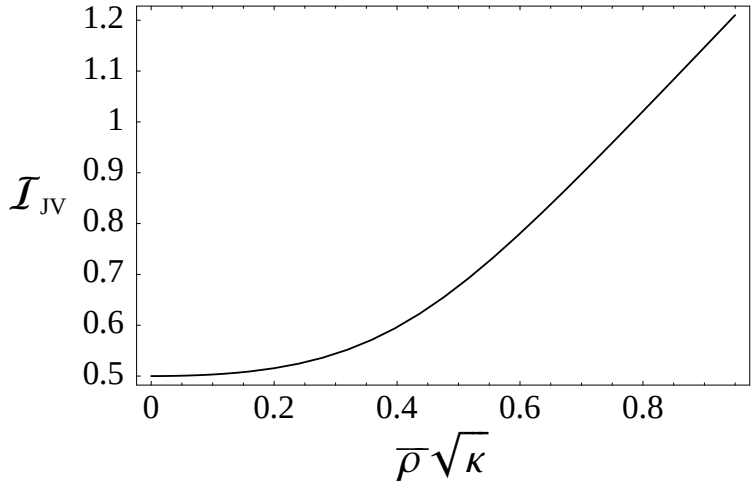

Figure 5.11: Moment of inertia for a Josephson vortex in co-planar coupled annular Bose-Einstein condensates.

Chapter 6

Conclusions

We have described an optical potential which could be used to confine a Bose-Einstein condensate in two concentric rings and allows for atoms to tunnel between the rings. A condensate in this double-ring geometry can be described by a two state model, from which we can calculate the tunnel coupling. Initial calculations using a specific double-ring potential show that coherent oscillations in the population imbalance, which are due to tunneling, may occur on a time scale of seconds, meaning that tunneling effects occurring in the double-ring trap may be observed during a condensate lifetime.

The main work of this thesis has been to determine the ground states of the condensate in a rotating double-ring trap. We investigate this in a phenomenological way, where the exact form of the trapping potential is not determined but instead we use a set of parameters which indicate the relative energies in each ring, the effective radii of the rings, the tunnel coupling, and the effective interaction strength in each ring. Due to the rotation, the atoms in the condensate will carry quantized angular momentum. The difference in the ring radii means that the kinetic energy in each individual ring will be minimised by different angular momentum. This effect is in competition with the tunnel coupling, which can minimise the energy if the angular momentum modes in each ring are the same. The angular momentum of the ground states is thus determined by a combination of the tunnel coupling and rotational effects.

At low tunnel couplings, the ground state solutions of a condensate in the double-ring contain Josephson vortices. These are identified by a 2π step in the relative phase, and a density defect in both rings at the same position around the ring as the phase step. Each Josephson vortex contributes one quantum of angular momentum per atom to the system. The Josephson vortex structures allow the expectation value in each ring to be close to the preferred angular momentum value of the isolated rings thus minimising the kinetic energy of the state. A further decrease in energy comes through the small, but finite, tunnel coupling. The tunnel coupling distorts the relative phase profile so that the phase step occurs over a confined region of the angular coordinate, and the relative phase is minimised around the rest of the ring. At larger tunnel couplings, ground states are such that all atoms in the condensate circulate with the same angular momentum.

It was found that non-linear interactions between atoms in the condensate are essential for ground state solutions to contain Josephson vortices. In an ideal condensate, ground states in the rotating double-ring at any frequency are states where

only one angular momentum mode is occupied. In this extreme, Josephson vortices are absent at all values of the tunnel coupling. The non-linearity couples multiple angular momentum modes, allowing states with many modes occupied to become the ground state. The absence of Josephson vortices in the non-interacting case is independent of the density distribution between rings. In the interacting case, however, relatively even densities are necessary in order to realize Josephson vortex states.

Josephson vortices are actuated by applying a sudden change to the detuning. The change in detuning would correspond to a sudden change in the trapping potential so that the individual ring bound state energies are shifted relative to each other. Numerical studies indicate that this sudden change gives rise to a constant velocity for the Josephson vortex. These dynamics have an analogy with long superconducting Josephson junctions, where a Josephson vortex (a 'fluxon') can be made to move along the junction barrier if a bias current is applied. An analytic theory of Josephson vortices in terms of the relative phase variable has been derived to explain these dynamics. This model includes stationary solutions for the relative phase of a single Josephson vortex. The equation of motion for the position variable of a Josephson vortex has been derived, which shows that the velocity of the vortex is directly related to the detuning. The dependence of the velocity on the ground state tunnel coupling has been investigated, and this is also consistent with the numerical results.

Also studied, though not related to the main work of this thesis, were possible dynamical instabilities of states in this double-ring system. Recent work [45] reported that the first excited state of a same radii double-ring condensate was unstable with respect to the growth of finite angular momentum modes, for some values of the tunnel coupling. Presented in Appendix C is a re-worked investigation of the instabilities in this system, which clarifies what may be several possible typographical errors in the original paper, and also points out the relationship between the sign of the tunnel coupling and the symmetry of the ground and first excited states. We find that there are instabilities in this same radii system, and in our concentric double-ring system, and the excitation spectra for these systems is similar. Numerical integration confirms the behaviour described in Ref. [45], that is, for the first excited state, at certain values of the coupling strength, there is a transfer of atoms to other angular momentum modes.

Various possibilities exist for further study of this concentric double-ring system. Within the analytic model, stationary solutions for multiple Josephson vortices could be found. Further work on the dynamics of Josephson vortices would be very interesting, especially for the case where there is a spatially varying external potential. This can also be done using the analytic model. Also, the coherent Josephson oscillations of states without Josephson vortices could be investigated. These may prove interesting given the extra dimension around the ring, which could lead to more complex dynamics than is seen in double well confinements. The possibility of macroscopic quantum tunneling of a Josephson vortex could be included. This has already been studied in the context of superconducting Josephson junctions [43]. Finite temperature effects could also be incorporated into both the numerical and analytic studies of the Josephson vortex dynamics. This would provide a damping mechanism for fluxon motion [26] and would require a treatment beyond the Gross-Pitaevskii formalism used in this thesis.

Appendix A

Methods of Determining Radial Ground State Solutions

A.1 Thomas Fermi approximation

The Thomas Fermi approximation consists of neglecting the differential term in the Gross-Pitaevskii equation, which then allows a solution for the wave function of the condensate to be found analytically. This is equivalent to assuming that the kinetic energy contribution to the overall energy of the system is negligible. This assumption is generally expected to be valid at the low temperatures where Bose-Einstein condensates exist; however, its accuracy should be tested for each specific confining geometry and particle interaction strength. The kinetic energy term is proportional to the gradient of the density, so should be valid in regions where the density varies slowly in space. It is expected to become inaccurate near the edges of the condensate, and is not expected to be a good approximation for small condensates. Neglecting the kinetic energy term, the GPE reduces to:

$$\tilde{\mu}\varphi(\rho) = \left(\tilde{U}(\rho) + \eta N|\varphi(\rho)|^2\right)\varphi(\rho) \tag{A.1}$$

This can be divided through by $\varphi(\rho)$. Rearranging then gives an expression for the density profile, where $\tilde{\mu}$, the chemical potential, is unknown:

$$|\varphi(\rho)|^2 = \frac{\tilde{\mu} - \tilde{U}(\rho)}{\eta N} \tag{A.2}$$

Examining equation (A.2) we see that the inverted double well potential defines the basic shape of the Thomas Fermi density profile, while the chemical potential $\tilde{\mu}$ fixes the height of this profile. Two constraints allow us to find the correct solution. Firstly, the wave function must be correctly normalised, and secondly, only positive densities are physical. Ignoring regions of the density profile where the density is negative (for a similar neglecting of areas of negative density see Ref. [34]), we see that increasing or decreasing the chemical potential has the effect of increasing or decreasing the normalisation of the density profile, respectively. To solve, a simple bisection method can be used with two initial values of the chemical potential (one giving a density profile normalisation with a value greater than 1, and one giving a density profile with a normalisation less than 1). This quickly solves for the chemical potential, and therefore the density profile which is normalised correctly.

To use the Thomas Fermi method to solve for the ground state of a condensate confined in only one of the rings, the potential must be taken to be zero-valued across the region where the second ring would lie. The inverted single ring potential will still provide the shape of the density profile, and the normalisation of the density profile must be calculated over the single ring only.

A.2 Numerical energy minimisation

To find the ground state wave function without employing any approximations requires a numerical method. A minimisation procedure can be used since the ground state solution is the minimum energy configuration of the system. The method below was described in Ref. [35] (and included here for completeness) except that we use a finite difference discretisation rather than the suggested finite element discretisation. The energy functional, or expectation value of the energy, is defined as:

$$E = \int \left[\left(\frac{d\varphi(\rho)}{d\rho} \right)^2 + \tilde{U}(\rho)|\varphi(\rho)|^2 + \frac{\eta N}{2}|\varphi(\rho)|^4 \right] \rho d\rho \tag{A.3}$$

and the chemical potential is then:

$$\tilde{\mu} = E + \int \frac{\eta N}{2}|\varphi(\rho)|^4 \rho d\rho \quad . \tag{A.4}$$

The energy can be minimised under the constraint that the wave function must be normalised correctly. To achieve this a new function, F, is defined which is now the function to be minimised. The normalisation condition is incorporated into F via a Lagrange multiplier, λ:

$$F = E - \lambda \left[\int |\varphi(\rho)|^2 \rho d\rho - 1 \right] \tag{A.5}$$

The energy functional can be discretised using finite difference approximations with a stepsize of h. The first derivative of the wave function with respect to ρ is given by the central difference approximation:

$$\frac{d\varphi_{\mathrm{j}}}{d\rho} = \frac{\varphi_{\mathrm{j}+1} - \varphi_{\mathrm{j}-1}}{2h} \tag{A.6}$$

where φ_{j} is the value of the wave function at step j along ρ. The terms inside the square brackets of the energy functional can then be written as follows:

$$X_{\mathrm{j}} = \left(\frac{\varphi_{\mathrm{j}+1} - \varphi_{\mathrm{j}-1}}{2h} \right)^2 + \tilde{U}(\rho_{\mathrm{j}}) \left(\varphi_{\mathrm{j}}\right)^2 + \frac{\eta N}{2} \left(\varphi_{\mathrm{j}}\right)^4 \tag{A.7}$$

where X_{j} is the bracket evaluated at the jth grid point along ρ. Using the trapezium rule for numerical integration the energy can be written as:

$$E = \frac{h}{2} \left[(X_2\rho_2 + X_{\mathrm{n}-1}\rho_{\mathrm{n}-1}) + 2\sum_{\mathrm{j}=3}^{\mathrm{n}-2} X_{\mathrm{j}}\rho_{\mathrm{j}} \right] \tag{A.8}$$

This means that our final expression for F is:

$$F = \frac{h}{2}\left[(X_2\rho_2 + X_{n-1}\rho_{n-1}) + 2\sum_{j=3}^{n-2} X_j\rho_j\right] - \lambda\left[\frac{h}{2}\left[(\varphi_1\rho_1 + \varphi_n\rho_n) + 2\sum_{j=1}^{n-1}\varphi_j\rho_j\right] - 1\right] \quad \text{(A.9)}$$

The set of $\{\vec{\varphi}_j, \lambda\}$ which minimises equation (A.9) defines a critical point of F, where the derivative with respect to each variable should vanish, i.e.:

$$\nabla_{\vec{\varphi}_j} F = \vec{0} \quad \text{(A.10)}$$

$$\frac{\partial F}{\partial \lambda} = 0 \quad \text{(A.11)}$$

Equations (A.10) and (A.11) describe a system of n+1 equations with n+1 variables (assuming there are n grid points along ρ). We use Newton's method to solve these. Newton's method can be employed to find the root of a vector function, $\vec{f}(\vec{x})$. The root, $\vec{x}$ satisfies both:

$$\vec{f}(\vec{x}) = \vec{0} \quad \text{(A.12)}$$

and:

$$J(\vec{x}) = \vec{0} \quad \text{(A.13)}$$

where $J(\vec{x})$ is the Jacobian matrix. Each iteration of the Newton method generates a new vector, $\vec{x}_{k+1}$ from the previous vector $\vec{x}_k$. This is found by solving for Δx then adding this increment on to $\vec{x}_k$:

$$J(\vec{x}_k)\Delta x = -\vec{f}(\vec{x}) \quad \text{(A.14)}$$

$$\vec{x}_{k+1} = \vec{x}_k + \Delta x \quad \text{(A.15)}$$

Applying this to our system, the vector function we wish to find the root of is:

$$\nabla_{\vec{\varphi}_j,\lambda} F = \vec{0} \quad \text{(A.16)}$$

We therefore solve (A.17) for $\Delta(\vec{\varphi}_j, \lambda)$, then we increment $(\vec{\varphi}_j, \lambda)$ by $\Delta(\vec{\varphi}_j, \lambda)$:

$$J(\vec{\varphi}_j, \lambda)\Delta(\vec{\varphi}_j, \lambda) = -\nabla_{\vec{\varphi}_j,\lambda} F \quad \text{(A.17)}$$

The initial value of the Lagrange multiplier can be obtained using a least squares method as suggested in Ref. [35]. For an initial estimate of the wave function, λ is chosen such that the sum of the squared non-zero entries of the vector $\nabla_{\vec{\varphi}_j} F$ is minimised. This value of λ can be found by taking the dot product of $\nabla_{\vec{\varphi}_j} F$, and then inserting the values of $\vec{\varphi}_j$ from the initial wave function. This gives a function of λ which is easily minimised.

Thomas Fermi wave functions were used as initial wave functions for the numerical method. Slightly lowered Thomas Fermi wave functions were used to find an appropriate step size, since Thomas Fermi wave functions always have higher peak values than those of the full solutions. It was found that a step size of $h = 0.001$ was sufficiently small to converge to the ground state solution for different initial wave functions. To solve for the ground state of the condensate confined in only one of the rings, the appropriate discretized potential must be inserted into the code, and appropriate initial wave functions chosen. The rest of the method is the same as for the double ring case.

A.2.1 Extension of numerical method for first excited state

In addition to ground states, excited states are also critical points of the energy functional. This means we can use the same minimisation method as for ground states, provided we include additional constraints regarding the symmetry of the wave function. The first excited state of the condensate in the double ring potential will be antisymmetric, and therefore must have a node (i.e. a point of zero density) at some point along ρ. Multiple first excited states were found in Ref. [35] by minimizing the energy while enforcing a node in the centre of a harmonic trap.

The two rings of potential in our system are slightly asymmetric, so we do not know exactly where the node will lie. This makes the minimisation method time consuming as we have to test multiple possible node positions. To enforce a node at a chosen point along ρ, the value of the discretised initial wave function at the node point was set to zero. In the Newton minimisation procedure, the change in wave function was then calculated such that the change at the node point was also zero at every iteration. Requiring the jth entry of Δx to be zero in equation (A.14) is effectively the same as removing this entry in Δx, and the ith column of the Jacobian matrix. This leaves an overdetermined system requiring a least squares solution. A QR Decomposition of the Jacobian matrix can be done in Mathematica, and then the change in wave function can be found using the LinearSolve function. We found that while the energy converged to a steady value, the normalisation varied for all node positions. The first excited state was then taken as the solution with a normalisation closest to 1. Also, of course, we require the first excited state energy to be higher than the ground state energy.

A.3 Testing numerical energy minimisation

To check the robustness of the method used to solve for the radial ground states, we choose an initial wave function which is not related to the mathematical description of the problem (as opposed to the Thomas Fermi wave function which took its form directly from the confining potential). Fig. A.1 shows the triangular wave function used for this purpose. From this initial condition a wave function is found which looks the same as those obtained using the Thomas Fermi wave functions as initial conditions. The solutions which used Thomas Fermi wave functions as initial conditions all had energies of -166.042 and chemical potentials of -155.177. The wave function resulting from the triangular initial wave function has the same energy and chemical potential values (to 3 d.p.), indicating that our minimisation method is accurate for the range of initial conditions used.

We also test the minimisation method against the density profiles and energy calculations presented in Ref. [44] for the case of a condensate confined in a harmonic potential. We solve the Gross-Pitaevskii equation using a potential of $\rho^2/2$ and the same normalisation as was used in Ref. [44] so that our solutions can be directly compared. In the 2-D case, this normalisation is:

$$2\pi \int |\varphi(\rho)|^2 \rho d\rho = 1 \tag{A.18}$$

For this harmonic oscillator potential a stepsize of 0.02 is sufficient since the trapping potential is noticeably shallower than our double-ring potential. Fig. A.2 shows the

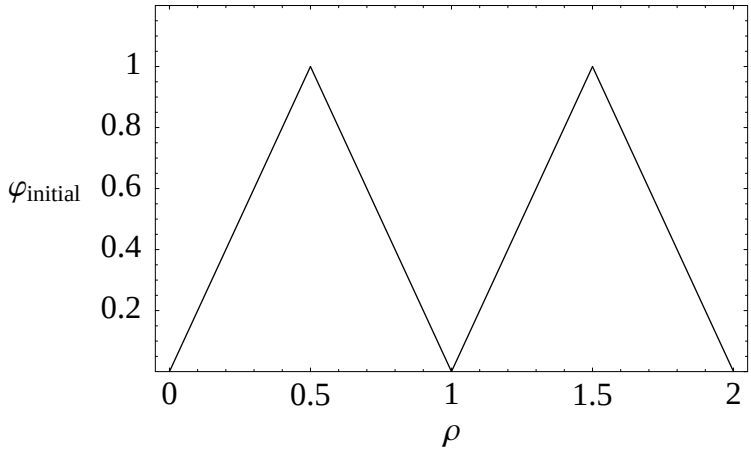

Figure A.1: An initial double-ring wave function used for testing the numerical minimisation method

non-rotating ground state wave function from Ref. [44], and from our Newton minimisation programme. The four wave functions correspond to solutions containing different numbers of atoms in the condensate. Fig. A.3 shows the singly quantized vortex state, again from Ref. [44], and the $m = 1$ vortex wave functions found using our minimisation programme.

The expression for the energy of the $m = 0$ state given in Ref. [44] is:

$$\varepsilon_0 = \sqrt{1 + 2\xi N} \tag{A.19}$$

where ξ is the healing length, which has been determined experimentally to be 1/7. Also given by Ref. [44] is an expression for the energy difference between vortex and non-vortex states, from which the energy of the $m = 1$ state can be found as:

$$\varepsilon_1 = 2\sqrt{1 + \frac{\xi N}{2}} \tag{A.20}$$

Tables A.1 and A.2 compare the energies calculated using these formulas and the corresponding energies found from our numerical method. As can be seen the agreement is reasonable and a smaller stepsize may increase the accuracy slightly. The energies of the vortex states were calculated in the laboratory frame (i.e. at zero rotational frequency). The discrepancy at higher interaction strengths is most likely due to the approximation used in Ref. [44], where a Gaussian trial wave function was used in the energy functional to obtain their analytic energy expression.

N	Analytical Energies from Ref. [44]	Calculated Numerical Energies
1	1.134	1.136
10	1.964	1.930
100	5.438	5.189
1000	16.933	15.998

Table A.1: Comparison of non-vortex ground state energies

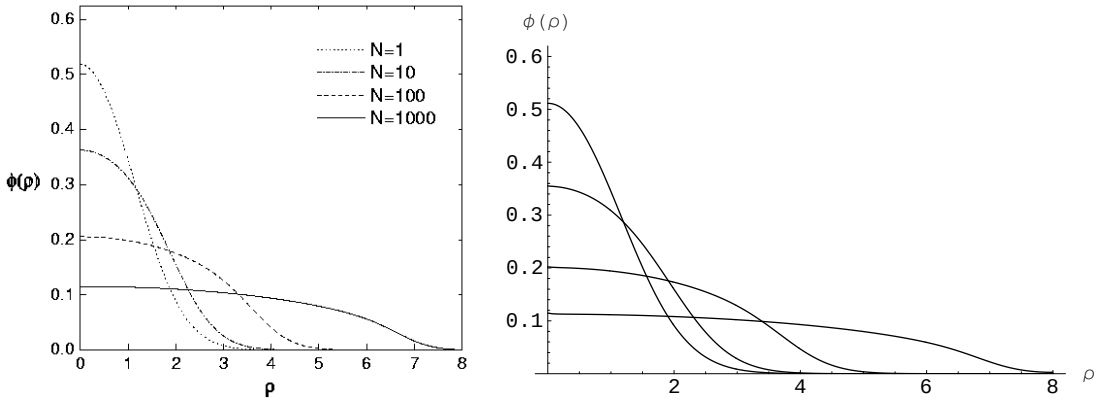

Figure A.2: $m = 0$ wave functions from [44] (left hand plot), and from our numerical minimisation (right hand plot)

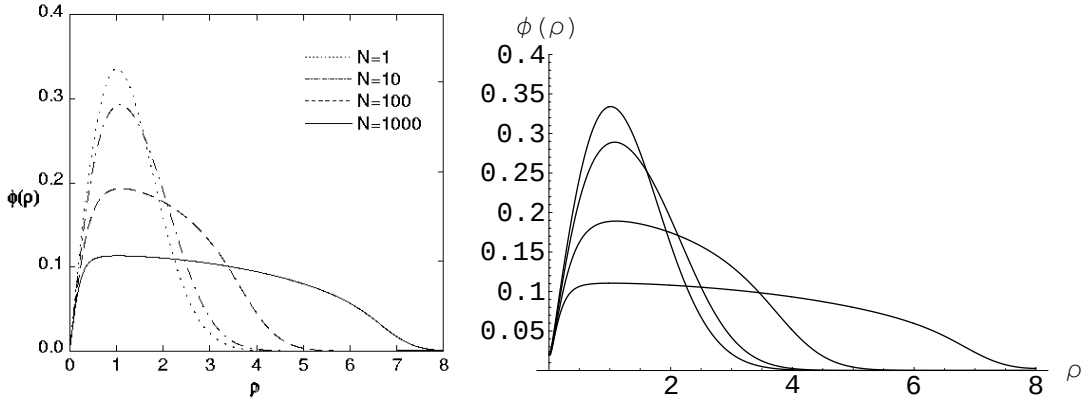

Figure A.3: Vortex solutions from [44] (left hand plot), and from our numerical minimisation (right hand plot)

N	Analytical Energies from Ref. [44]	Calculated Numerical Energies
1	2.070	2.075
10	2.619	2.613
100	5.707	5.542
1000	17.021	16.156

Table A.2: Comparison of vortex state energies

Appendix B

Imaginary Time Propagation

B.1 Notes on numerical method

The MATLAB code used for the imaginary time propagation was written by Joachim Brand, and is included on the CD that accompanies this thesis. Here we briefly include the derivation of the working equations for this method and comments about the initial conditions used and the stability of ground state results obtained.

A given initial wave function can be considered to be constructed from contributions of many eigenstates of the system. Under imaginary time propagation, the contributions from all eigenstates decay, but the ground state contribution decays most slowly. After a sufficiently long evolution time (during which the wave function must be kept normalised), the wave function consists mostly of a ground state contribution only.

The 'imaginary-time' equation is:

$$\frac{\partial \alpha_m^{\mathrm{i/o}}}{\partial t} = -\frac{\partial E}{\partial \alpha_m^{(\mathrm{i/o})^*}} + \beta \frac{\partial N}{\partial \alpha^{(\mathrm{i/o})^*}} \tag{B.1}$$

where E is the energy functional of the system. The last term has been introduced to compensate for the decay of the wave function. N is the total number of particles in the condensate.

To choose the value of β, we first consider that the time evolution of the total number of particles in the condensate is given by:

$$\frac{dN}{dt} = \sum_m^{x=\mathrm{i,o}} \alpha_m^{(x)^*} \dot{\alpha}_m^{(x)} + \dot{\alpha}_m^{(x)^*} \alpha_m^{(x)} \tag{B.2}$$

where the index m indicates a summation over all angular momentum modes, and x indicates that the summation should be carried out first using the amplitudes from the inner ring, and then using the amplitudes from the outer ring. Expressing the time derivatives of the amplitudes using the right hand side of equation (B.1) gives:

$$\frac{dN}{dt} = 2\beta N - 2Re\left(\alpha_m^{(x)} \frac{\partial E}{\partial \alpha_m^{(x)}}\right) \tag{B.3}$$

From this we see that the number of particles in the condensate will remain constant

over time if we set:

$$\beta = \frac{1}{N} Re \sum_{m}^{x=\mathrm{i/o}} \alpha_m^{(x)} \frac{\partial E}{\partial \alpha_m^{(x)}} \tag{B.4}$$

To look at the energy evolution under imaginary time propagation we consider the time derivative of the energy functional:

$$\frac{dE}{d\tau} = \sum_{m,x=\mathrm{i/o}} \left(\frac{\partial E}{\partial \alpha_m^x} \dot{\alpha}_m^x + \frac{\partial E}{\partial \alpha_m^{x^*}} \dot{\alpha}_m^{x^*} \right) \tag{B.5}$$

which can be rewritten as:

$$\frac{dE}{d\tau} = -2N \sum_{m,x=\mathrm{i/o}} \frac{1}{N} \left| \frac{\partial E}{\partial \alpha_m^x} \right|^2 + 2N\beta^2 \quad . \tag{B.6}$$

These two terms can be likened to the mean of the squares, and the square of the mean, respectively.

$$\frac{dE}{d\tau} = -2N \left(\langle H^2 \rangle - \langle H \rangle^2 \right) \leq 0 \tag{B.7}$$

Using this simple argument we can see that the energy under imaginary time propagation should decrease, since the variance $(\langle H^2 \rangle - \langle H \rangle^2)$ is a positive quantity.

The non-linear term is transformed into position space at each time step. This allows the non-linear term to be calculated as a product of the discretised wave function, rather than calculating the complicated summation over angular momentum modes. The discretised wave function in position space is given by the inverse Fourier transform of the vector of angular momentum amplitudes, so that we have the relations:

$$\vec{\chi}_{\mathrm{i/o}} = \frac{N}{\sqrt{2\pi}} ifft(\vec{\alpha}^{\mathrm{i/o}}) \tag{B.8}$$

$$\vec{\alpha}^{\mathrm{i/o}} = \frac{\sqrt{2\pi}}{N} fft(\vec{\chi}_{\mathrm{i/o}}) \tag{B.9}$$

The MATLAB code considers the evolution of angular momentum modes from $m = -15$ to 16. Modes close to these limits are not noticeably occupied in any of the ground state wave functions found. The density in position space is then known at 32 points around the polar coordinate. Including more angular momentum modes would increase the accuracy of the density profiles, although there is nothing to suggest that any more information would be gained by doing this.

The imaginary time algorithm requires a vector of initial occupations of the angular momentum modes in both rings. Provided these initial conditions are reasonably close to the ground state, they will not change noticeably but will converge to a stationary state. To find the ground state multiple initial conditions must be tested and the energies compared. The reason for this is that for a given state to change the angular momentum in one of the rings, a vortex must cross that ring. This costs interaction energy, and is therefore not likely to happen in the imaginary time evolution as this follows the path of decreasing energy.

To check the energies returned by the imaginary time propagation, we compare them with results from the variational model for solutions where the angular momentum in both rings is the same. The agreement is good.

We can check that the ground states are stationary by evolving them in real time. Their stability can also be checked by following the same procedure after adding small random noise components to each angular momentum mode. As expected, no unstable or nonstationary wave functions were found.

B.2 Choice of parameters for ground state solutions

Using the radial inner and outer ring wave functions shown in Fig. 3.2 and Fig. 3.3 we can calculate the various integrals which appear as free parameters in the general method of Section 4.1. We find:

$$\frac{1}{\rho_{\mathrm{i}}^2} = \int \frac{1}{\rho} |\phi_{\mathrm{i}}|^2 d\rho = 2.43 \tag{B.10}$$

$$\frac{1}{\rho_{\mathrm{o}}^2} = \int \frac{1}{\rho} |\phi_{\mathrm{o}}|^2 d\rho = 0.54 \tag{B.11}$$

These correspond to effective radii of $\rho_{\mathrm{i}} = 0.64$ and $\rho_{\mathrm{o}} = 1.34$. The effective interaction strengths are:

$$\gamma_{\mathrm{i}} = \frac{\eta N}{2\pi} \int |\phi_{\mathrm{i}}|^4 \rho d\rho = 9.6 \tag{B.12}$$

$$\gamma_{\mathrm{o}} = \frac{\eta N}{2\pi} \int |\phi_{\mathrm{o}}|^4 \rho d\rho = 5.6 \tag{B.13}$$

The tunnel coupling from Section 3.4.2 is ≈ 0.6. The values of these integrals can of course be changed by altering the trapping potential, but these particular values give an indication of the order of magnitude that might be accessible. For the calculation of the ground states presented in Section 4.2 we use effective radii of $\rho_{\mathrm{i}} = 0.8$ and $\rho_{\mathrm{o}} = 1.166$, and effective interaction strengths of 100 for both rings as this produces a more even density distribution than lower values of the interaction strength.

Appendix C

Instabilities in Double-Ring Bose-Einstein Condensates

Recent work by I. Lesanovsky and W. von Klitzing [45] showed that the non-rotating first excited state of a Bose-Einstein condensate in a vertically separated double-ring system is unstable with respect to the occupations of finite angular momentum modes, at some values of the coupling strength. Their time-dependent numerical simulations show the onset of Josephson oscillations in the angular momentum at these unstable coupling strengths. Their double-ring system differs from the co-planar system studied in this thesis. They consider two rings of identical radius, positioned at different heights along the z-axis, so that the coupling strength can be altered by varying the spatial separation of the rings along the z-axis. Their stability analysis involves calculating the Bogoliubov spectrum, from which modes with a complex eigenfrequency can be identified. These modes can grow in occupation if a small initial occupation is provided. We extend this analysis to investigate possibile instabilities in the co-planar double ring system.

C.1 Method for examining stability

We present the method outlined in Ref. [45] but with several corrections. Whether these are typographical errors is somewhat unclear. We find similar results from numerical integration; however, we include the derivation to clear up any confusion which may exist. In particular our derivation is consistent with the general quantum mechanical theorem that the ground state of a double well system should be symmetric, and the first excited state antisymmetric. This symmetry requirement then determines the sign of the coupling term.

A two-state model is employed to describe the equal radii double-ring system from Ref. [45], with the indices u and d identifying the 'up' and 'down' rings. A separation ansatz is used so that the radial and z-dependence of the wavefunction can be integrated out, after assuming that the condensate exists in the ground state of the confining potential along these two directions. Coupled equations for the angular parts of the wavefunction are then given by (see also equation (2) of Ref. [45]):

$$i\frac{\partial \chi_{\mathrm{u/d}}}{\partial \tau} = -\frac{\partial^2 \chi_{\mathrm{u/d}}}{\partial \phi^2} - \kappa \chi_{\mathrm{d/u}} + \gamma |\chi_{\mathrm{u/d}}|^2 \chi_{\mathrm{u/d}} \tag{C.1}$$

where κ is the tunnel coupling, which is positive. This can be compared with equation (4.5), where we have set $\rho_{\mathrm{i/o}} = 1$, and are not considering any finite detuning or rotation. We also assume equal interaction strengths in both rings. Note that in Ref. [45] the coupling term appears as $+\kappa$, where κ is also taken to be positive. This discrepancy is discussed below. The angular part of the wavefunction can be written as a superposition of contributions from all angular momentum modes, with amplitudes given by the $\alpha_m^{\mathrm{u/d}}$.

$$\chi_{\mathrm{u/d}} = \frac{1}{\sqrt{2\pi}} \sum_m \alpha_m^{\mathrm{u/d}} e^{im\theta} \tag{C.2}$$

By direct substitution we find:

$$\begin{aligned} i \textstyle\sum_m \frac{\partial \alpha_m^{\mathrm{u/d}}}{\partial \tau} e^{im\theta} = \textstyle\sum_m m^2 \alpha_m^{\mathrm{u/d}} e^{im\theta} - \kappa e^{i\theta_{\mathrm{u/d}} - \theta_{\mathrm{d/u}}} \textstyle\sum_m \alpha_m^{\mathrm{d/u}} e^{im\theta} \\ + \frac{\gamma}{2\pi} \textstyle\sum_j \sum_k \sum_l \alpha_j^{\mathrm{u/d}} \alpha_k^{\mathrm{u/d}^*} \alpha_l^{\mathrm{u/d}} e^{ij\theta} e^{-ik\theta} e^{il\theta} \end{aligned} \tag{C.3}$$

where m, j, k, l can each vary over all the positive and negative integers. To contribute, terms from the non-linear interaction term must satisfy the condition $j - k + l = m$. Using this we can rewrite the summations in this last term:

$$\begin{aligned} i \textstyle\sum_m \frac{\partial \alpha_m^{\mathrm{u/d}}}{\partial \tau} e^{im\theta} = \textstyle\sum_m m^2 \alpha_m^{\mathrm{u/d}} e^{im\theta} - \kappa e^{i\theta_{\mathrm{u/d}} - \theta_{\mathrm{d/u}}} \textstyle\sum_m \alpha_m^{\mathrm{d/u}} e^{im\theta} \\ + \frac{\gamma}{2\pi} \textstyle\sum_m \sum_k \sum_l \alpha_{m+k-l}^{\mathrm{u/d}} \alpha_k^{\mathrm{u/d}^*} \alpha_l^{\mathrm{u/d}} e^{im\theta} \end{aligned} \tag{C.4}$$

We can next write a system of $m \times 2$ equations which govern the dynamics of the entire system (see equation (4.11) for comparison with concentric double-ring system):

$$i \frac{\partial \alpha_m^{\mathrm{u/d}}}{\partial \tau} = m^2 \alpha_m^{\mathrm{u/d}} - \kappa e^{i\theta_{\mathrm{u/d}} - \theta_{\mathrm{d/u}}} \alpha_m^{\mathrm{d/u}} + \frac{\gamma}{2\pi} \sum_k \sum_l \alpha_{m+k-l}^{\mathrm{u/d}} \alpha_k^{\mathrm{u/d}^*} \alpha_l^{\mathrm{u/d}} \tag{C.5}$$

Note that here the non-linear term differs from the one given in equation (3) of Ref. [45].

To investigate the stability of the non-rotating state, solutions are found for the coupled equations where only the $m = 0$ mode is occupied. These solutions are:

$$\alpha_0^{\mathrm{u}} = \pm \alpha_0^{\mathrm{d}} e^{-i(\gamma/4\pi \mp |\kappa|)\tau} \tag{C.6}$$

where the density of atoms in each ring is equal. These solutions differ from those given in Ref. [45] in three respects. Firstly, in our solutions there is a negative in the exponential power. Without this negative sign the solutions do not satisfy the relevant $m = 0$ equations. Secondly, the chemical potential depends only on the absolute value of κ. This is always the case when the double ring eigenvalues are calculated using a two-state model (refer to Section 1.3.2).

The final difference between our $m = 0$ solutions and those in the PRL is of a more fundamental nature. The solutions given in the PRL in equation (4) are such that the state with lower energy, $\gamma/2 - \kappa$ is antisymmetric (κ is taken as positive in Ref. [45], as can be seen in Fig. 1), and the first excited state is symmetric. As explained in Section 1.3.2, the ground state of a double well system is symmetric. To satisfy this symetry requirement, κ must be a positive number, as it is defined

in Section 1.3.2. However, comparing equation (C.1) above, and equation (3) in Ref. [45], we see that the definitions of κ differ by -1. We continue the stability analysis with the correct definition of the tunnel coupling, which is consistent with a symmetric ground state solution.

The ansatz $\alpha^{\mathrm{u/d}}_{m\neq 0} = e^{-i\mu\pm\tau}\left[u^{\mathrm{u/d}}_m e^{-i\omega\tau} + v^{*\mathrm{u/d}}_m e^{i\omega\tau}\right]$, can be used to investigate the stability of the $m = 0$ mode. Substituting this ansatz into equations (C.5), and linearizing in u_m and v_m, we find equations of the form:

$$\omega u^{(\mathrm{u/d})}_{m,\pm} = (m^2 - \mu_\pm + \gamma)u^{(\mathrm{u/d})}_{m,\pm} + \frac{\gamma}{2}v^{(\mathrm{u/d})}_{-m,\pm} - \kappa u^{(\mathrm{d/u})}_{m,\pm} \tag{C.7}$$

$$-\omega v^{(\mathrm{u/d})}_{-m,\pm} = (m^2 - \mu_\pm + \gamma)v^{(\mathrm{u/d})}_{-m,\pm} + \frac{\gamma}{2}u^{(\mathrm{u/d})}_{m,\pm} - \kappa v^{(\mathrm{d/u})}_{-m,\pm} \tag{C.8}$$

where the subscript $+$ refers to the symmetric ground state, and the subscript $-$ refers to the antisymmetric first excited state. Diagonalising these equations we find that the ground and first excited states share one branch of the excitation spectra which is independent of the tunnel coupling:

$$\omega_1 = \sqrt{(m^2 + \frac{\gamma}{2})^2 - \frac{\gamma^2}{4}} \tag{C.9}$$

The second branch of the spectra has a tunnel coupling dependence, and differs for the ground and first excited states:

$$\omega_{2,\pm} = \sqrt{(m^2 + \frac{\gamma}{2} \pm 2\kappa)^2 - \frac{\gamma^2}{4}} \tag{C.10}$$

For the symmetric ground state both of these frequencies are always real and positive, implying stability of the ground state against excitations of finite angular momentum modes. For the antisymmetric state the energy $\omega_{2,-}$ can be complex for some values of the tunnel coupling. Fig. C.1 shows the imaginary and real parts of this excitation energy for an interaction parameter $\gamma = 2$. This spectrum of instabilities is similar in form to that presented in Ref. [45]; however, our derivation is consistent with the expected symmetries of the ground and first excited states.

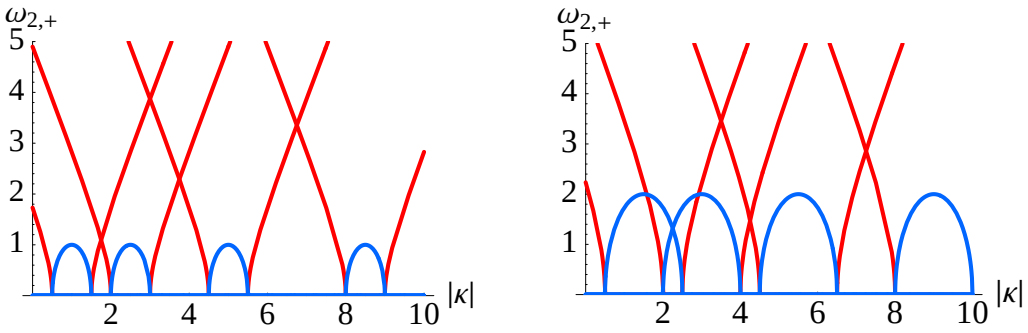

Figure C.1: Excitation energies for antisymmetric state. Red - real part, Blue - imaginary part, $\gamma = 2$ (left plot), $\gamma = 4$ (right plot)

C.1.1 Numerical integration to show instabilities

We use MATLAB to construct and then evolve ground and first excited state wave functions in time. The first excited state wave functions are expected to show a transfer of occupation from the $m = 0$ mode to finite angular momentum modes, at certain values of the tunnel coupling. The ground state wave functions are expected to show no change over time.

Initial wave functions are constructed so that the $m = 0$ mode has an occupation of $\sqrt{0.5}$ in the upper ring and $+\sqrt{0.5}$ in the lower ring for a ground state, or $-\sqrt{0.5}$ in the outer ring for a first excited state. This mode, and the first five (positive and negative) finite angular momentum modes are given a small random occupation (0.001*rand). The wave function is then renormalised before it is evolved in time.

We find similar results as shown in Ref. [45]. The first excited state of the double-ring system contains a dynamic instability at certain values of the tunnel coupling. This results in the growth of finite angular momentum modes, and oscillations in angular momentum and population between the rings. Ground state wave functions show no change over time, even with the small random occupations introduced. We monitor total angular momentum, normalisation, and energy as functions of time.

Fig. C.2 plots the occupation of the m modes as a function of time in the outer ring. The coupling strength is 1.6, and the interaction strength is $\gamma = 4$. At this coupling strength the stability analysis above predicts that the ± 1 modes will grow in occupation. Fig. C.3 plots the same occupations for the first excited state at a tunnel coupling of 3.2, where the $m = \pm 2$ modes are expected to grow in occupation. These figures can be compared to Fig. 2 in Ref. [45]. In both cases, the modes predicted by the stability analysis are the first to show an increase in occupation. In both cases other modes become occupied at longer times, however these are much smaller in amplitude. Energy, angular momentum, and normalisation are conserved with the largest error being proportional to 10^{-4} (angular momentum in the $\kappa = 1.6$ case), all other errors are proportional to, or smaller than 10^{-8}. We take the error to be the value at the end of the propagation (30τ) less the value at the start of the propagation.

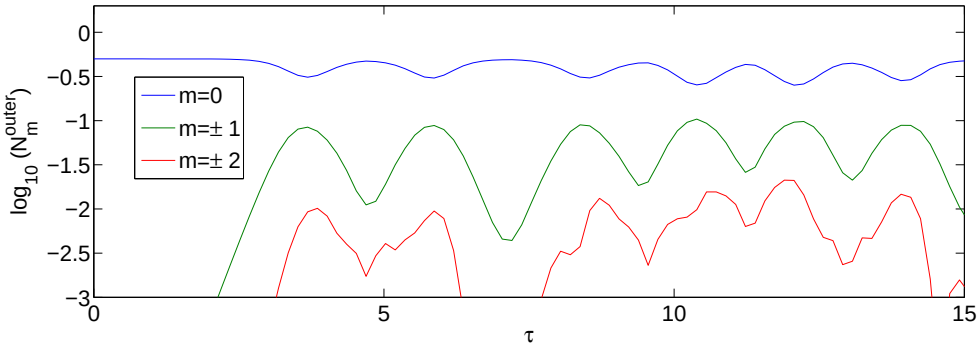

Figure C.2: Evolution of angular momentum mode occupations, $\kappa = 1.6$

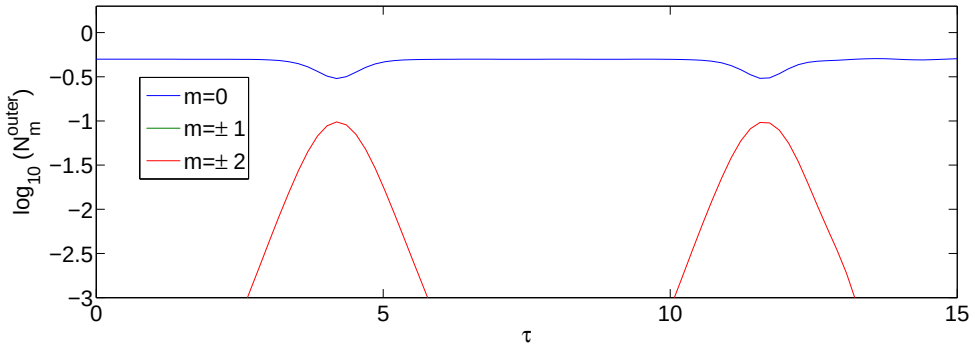

Figure C.3: Evolution of angular momentum mode occupations, $\kappa = 3.2$

C.2 Stability of co-planar double-ring BECs

We now extend the stability analysis to the co-planar double-ring system studied in this thesis, for the non-rotating case. To do this we follow the same method as for the same-radii system, except that in the system of equations given in equation (C.5) the kinetic energy terms will contain prefactors with the effective radii. For the co-planar system the equations analogous to (C.5) are

$$i\frac{\partial \alpha_m^{\mathrm{i/o}}}{\partial \tau} = \frac{{m_{\mathrm{i/o}}}^2}{\rho_{\mathrm{i/o}}^2}\alpha_m^{\mathrm{i/o}} - \kappa e^{i(\theta_{\mathrm{i/o}}-\theta_{\mathrm{o/i}})}\alpha_m^{\mathrm{o/i}} + \gamma\sum_k\sum_l \alpha_{m+k-l}^{\mathrm{i/o}}\alpha_k^{\mathrm{i/o}^*}\alpha_l^{\mathrm{i/o}} \tag{C.11}$$

Ground and first excited state solutions for the $m = 0$ mode in the co-planar ring case are the same as in equation C.6. The resulting eigenfrequency expressions are considerably more complex, but by plotting the frequencies we quickly see that similar dynamic instabilities are expected in the first excited state of the co-planar double-ring system. The regions of tunnel coupling where dynamic instabilities are expected vary slightly depending on the chosen values of the effective radii, but are very similar to those shown in Fig. C.1. The eigenfrequencies of the ground state remain real and positive for all coupling strengths.

Appendix D

Contents of CD

1. Bose-Einstein Condensates in Coupled Co-planar Double-Ring Traps.pdf
2. Non-rotating ground state - solving for radial density profiles. Includes Mathematica code for minimisation method used to calculate ground state wave functions. Total potential.nb contains the mathematical form of the double ring potential, and conversion of scaled quantities back to real units.
3. First excited state, Two-state model. Mathematica code for determining the first excited state wave function. Tests the validity of the two-state model.
4. Rotating ground state. Contains Mathematica code for minimisation method used to calculate wave functions carrying any quanta of angular momentum, and determination of the ground states as a function of frequency for the double-ring, and single ring confinements.
5. Ground state - MATLAB. Includes code for imaginary time propagation. Contains ground state wave functions, and analytic calculations of the ground states for zero interactions, and for variational model.
6. Dynamics of JVs - MATLAB. Includes code for propagation of a wave function through real time, and data shown in Section 5.1 and 5.2.
7. Analytic JVs - phase profiles and inertia.
8. Double ring instabilities. Contains Mathematica file used to calculate spectrum of excitation energies. Also contains MATLAB code for evolving a ground or first excited state in time.

Bibliography

[1] S. N. Bose, Z. Phys., **26**, 178 (1924), English translation in: B. Banerjee, Phys. News **5**, 2, 40, 42, (1974).

[2] A. Einstein, Sitzber. Kgl, Preuss. Akad. Wiss., **3** (1925).

[3] C. N. Cohen-Tannoudji, Rev. Mod. Phys. **70**, 707 (1998).

[4] K. B. Davis, M. -O. Mewes, M. R. Andrews, N. J. van Druten, D. S. Durfee, D. M. Kurn, and W. Ketterle, Phys. Rev. Lett. **75**, 3969 (1995).

[5] M.H. Anderson, J.R. Ensher, M.R. Matthews, C.E. Wieman, and E.A. Cornell, Science **269**, 198 (1995).

[6] C. A. Cornell, and C. E. Wieman, Rev. Mod. Phys. **74**, 875 (2002).

[7] M. R. Andrews, C. G. Townsend, H.-J. Miesner, D. S. Durfee, D. M. Kurn, and W. Ketterle, Science **275**, 637 (1997).

[8] P. B. Blakie, and M. J. Davis, Phys. Rev. A **72**, 063608 (2005).

[9] G. Modugno, M. Modugno, F. Riboli, G. Roati, and M. Inguscio, Phys. Rev. Lett. **89**, 190404 (2002).

[10] J. L. Roberts, N. R. Claussen, S. L. Cornish, E. A. Donley, E. A. Cornell, and C. E. Wieman, Phys. Rev. Lett. **86**, 4211, (2001).

[11] W. Ketterle, Rev. Mod. Phys. **74**, 1131, (2002).

[12] F. Pereira, D. Santos, and A. Landragin, Phys. World **20**, 32, (2007).

[13] K. Brugger, T. Calarco, D. Cassettari, R. Folman, H. Albrecht, B. Hessmo, P. Krüger, T. Maier, and J. Schmiedmayer, Jour. Mod. Optics **47**, 2789 (2000).

[14] L. Pitaevskii, and S. Stringari, *Bose-Einstein Condensation* (Oxford University Press, New York, 2003).

[15] E. P. Gross, Nuovo Cimento **20**, 454 (1961).

[16] L. P. Pitaevskii, Zh. Eksp. Teor. Fys. **40**, 646 (1961), English translation in Sov. Phys. JETP **13**, 451 (1961).

[17] A. L. Fetter, arXiv:0801.2925 (2008).

[18] R. W. Spekkens, and J. E. Sipe, Phys. Rev. A **59**, 3868 (1999).

[19] J. Tempere, J. T. Devreese, and E. R. I. Abraham, Phys. Rev. A **64**, 023603 (2001).

[20] K. Helmerson, M. F. Anderson, C. Ryu, P. Clade, V. Natarajan, A. Vaziri, and W. D. Phillips, Nucl. Phys. A **790**, 705c (2007).

[21] C. Cohen-Tannoudji, B. Diu, and F. Laloë, *Quantum Mechanics, Vol I* (Wiley and Herman, Paris, 1997).

[22] A. Smerzi, S. Fantoni, S. Giovanazzi, and S. R. Shenoy, Phys. Rev. Lett. **79**, 4950 (1997).

[23] S. Raghavan, A. Smerzi, F. Fantoni, and S. R. Shenoy, Phys. Rev. A **59**, 620 (1999).

[24] E. Sakellari, M. Leadbeater, N. J. Kylstra, and C. S. Adams, Phys. Rev. A **66**, 033612 (2002).

[25] B. D. Josephson, Rev. Mod. Phys. **46**, 251 (1974).

[26] A. Barone, and G. Paternò , *Physics and Applications of the Josephson Effect* (Wiley, New York, 1982).

[27] A. Messiah, *Quantum Mechanics* (Dover, New York, 1999).

[28] M. Albiez, R. Gati, J. Fölling, S. Hunsmann, M. Cristiani, and M. K. Oberthaler, Phys. Rev. Lett. **95**, 010402 (2005).

[29] E. M. Wright, J. Arlt, and K. Dholakia, Phys. Rev. A **63**, 013608 (2000).

[30] W. D. Phillips, in: J. Dalibard, J. M. Raimond, and J. Zinn-Justin, eds, *Fundamental Systems in Quantum Optics* (Elsevier, Amsterdam, 1992), pp. 1-164.

[31] C. Cohen-Tannoudji, in: J. Dalibard, J. M. Raimond, and J. Zinn-Justin, eds, *Fundamental Systems in Quantum Optics* (Elsevier, Amsterdam, 1992), pp. 166-210.

[32] A. Rakonjac, unpublished notes (2005-2006).

[33] T. Kuga, T. Yoshio, N. Shiokawa, and T. Hirano, Phys. Rev. Lett. **78**, 4713 (1997).

[34] M. Edwards, and K. Burnett, Phys. Rev. A **51**, 1382 (1995).

[35] W. Bao, and W. Tang, Jour. Comp. Phys **187**, 230 (2003).

[36] J. Brand, unpublished notes (2007).

[37] U. Zuelicke, unpublished notes (2007).

[38] A. V. Ustinov, Physica D **123**, 315 (1998).

[39] Z. Hermon, A. Stern, and E. Ben-Jacob, Phys. Rev. B **49**, 14 (1994).

[40] *Handbook of Mathematical functions*, Edited by M. Abramowitz, and I. A. Stegun, (Dover, New York, 1965).

[41] J. Brand, unpublished notes (2007).

[42] V. M. Kaurov, and A. B. Kuklov, Phys. Rev. A **73**, 013627 (2006).

[43] A. Shnirman, E. Ben-Jacob, and B. Malomed, Phys. Rev. B **56**, 14677 (1997).

[44] S.-H. Kim, C. Won, S. D. Oh, and W. Jhe, e-print arXiv:9904087

[45] I. Lesanovsky, and W. von Klitzing, Phys. Rev. Lett **98**, 050401 (2007).